Meso- and submesoscale variability within the Peruvian upwelling regime: Mechanisms of oxygen supply to the subsurface ocean.

Dissertation
zur Erlangung des Doktorgrades
der Mathematisch - Naturwissenschaftlichen
Fakultät
der Christian-Albrechts-Universität zu Kiel

vorgelegt von
Sören Thomsen
Kiel, Dezember 2015

Erster Gutachter: Prof. Dr. Torsten Kanzow

Zweiter Gutachter: Prof. Dr. Richard J. Greatbatch

Tag der mündlichen Prüfung: 05.02.2016

Zum Druck genehmigt: 05.02.2016

gez. _____

Prof. Dr. Wolfgang J. Duschl, Dekan

Für dich Klaus

Abstract

The role of meso- and submesoscale processes for the near-coastal circulation, physical and biogeochemical tracer distributions and oxygen minimum zone ventilation in the Peruvian upwelling regime is investigated in this thesis. A multi-platform four-dimensional observational experiment was carried out off Peru in early 2013 and is the basis for this thesis. Furthermore a high-resolution submesoscale permitting physical circulation model is used to study submesoscale frontal dynamics in more detail. The formation of a subsurface anticyclonic eddy and its impact on the near-coastal salinity, oxygen and nutrient distributions was captured by the observations. The eddy developed in the Peru-Chile Undercurrent downstream of a topographic bend, suggesting flow separation as the eddy formation mechanism. The eddy resulted in enhanced cross-shore exchange of physical and biogeochemical tracers due to along-isopycnal stirring and offshore transport of core waters. The core waters originated from the bottom boundary layer and were characterized by low potential vorticity and an enhanced nitrogen-deficit. The subduction of highly oxygenated surface water in a submesoscale cold filament is observed by glider-based measurements. The subduction ventilates the upper oxycline but does not reach into oxygen minimum zone core waters during the summer observations. Lagrangian floats are used to study the pathways of newly upwelled water in a regional submesoscale permitting model. The model analysis suggests a gradual warming of the newly upwelled waters due to surface heat fluxes. The associated density decrease prevents the floats to enter the density range of the oxygen minimum zone in summer. However, in winter a density increase is found due to surface cooling and thus it might be possible that submesoscale processes ventilate the oxygen minimum zone. In the model about 50 % of the newly upwelled floats leave the mixed layer within 5 days both in summer and winter emphazising a hitherto unrecognized importance of subduction for the ventilation of the Peruvian oxycline.

Zusammenfassung

Ziel dieser Doktorarbeit ist es zu einem tieferen Verständnis für die Rolle von meso- und submesoskaligen Prozessen für die Zirkulation, die physikalischen und biogeochemischen Tracerverteilungen sowie die Sauerstoffventilation in der küstennahen Sauerstoffminimumzone vor Peru beizutragen. Hierfür wurde eine auf verschiedenen Plattformen basierende vier-dimensionale Messkampagne im Frühjahr 2013 vor Peru durchgeführt. Zusätzlich wurde ein hochauflösendes physikalisches Ozeanzirkulationsmodel, welches Bereiche des submesoskaligen Regimes explizit auflöst, genutzt um submesoskalige Frontenprozesse im Detail zu untersuchen. Die Formation eines antizyklonalen Wirbels mit Kern unterhalb der Thermokline und dessen Einfluss auf die küstennahe Salz-, Sauerstoff- und Nährstoffverteilung konnte während der Messkampange beobachtet werden. Da sich der Wirbel direkt hinter einer abrupten topographischen Biegung bildet, wird Strömungsablösung als Wirbelformationsmechanismus vermutet. Auf Grund von mesoskaliger Vermischung entlang von Isopykanen und dem Transport von Wasser im Wirbelkern verursacht der Wirbel einen erhöhten Austausch von physikalischen und biogeochemischen Tracern zwischen dem offenen Ozean und der Küstenregion. Die Kernwassermassen entstammen der bodennahen turbulenten Grenzschicht und zeichnen sich durch niedrige potentielle Wirbelhaftigkeit sowie erhöhten Stickstoffmangel aus. Die Subduktion von mit Sauerstoff angereichertem Oberflächenwasser innerhalb eines submesoskaligen Kaltwasserfilaments wurde von Gleitermessungen aufgezeichnet. Die Subduktion ventiliert die obere Oxykline, reicht allerdings im Sommer nicht bis in den Kern der Sauerstoffminimumzone. Mit Hilfe von numerischen Lagrangschen Partikeln wird der Pfad von frisch aufgetriebenem Wasser in einem regionalen Ozeanmodel, welches submesoskalige Prozesse teilweise explizit auflöst, untersucht. Die Modeluntersuchungen lassen vermuten, dass eine kontinuierliche Erwärmung des aufgetriebenen Wasser erfolgt. Die damit verbundene Reduzierung der Dichte hindert die Partikel im Sommer in den Dichtebereich der Sauerstoffminimumzone zu gelangen. Im Winter hingegen wird teilweise eine Erhöhung der Dichte durch atmosphärische Abkühlung beobachtet, welche eine Ventilation der Sauerstoffminimumzone durch submesoskalige Prozesse ermöglichen könnte. Im Model verlassen ungefähr 50 % der frisch aufgetriebenen Floats die Deckschicht innerhalb von 5 Tagen. Dies deutet auf eine bis dahin unerkannte Wichtigkeit von Subduktionsprozessen für die Ventilation der peruanischen Oxykline hin.

Contents

1 Introduction

The ocean, as an important component of the Earth's climate system, stores and transports heat, freshwater and climate relevant gases such as CO_2 (*Siedler et al.*, 2001). In both the atmosphere and the ocean, turbulent motion drives a large portion of these transports and thus is crucial for the overall climate system (*Wunsch*, 2002; *Zhang et al.*, 2014). In the ocean turbulent processes exist on various length scales (*Olbers et al.*, 2012). They range from mesoscale eddies with diameters of hundreds of kilometres down to internal waves with wavelength of centimeters which break and stimulate diapycnal mixing on millimeter scales.

In the ocean, turbulent motion has traditionally been categorized into three dynamical regimes: the two-dimensional geostrophic mesoscale, the internal wave field and the three-dimensional microscale (*Ferrari and Wunsch*, 2009). In recent years, this traditional dynamical view of three exclusive types of motions was expanded by including a fourth regime of motion: submesoscale frontal processes. The latter play an important role in the near surface ocean dynamics, where the geostrophic balance, which holds if the horizontal pressure gradient force is balanced by the Coriolis force, breaks down and ageostrophic effects become important (*Thomas et al.*, 2008; *Ferrari*, 2011; *Levy et al.*, 2012). Submesoscale frontal processes are most pronounced in the weakly stratified mixed layer but also affect the dynamics within the thermocline (*Badin et al.*, 2011; *Ramachandran et al.*, 2014). These processes can drive large vertical velocities and thus are crucial for understanding tracer fluxes between the atmosphere and the ocean interior (*Capet et al.*, 2008a). Furthermore submesoscale instabilities seem to provide key mechanisms to connect the three traditional regimes by extracting energy from the balanced geostrophic motion and supplying it to three-dimensional turbulence, where it finally dissipates (*Taylor and Ferrari*, 2009; *Molemaker et al.*, 2010; *Brueggemann and Eden*, 2014).

The first idealized basin scale two-layer ocean model with mesoscale eddies was developed by *Holland and Lin* (1975a,b). Since more than 20 years mesoscale eddies are found in more realistic basin scale three-dimensional ocean models (e.g. *Treguier et al.*, 2005) and nowadays there are even high-resolution global climate models which allow the explicit simulation of mesoscale eddies in the ocean (*Delworth et al.*, 2012). However, submesoscale processes are far from being resolved in large-scale long-term simulations (*Fox-Kemper et al.*, 2011). As submesoscale frontal processes are known to be important for air-sea gas exchange, and thus for the fluxes of climate relevant gases, such as CO_2 (*D'Asaro et al.*, 2011; *Ferrari*, 2011), parameterizations of the effects of subgridscale processes are needed (*Fox-Kemper and*

Ferrari, 2008; *Brueggemann and Eden*, 2014). Still there are large uncertainties concerning the understanding and the ability to parameterize the effects of submesoscale variability (*Mahadevan et al.*, 2010; *Brueggemann and Eden*, 2014). Consequently, the uncertainties influence the predictability of quantities that are highly affected by the submesoscales, as e.g. mixed layer depth or the air-sea gas exchange of heat and trace gases (*Oschlies*, 2002; *D'Asaro et al.*, 2011; *Ferrari*, 2011). In order to constrain new parametrizations and improve or evaluate the existing ones, a deeper process understanding is needed. However, the recent increase in computational power and the large cost reduction of computing time made it possible to increase the resolution of regional ocean general circulation models down to some hundred meters. Consequently, more and more high resolution regional and idealized model studies exist that have sufficient resolution to permit submesoscale frontal processes (*Thomas et al.*, 2008; *Gula et al.*, 2014; *Molemaker et al.*, 2015). The simulations are restricted to certain regions and are only integrated over short time periods of several years. Still they can be used to improve our recent understanding of submesoscale dynamics. However, due to their short integration time the simulations do not capture long term climate signals and thus cannot be used for climate predictions.

Submesoscale processes are characterized by short time scales of O(day) and length scales of O(100 m - 10 km) and thus are hard to capture synoptically by traditional shipboard measurement programs. Hydrographic measurements are able to achieve a vertical resolution of several centimeters but seldom are made closer than ten km apart in the horizontal during large scale surveys. However, if strong lateral density gradients exist and stratification is low, the occurrence of submesoscale processes can be expected. First measurements of fronts in the surface mixed layer reach back to the early campaigns of *Uda* (1938),*Cromwell and Reid* (1956) and *Knauss* (1957). Despite these early observations the scientific interest in surface fronts is a relatively new phenomenon (*Munk et al.*, 2000; *Thomas et al.*, 2008). This might be related to the fact that the observations of submesoscale near-surface processes increased significantly in recent years due to the developement of towed systems, which enable to measure hydrographic properties with high horizontal resolution (e.g. *Pollard and Regier*, 1992; *Rudnick and Luyten*, 1996; *Lee et al.*, 2006; *Hosegood et al.*, 2006; *Thomas et al.*, 2013). Nevertheless, it remains extremely challenging to explore the temporal variability of these small scale processes by direct measurements.

However, new measurement platforms such as gliders are able to capture these processes. Although gliders are relatively slow compared to towed shipboard measurements, they are highly suited to study submesoscale dynamics as they can be used in fleets to achieve three-dimensional fields of variables.

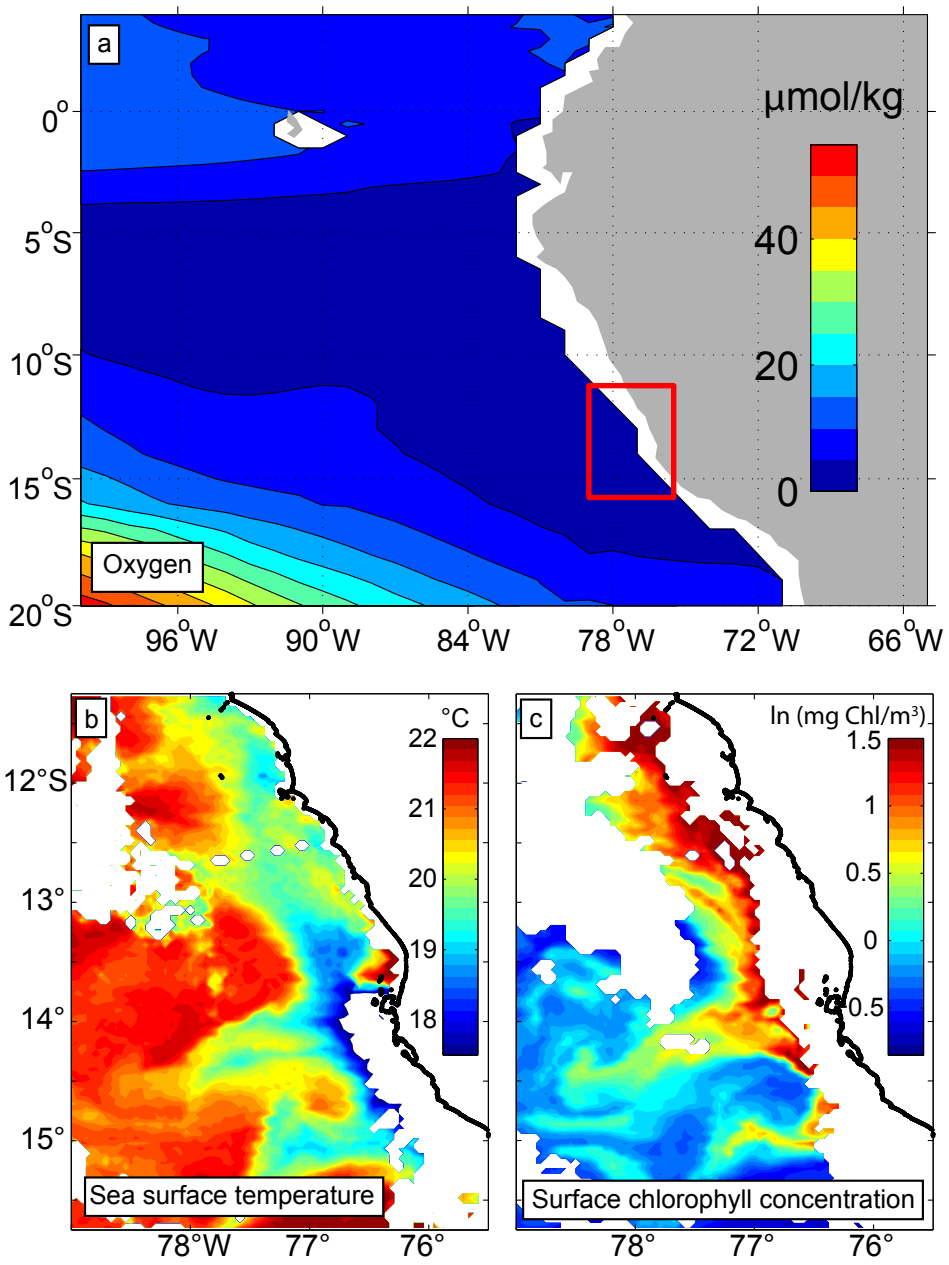

Figure 1: Oxygen concentration (a) in μmol/kg in the eastern tropical Pacific at $\sigma_\theta = 26.8\ kg/m^3$ as obtained from the MIMOC climatology (*Schmidtko et al.*, 2013). The red square indicates the region shown in (b) and (c), which represent the study area of this thesis. Sea surface temperature in °C (b) and surface chlorophyll concentrations (c) in logarithmic form (of unit mg/m^3) from MODIS Aqua satellite measurements on January 25 2013 off Peru.

One important challenge due to the short time scale of these processes is to separate temporal and spatial variability, which is difficult with one single moving sensor platform such as a ship alone. However, with a swarm of gliders covering a small area it might become possible to separate spatial from temporal changes.

The Peruvian upwelling regime, as one of the four major eastern boundary upwelling systems, shows pronounced meso- and submesoscale variability (Fig. 1b,c; *Capet et al.* 2008b; *McWilliams et al.* 2009). Mesoscale eddies and submesoscale filemants have large effects on the horizontal and vertical transport of momentum, heat and tracers (*Klein and Lapeyre*, 2009). In upwelling systems, this variability is thought to induce a net reduction of biological productivity by exporting nutrients from the productive near-coastal region into the open ocean (*Rossi et al.*, 2008, 2009; *Lathuilière et al.*, 2010; *Gruber et al.*, 2011; *Nagai et al.*, 2015).

The highly productive Peruvian upwelling regime encompasses the most intense and shallowest oxygen minimum zone (OMZ) in the ocean (Fig. 1a; *Karstensen et al.* 2008; *Fuenzalida et al.* 2009; *Paulmier and Ruiz-Pino* 2009). OMZs are characterized by a sluggish mean circulation and thus mesoscale eddies are important for ventilating OMZs by means of along-isopycnal stirring (*Wyrtki*, 1962; *Luyten et al.*, 1983a; *Stramma et al.*, 2010; *Hahn et al.*, 2014; *Brandt et al.*, 2015). However, so far little is known about the role of mesoscale eddies for the circulation and ventilation of the near-coastal OMZ off Peru. Submesoscale frontal processes can drive large vertical velocities and enhance vertical tracer fluxes in the upper ocean (*Capet et al.*, 2008a). Due to the vicinity of the well-oxygenated mixed layer and the OMZ waters below, vertical advective motion driven by submesoscale frontal dynamics might be a key process for the vertical supply of oxygen into the OMZ off Peru. However, submesoscale processes and in particular their potential role for the oxygen ventilation have not been addresses so far.

The focus of this thesis lies on turbulent motion found in the upper ocean in the Peruvian upwelling regimes. In particular the role of meso- and submesoscale processes for the near-coastal circulation, tracer distribution and ventilation of the OMZ is investigated. The following three main scientific questions will be addressed:

1. How is the near-coastal circulation influenced by meso- and submesoscale motion?

2. How do meso- and submesoscale processes impact on the near-coastal tracer distribution?

3. What is the role of meso- and submesoscale processes for the near-coastal oxygen ventilation?

To answer these questions a multi-platform four-dimensional observational experiment was carried out off Peru in early 2013 which is the basis for this thesis. Furthermore a high-resolution submesoscale permitting physical model is used to study submesoscale frontal dynamics in more detail.

This thesis is structured as follows: First the theoretical background is given in section 2. This includes the definition of key terms used in this thesis (section 2.1). Then follows the introduction of four different oceanic regimes and the underlying physics, including mesoscale dynamics (section 2.2), submesoscale frontal processes (section 2.3 and 2.4) as well as the internal wave and the three-dimensional turbulent regime (section 2.5). The role of submesoscale frontal processes for the energy cycle are described in section 2.6. In section 2.7 the mathematical framework for turbulent tracer fluxes is introduced. The role of meso- and submesoscale flows for the biogeochemistry is described in section 2.8. The observational dataset and the model simulation used in this thesis are briefly introduced in section 3. The seasonal cycle of the Peruvian upwelling regime is described in section 4. Section 5 consists of a manuscript which is under review for Journal of Geophysical Research - Oceans. The manuscript focuses on the formation of a subsurface anticyclonic mesoscale eddy in the Peru-Chile Undercurrent and its impact on the near-coastal salinity, oxygen and nutrient distributions. In section 6 the question whether submesoscale processes ventilate the oxygen minimum zone off Peru is investigated based on high-resolution glider observations and regional model simulation output in a manuscript submitted to Geophysical Research Letters. A summary and a synthesis are given in section 7. The thesis ends with a conclusion and an outlook on future work.

2 Theoretical background

2.1 Definition of key terms

In the ocean, turbulent motion over a wide range of scales is found (*Olbers et al.*, 2012). As these scales often interact it is, in general, not possible to clearly separate the associated motions. Therefore, it is often helpful to define different dynamical regimes in which certain of these processes dominate. However, it is necessary to keep in mind that these dynamical regimes usually interact and the separation should rather be seen as a guide than an absolute physical constraint. In the following sections, four dynamical regimes are introduced: meso- and submesoscale variability, internal waves and the isotropic microscale regime.

2.1.1 Richardson and Rossby number

A common way, to distinguish between different dynamical regimes is to define non-dimensional numbers that express ratios between two different processes or quantities. The magnitude of such a non-dimensional number thus tells which of the quantities or processes dominates over the other. The Richardson number (Ri) gives the ratio of vertical stability to vertical shear and is usually defined by $\mathrm{Ri} = N^2/S^2$, where $N^2 = -g/\rho_0 \cdot \partial\rho/\partial z$ is the Brunt-Väisälä frequency, with g being the acceleration due to gravity, ρ the locally defined neutral density, ρ_0 a reference density and $S = ((du/dz)^2 + (dv/dz)^2)^{1/2}$ is the vertical shear, with u and v being the zonal and meridional velocity component, respectively. The Rossby number (Ro) gives the ratio between the inertial and Coriolis forces and is defined by $\mathrm{Ro} = U/(fL)$, where U and L are typical velocity and length scales, respectively and f is the local Coriolis parameter. The Rossby number can also be approximated by $\mathrm{Ro} = \xi/f$ with ξ the vertical component of the relative vorticity $\xi = \partial v/\partial x - \partial u/\partial y$, since $\xi \sim O(U/L)$.

2.1.2 Rossby and mixed layer radius

The first baroclinic Rossby radius of deformation is defined as $R_d = c/f$, where c is the baroclinic gravity-wave phase speed (e.g. *Gill*, 1982; *Chelton et al.*, 1998). In case of uniform stratification the first baroclinic Rossby radius of deformation can be approximated by $R_d = NH/f$, where N is the Brunt-Väisälä frequency and H the water depth. The Rossby radius defines the length scale above which baroclinic motion is more influenced by rotational than gravitational effects. In such a baroclinically unstable flow the fastest growing waves have a lateral size close to the first baroclinic

Rossby radius of deformation (*Eady*, 1949). In recent years the so-called mixed layer radius R_{ML} was introduced as a length scale for submesocale processes (*Thomas et al.*, 2008). The mixed layer radius is defined as $R_{ML} = Nh/f$, where N is the average stratification in the mixed layer and h the mixed layer depth. It defines the typical length scale of geostrophic motion restricted to the mixed layer (*Thomas et al.*, 2008).

2.1.3 Oceanic fronts

An ocean front is here loosely defined as a location with a strong horizontal buoyancy gradient without any particular threshold being set (*Hoskins*, 1982). In the ocean, fronts of various sizes and depth scales exist but it makes sense to distinguish between two types of fronts. Shallow fronts are mainly found in the surface mixed layer whereas deep fronts penetrate into the interior ocean. In general, mixed layer fronts and the shallow parts of deep fronts exhibit much stronger lateral buoyancy gradients than the fronts in the ocean interior. This is because the free surface and the strong stratification in the thermocline suppress vertical motion and thus favour frontogenesis, the strengthening of a horizontal density gradient by a confluent flow (*Hoskins*, 1982). Frontogenesis in the deeper ocean is balanced by overturning eddy fluxes which counteract the frontogenesis (*Levy et al.*, 2012). Thus submesoscale frontal processes are mainly found in the mixed layer. In section 2.4 the term frontogenesis and its role for cold filament intensification is described in more detail.

2.1.4 Geostrophic balance

An important concept of ocean dynamics is the so called geostrophic balance. For a flow with small Rossby numbers ($Ro << 1$) the horizontal component of the momentum equation reduces to a balance between the pressure gradient force and the Coriolis force. The resulting geostrophic flow can be directly diagnosed from the oceanic pressure field as it flows along lines of constant pressure. The difference between an observed flow and a geostrophic flow is called ageostrophic flow. Ageostrophic flow occurs for example at oceanic fronts, where the geostrophic balance is being disturbed by larger scale confluent flow. A secondary ageostrophic circulation develops to restore the geostrophic balance (section 2.4). In this thesis geostrophic or ageostrophic flows are often called 'balanced' or 'unbalanced' flows, respectively.

2.1.5 Potential vorticity and symmetric instability

Ertels potential vorticity (PV) is conserved in the absence of tracer and/or momentum mixing and is thus a fundamental property in fluid dynamics as well as an ideal tracer with which to identify and track water masses. PV can be defined as follows:

$q = \boldsymbol{\omega_a} \cdot \nabla b$ where $\boldsymbol{\omega_a} = \boldsymbol{fk} + \nabla \times \boldsymbol{u}$ is the absolute vorticity, where $\mathbf{k}$ is the vertical unit vector and $\mathbf{u}$ the velocity vector. The buoyancy is given by $b = -g\rho/\rho_0$, where g is the graviational acceleration, ρ the density and ρ_0 a reference density. *Thomas et al.* (2013) give a detailed overview of the different instability types and conditions related to potential vorticity. A short summary is given here following *Thomas et al.* (2013).

The PV can be decomposed into a vertical component q_{vert} and a baroclinic component q_{bc}:

$$q = q_{vert} + q_{bc}$$

with

$$q_{vert} = \xi_{abs} N^2 \quad \text{and} \quad q_{bc} = (\frac{\partial u}{\partial z} - \frac{\partial w}{\partial x})\frac{\partial b}{\partial y} + (\frac{\partial w}{\partial y} - \frac{\partial v}{\partial z})\frac{\partial b}{\partial x}$$

where the vertical component of the absolute vorticity is defined as $\xi_{abs} = f - \partial u/\partial y + \partial v/\partial x$. Now, assuming geostrophic and hydrostatic balance ($w = 0$) the last term of the equation above can be reduced to:

$$q_{bc}^g = -f \left| \frac{\partial \boldsymbol{u_g}}{\partial z} \right|^2 = -\frac{1}{f} |\nabla_h b|^2$$

When the PV of a geostrophically balanced flow takes the opposite sign of the Coriolis parameter ($qf < 0$) the flow is unstable to various instability types (*Hoskins*, 1974). If the vertical stratification ($N^2 = \partial b/\partial z < 0$) is responsible for the negative qf, ordinary upright convection, also called gravitational instability, occurs. However, even a statically stable flow ($N^2 > 0$) can have negative PV. The vertical component of the absolute vorticity ξ_{abs} can become negative leading to negative PV. This instability is termed inertial instability and might occur more preferentially close to the equator where f becomes zero and thus becomes neglectable for the absolute vorticity. If the baroclinicity of the flow is larger than the vertical vorticity ($|fq_{bc}^g| > fq_{vert}$), with $fq_{vert} > 0$, and thus is responsible for lowering the PV, the instability is called symmetric instability. In section 2.6 the processes occuring along a symmetrically unstable mixed layer front and their role for the kinetic energy cascade are discussed in detail.

2.2 Mesoscale dynamics

At the mesoscale, which here is referred to as horizontal scales larger than the first baroclinic Rossby radius of deformation of O(10–100 km), the horizontal flow is close to geostrophic balance. The geostrophic scaling is valid at small Rossby numbers (Ro << 1) and large Richardson numbers (Ri >> 1) (*Thomas et al.*, 2008). Most of the ocean's kinetic energy at subinertial frequencies is contained in the geostrophic mesoscale eddy field (*Ferrari and Wunsch*, 2009). Figure 2 shows the surface eddy kinetic energy inferred from satellite sea level anomaly measurements. Enhanced eddy kinetic energy is found within the Southern Ocean along the Antarctic Circumpolar Current, in the western boundary current regions of the subtropical gyres and a weaker maximum shows up in eastern boundary upwelling systems e.g off California and Peru (Fig. 2). It is important to note that also subsurface eddies can be found in the ocean (e.g. *McWilliams*, 1985; *D'Asaro*, 1988; *Molemaker et al.*, 2015). The sea level anomaly signal for such subsurface eddies is often very weak or not present. This makes it difficult to detect these eddies by satellite measurements. However, in the Peruvian upwelling regions these subsurface eddies make an important portion of the mesoscale eddy field (*Colas et al.*, 2012) and can often only be seen by direct *in-situ* measurements as shown in section 5.

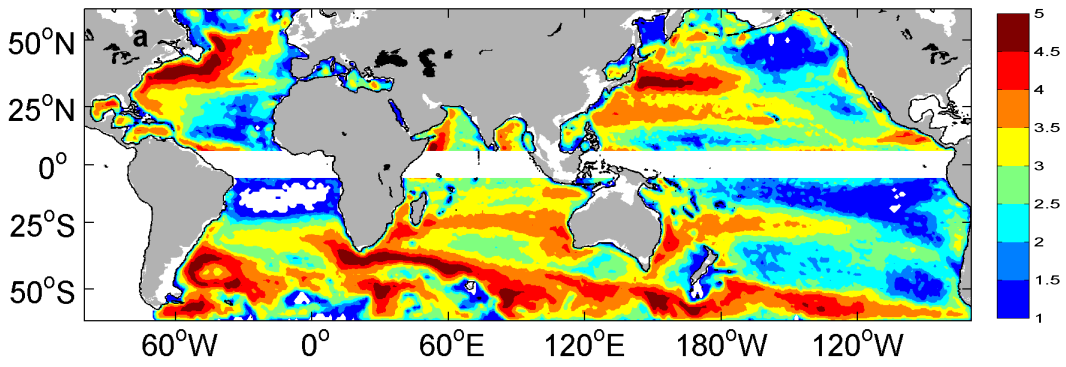

Figure 2: Global horizontal distribution of mean eddy kinetic energy in logarithmic form (of unit J/m2) based on altimeter data available by the AVISO Altimetry Operations Center. Figure is taken from (*Xu et al.*, 2014)

Mesoscale eddies are generated via barotropic and/or baroclinic instability, where the former is a horizontal and the latter a vertical shear instability (*Olbers et al.*, 2012). In the ocean interior baroclinic instability seems to be the dominant eddy kinetic energy source (e.g. *von Storch et al.*, 2012). The Eady growth rate, given by $\omega_{Eady} = 0.3f/\sqrt{Ri}$, is a good proxy for measuring

baroclinic instability (*Eady*, 1949; *Olbers et al.*, 2012). Regions of enhanced Eady growth rates based on hydrographic data are indeed well correlated with high eddy kinetic energy (*Chelton et al.*, 2007; *Vollmer and Eden*, 2013; *Thomsen et al.*, 2014).

In boundary current regions, strong lateral shear exists and barotropic instabilities and interactions with topography are also important for generating mesoscale eddies (*Gula et al.*, 2015). It is important to note that even if unforced mesoscale instabilities such as baroclinic and barotropic instability are mainly used to describe the generation of mesoscale eddies, several recent studies point out the importance of submesoscale instabilities and upscale energy transfer for the generation of mesoscale features (*Molemaker et al.*, 2015). This will be discussed in more detail later as it is of relevance for the eddy formation described in section 5. Mesoscale eddies further play an important role for the along-isopycnal tracer transport due to mesoscale stirring (section 2.7) and modulate biogeochemical processes (section 2.8).

2.3 Submesoscale frontal processes

Submesoscale frontal processes operate on lateral scales smaller than mesoscale eddies but are still influenced by rotation and stratification as they are characterized by Ro and Ri of O(1) (*Thomas et al.*, 2008; *Levy et al.*, 2012). Figure 3a,b taken from (*Thomas et al.*, 2008) shows the local Ro and Ri within a simulated flow field. Note the increase and decrease of the Ro and Ri, respectively in specific areas (e.g. at x = 14 - 22 km and y = 35 km). In submesoscale flows the relative vorticity ξ becomes comparable to the planetary vorticity f since $Ro = U/(fL) = \xi/f = O(1)$. Different to mesoscale flows, submesoscale flows are only partly geostrophically balanced as advection of momentum plays a significant role.

The horizontal velocity or density gradients associated with submesoscale flows are found at a typical length scale L, which we want to derive here following (*Thomas et al.*, 2008). This length scale is given by $L = U/f$ as $\xi \sim U/L$ and $Ro = U/(fL) = O(1)$. Assuming thermal wind balance $U \sim b_y h/f$; the horizontal velocity scale U can be related to the lateral buoyancy gradient b_y and the mixed layer depth h, the vertical scale at which the velocity and lateral buoyancy gradients are dominant. It follows that $L = b_y h/f^2$. Using now the relationship between the lateral and vertical buoyancy gradients at an adjusted front $N^2 = b_y^2/f^2$ (*Tandon and Garrett*, 1994) the typical length scale can also be expressed in terms of stratification $L = Nh/f$, where N is the depth averaged Brunt-Väisäla frequency and h a depth scale, which is often the mixed layer depth. Note the similarity to the first baroclinic Rossby radius of deformation describing mesoscale

motion, where h represents the full water depth. This results in a length scale $L = 2.15\,km$ using typical values for the mixed layer depth of h = 15 m, $N = 5 \times 10^{-3} s^{-1}$ and the Coriolis parameter $f = 3.5 \times 10^{-5}$ found during the summer season in the Peruvian upwelling regime (*Koehn*, 2014).

The inverse of the growth rate ω_{growth} of baroclinic mixed layer instabilities given by $1/\omega_{growth} = \sqrt{Ri}/f$ is often used as a typical time scale of submesoscale variability. This results in a typical time scale of $O(1/f)$ since $Ri = O(1)$ (*Thomas et al.*, 2008). Both, the time and the length scale of submesoscale motion are influenced by the Coriolis parameter. This implies that submesoscale processes have longer timescales and larger lateral scales closer to the equator. Thus, a definition of submesoscale processes based on fixed length scales can be misleading because submesoscale flows are defined by their dynamics and the associated time and length scale vary with latitude and mixed layer properties.

Thomas et al. (2008) describe three different mechanisms that are responsible to generate submesoscale motions:

1) Unforced instabilities are one mechanism to generate submesoscale variability. If strong winds pass an oceanic frontal region, the enhanced wind-stress results in enhanced vertical mixing within the upper ocean and a deepening of the mixed layer. During the wind event the stratification in the upper ocean is reduced, but lateral density gradients can still be present. Weak stratification, strong lateral density fronts and thus strong vertical shear are favorable conditions for submesoscale baroclinic instabilities as the Ri becomes small. Various studies have treated the unforced baroclinic instability problem at low Ri (*Stone*, 1966, 1970, 1972; *Haine and Marshall*, 1998; *Boccaletti et al.*, 2007). More recent studies also highlight the importance of barotropic instabilities at submesoscale fronts which are driven by strongly laterally sheared flow (e.g. *Gula et al.*, 2014).

2) Forced instabilities can grow under persistent atmospheric surface forcing. When wind blows in the direction of a frontal jet (i.e down-front), the associated ageostrophic Ekman transport within the mixed layer results in the advection of denser water over lighter water, which leads to convective driven mixing. The associated redistribution of buoyancy can drive a geostrophy-restoring ageostrophic secondary circulation which further strengthens the front (*Thomas and Lee*, 2005a). Strong near surface loss of buoyancy as a result of air-sea heat flux also favors submesoscale variability as it decreases the Ri (*Haine and Marshall*, 1998). The role of forced instabilities along submesoscale mixed layer fronts for the dissipation of kinetic energy is further discussed in section 2.6.

3) Frontogenesis, the intensification of a density front (*Hoskins* (1982), see more details in next subsection 2.4), is another mechanism to gener-

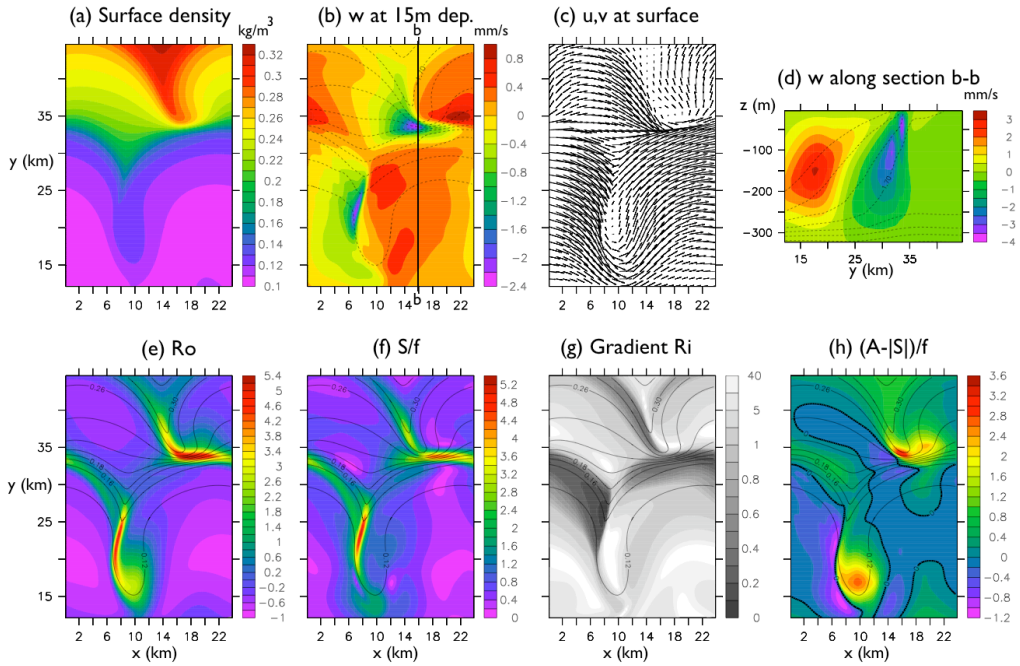

Figure 3: Numerical simulation of a front undergoing frontogenesis. Two specific areas are of interest here ($x_1 = 14 - 22\ km$, $y_1 = 35\ km$ and $x_2 = 8\ km$, $y_2 = 17.5 - 25\ km$), where cold filamentary intensification occurs. (a) Surface density, (b) vertical velocity, (c) surface u,v velocities, (d) vertical section of vertical velocity, (e) Rossby number, (f) Lateral strain rate $S_{strain} = ((\frac{\partial u}{\partial x} - \frac{\partial v}{\partial y})^2 + (\frac{\partial v}{\partial x} + \frac{\partial u}{\partial y})^2)^{1/2}$ divided by Coriolis parameter f, (g) gradient Ri and (h) stability criteria for unbalanced instability mode: $(A - \mid S_{strain} \mid)/f$. The criteria is met if the difference between the absolute vorticity ($A = f + \frac{\partial v}{\partial x} - \frac{\partial u}{\partial y}$) and the magnitude of the strain rate changes sign within the domain. For more details see (*Molemaker et al.*, 2005; *Thomas et al.*, 2008). Figure is taken from (*Thomas et al.*, 2008)

ate submesoscale variability. When a geostrophically balanced mixed layer front becomes unstable and starts to meander, regions with horizontal convergence and divergence are formed leading to a large lateral strain rate $S_{strain} = ((\partial u/\partial x - \partial v/\partial y)^2 + (\partial v/\partial x + \partial u/\partial y)^2)^{1/2}$ and Ri and Ro of O(1). An ageostrophic secondary circulation develops which is associated with enhanced vertical velocities (Fig. 3b,d).

In the real ocean these different types of generation processes exist often simultaneously making it difficult to distinguish between them. In summary, submesoscale processes can be expected to play an important role if strong lateral density gradients resulting in strong vertical shear are accompanied

by weak stratification and strong atmospheric buoyancy loss.

2.4 Frontogenesis and cold filamentary intensification

Submesoscale variability covers a relatively broad range of scales including symmetric instabilities at some hundred meter scales to features such as filaments which have a typical length scale of several tens of kilometers but are only a few kilometres broad. Filaments play a key role in upwelling regimes as they transport productive coastal water offshore and downwards (*Rossi et al.*, 2008, 2009; *Nagai et al.*, 2015). Off the coast of Peru, cold filaments are uniquitous features seen in sea surface temperature fields and thus their dynamics will be described shortly.

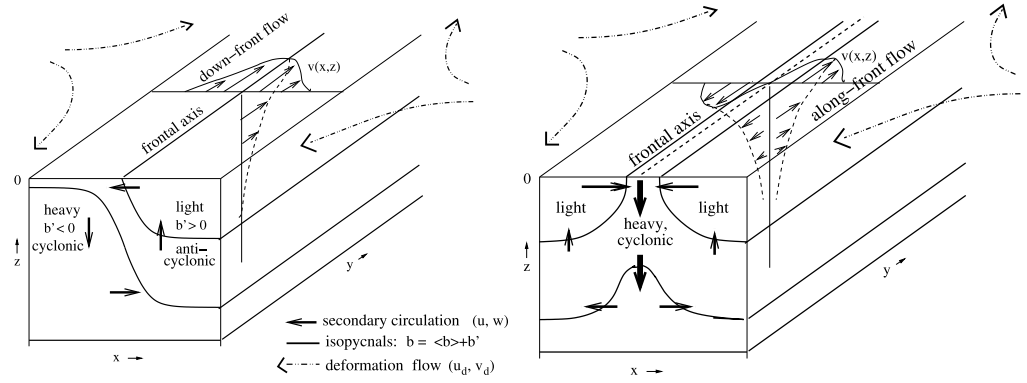

Figure 4: Sketches of surface frontogenesis (left) and cold filamentary intensification (right). On the right, a two-dimensional dense surface filament is undergoing frontogenesis in an external horizontal deformation flow (dotted–dash arrows) with uniform horizontal strain rate. Buoyancy contours (heavy solid lines) bulge up in the center, as labeled by "light" and "heavy". The approximately geostrophic longitudinal flow y (thin arrows) consists of a double jet. The ageostrophic secondary circulation (u, w) in the transverse plane (thick arrows) has central downwelling and peripheral upwelling, surface horizontal convergence, and subsurface horizontal divergence. Vortex stretching generates cyclonic vertical vorticity in the center and weaker anticyclonic vorticity on the edges. Figure is taken from (*McWilliams et al.*, 2009, 2015) with modified text.

Filaments can be described as an elongated double frontal system which can be separated into warm and cold filaments. To better understand the dynamics involved in the development of cold filaments, it is helpful to re-

capitulate the mechanisms that are responsible for the strengthening of a density front by a confluent large scale flows, called frontogenesis.

Frontogenesis has been studied in the atmospheric context for decades (*Hoskins*, 1982) but also occurs in the upper ocean (*Lapeyre et al.*, 2006; *Capet et al.*, 2008c). A sketch of this surface frontogenesis is shown in Figure 4a. Frontogenesis is caused by an external horizontal flow that deforms the flow field and yields strong horizontal density gradients. This deformation is responsible that the flow along the front has to accelerate. This acceleration drives an ageostrophic secondary circulation develops that restores the geostrophic balance of the front. Downwelling on the dense and upwelling on the light side of the front are typical characteristics of this secondary circulation (Fig. 4a). In the case of cold filamentary intensification (Fig. 4b), two fronts are aligned next to each other such that the center of this double front system is cold. Associated with these two fronts are two jets along each of the front resulting in large horizontal shear. Each of the two fronts contributes to the downwelling in the center of the front. This central downwelling is accompanied with a broader peripheral upwelling due to surface horizontal convergence and subsurface horizontal divergence. One open question is: Which factors ultimately limit the growth of frontogenesis when the straining deformation persists? This can be achieved by balanced instabilities as suggested by (*McWilliams and Molemaker*, 2011). Another more recent suggestion is that turbulence in the mixed layer and the associated momentum fluxes have to be taken into account when studying the arresting of frontogensis (*Gula et al.*, 2014; *McWilliams et al.*, 2015).

2.5 Internal waves and three-dimensional microscale turbulence

Surface waves found at the interface between the atmosphere and the ocean are a well known phenomenon for everyone looking at the ocean. However, also below the sea surface so-called internal waves are present, which lead to up- and downward motions in the water column. Internal waves propagate through the ocean interior and transport energy in the horizontal and vertical plane (*Mueller and Briscoe*, 2000).

Internal waves can be classified by their restoring forces, namely gravity or the Coriolis force. Gravity waves have a frequency close to the buoyancy frequency N and can only exist if a vertical density gradient is present. If the Coriolis force is the main restoring force, internal waves are called near-inertial waves with a frequency near f. However, more common are so-called internal inertial-gravity waves, which are influenced both by gravity and the Coriolis force. The period of free internal gravity waves is limited

by the buoyancy period $2\pi/N$, which has a typical range of 15 min in the upper ocean to several hours at greater depth, and by the inertial period $2\pi/f \geq 12$ h (*Olbers et al.*, 2012).

Internal waves can have various wavelengths ranging from several thousand kilometers down to centimeters. Fluctuating wind stress, tides and flow-topography interactions can generate internal waves (*Wunsch and Ferrari*, 2004). These propagate through the ocean where they interact with each other e.g. by resonant interaction (*Mueller and Briscoe*, 2000). Finally, small-scale internal waves can break, which results in turbulence and diapycnal mixing (*Munk*, 1966). Given that the internal waves provide an important energy source for the internal diapycnal mixing, they play an important role in the energy budget of the ocean circulation (*Wunsch and Ferrari*, 2004).

An important internal wave breaking mechanism is the so-called Kelvin-Helmholtz instability. It refers to the growth of small perturbations generated by the vertical shear of the horizontal velocity, which are not damped by the stratification. Mathematically the condition for Kelvin-Helmholtz instability to occur in a vertically sheared flow would be that Richardson numbers is below 1/4. This instability causes small-scale density overturns during the wave breaking which results in three-dimensional turbulence and diapycnal mixing (e.g. *Smyth et al.*, 2001). This diapycnal mixing is important for tracer fluxes across isopycnals. Diapycnal mixing is crucial for the global ocean circulation as it results in a downward heat transport and allows the cold and dense water found in the deep ocean to upwell (*Wunsch and Ferrari*, 2004).

2.6 Submesoscale routes to dissipation

The ocean gains kinetic energy at large scales due to atmospheric and tidal forcing (*Wunsch and Ferrari*, 2004). Finally, this kinetic energy dissipates at molecular scales and is transferred into heat and potential energy (*Wunsch and Ferrari*, 2004). The processes that accomplish the transfer of energy are not well understood. One major question in understanding global ocean dynamics is: How is the kinetic energy gained by the large scale forcing transported towards the smaller scales where it can be dissipated?

The exchange of kinetic energy between different length scales is called an energy cascade. Mesoscale motion transfers energy to larger scales, a process known as an 'inverse cascade' (*Charney*, 1971). Geostrophic turbulence therefore does not deliver an efficient pathway towards smaller scales (*Molemaker et al.*, 2010). However, breaking internal waves can transfer energy to small spatial scales into a regime of three-dimensional turbulence (*Garrett and Munk*, 1979). This regime of microscale turbulence is known to transfer

energy to even smaller scales called a 'forward cascade' (*Kolmogorov*, 1941), where it is finally dissipated by molecular processes. Due to the inverse energy cascade the mesoscale field plays an opposing role in energy transfer compared the internal waves and three-dimensional turbulent regime. However, contrary to mesoscale motion, submesoscale frontal processes seem to be able to break the geostrophic balance resulting in a 'forward cascade'. Recent studies show that submesoscale motion might deliver a pathway to extract energy from the geostrophic balanced state into the microscale turbulent regime (*Molemaker et al.*, 2010; *Brueggemann and Eden*, 2015).

Molemaker et al. (2010) carried out two high-resolution numerical simulation to investigate the energy transfer between different scales. At first they studied an idealized Boussinesq flow, a flow system which allows ageostrophic motion, and found that a 'forward energy cascade' directed towards small scale dissipation was established due to submesoscale frontal instabilities. As a second step the authors carried out a simulation with the same configuration but with a quasi-geostrophic model, which does not allow the advection by ageostrophic motion. This flow system was not able to establish a 'forward energy cascade', which points to the importance of the unbalanced flow at frontal regions for this route to dissipation.

Submesoscale frontal instabilities occur along submesoscale fronts and are described in the following. Figure 5 illustrates the ongoing processes at a wind-forced symmetrically unstable front. At strong lateral density fronts, symmetric instability can occur due to the strong vertical shear of the geostrophic flow. When submesoscale fronts experience strong atmospheric wind forcing along the geostrophic frontal jet, the ageostrophic Ekman flow destabilizes the water by bringing denser water over lighter water. The stratification and the Ertel PV are reduced and the frontal structures are strengthened (*Thomas and Lee*, 2005a). Strong atmospheric cooling can also reduce the PV within the mixed layer. Symmetric instability takes its energy from the kinetic and potential energy of the front itself (*Thomas and Taylor*, 2010). Symmetric instability results in strong along-isopycnal shear which can drive secondary Kelvin-Helmholtz instabilities, which can lead to strong dissipation rates (*Taylor and Ferrari*, 2009). Symmetric instability can thus be seen as a mediator of dissipation. *Thomas and Taylor* (2010) carried out high-resolution numerical model simulations and demonstrated that winds blowing in the same direction as the frontal jet force symmetric instability.

These results are of particular importance as they present a new pathway to small scale dissipation via a forward energy cascade associated with submesoscale instabilities. These findings might help to solve the question of how the kinetic energy of the ocean gained by large scale forcing is trans-

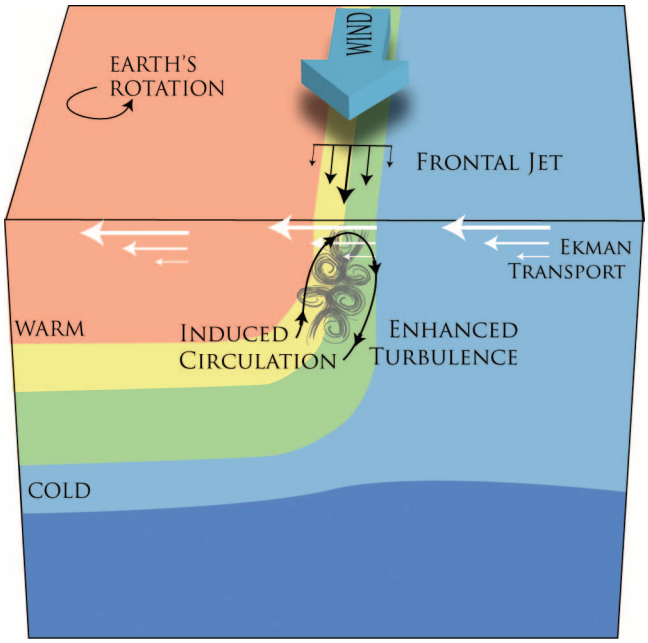

Figure 5: Structure of a symmetrically unstable front on the northern hemisphere. A wind blowing down the frontal boundary between warm and cold water induces an Ekman transport perpendicular to the wind and to the front. This carries heavy water from the cold side of the front over light water from the warm side, which, in the presence of the frontal jet and lateral density gradient, acts to reduce the stratification near the surface and makes the front unstable to symmetric instability. The instability draws energy from the frontal jet, leading to enhanced turbulence, and induces a circulation acting to bring warm water to the surface and cold water to depth, thus counteracting the effect of the Ekman transport and keeping the near-surface stably stratified, with warm water over cold water. Figure and text taken from *D'Asaro et al.* (2011)

ferred to smaller scales in the interior. Recent observational studies are in good agreement with the numerical and theoretical studies mentioned above and show that turbulent mixing processes are increased at frontal regions (*D'Asaro et al.*, 2011).

Little is known about the relative importance of different processes at submesoscale fronts leading to enhanced dissipation. Due to the intermittency of the processes it is difficult to make a global estimate of the overall dissipation of energy due to submesoscale frontal instability processes. *Bruggemann and Eden* (2015) used idealized numerical simulations to investigate kinetic energy pathways in different dynamical regimes. They established a

relationship between the Ri and the strength of the flux of kinetic energy towards smaller scales. In a global high-resolution model simulation they made a global estimate of the ageostrophic downscale energy flux using this Ri dependence. The authors estimated that 0.31 +/- 0.23 TW is transferred to smaller scales due to submesoscale instabilities, which is 31% +/- 23% of the wind power input into geostrophic flows in the ocean (*Wunsch*, 1998).

2.7 Turbulent tracer fluxes in the upper ocean

The aim of this study is to understand the role of meso- and submesoscale processes for the near-coastal oxygen ventilation off Peru. As these processes cause turbulent oxygen fluxes we will introduce different turbulent tracer fluxes in the upper ocean in the following.

Fluxes in the ocean can be caused by mean or time varying motion and are often divided into along-isopycnal and diapycnal fluxes. As isopycnal surfaces act to a first order in the horizontal domain, isopycnal fluxes are often assumed to be horizontal and diapycnal fluxes to be vertical tracer fluxes. However, isopycnal fluxes may also have a strong vertical component if the isopycnals are very steep e.g at frontal regions in the mixed layer.

In order to investigate tracer fluxes in the upper ocean it might be helpful to distinguish between different dynamic origins of the fluxes in a mathematical framework. *Levy et al.* (2012) give a comprehensive overview about the importance of different turbulent terms for tracer evolutions using the Reynolds-averaged equations of motion. These equations are averaged at fixed height over a time and space scale longer and larger than the fluctuations related to mesoscale motion e.g. the first baroclinic Rossby radius. Overbars represent averages and primes indicate meso- and submesoscale eddy fluctuations:

$$\underbrace{\frac{\partial \overline{C}}{\partial t}}_{1} + \underbrace{\overline{u} \cdot \nabla \overline{C}}_{2} = \underbrace{-\nabla_H \cdot \overline{u'C'}}_{3} - \underbrace{\frac{\partial \overline{w'C'}}{\partial z}}_{4} + \underbrace{\frac{\partial}{\partial z}(\overline{K_z \frac{\partial C}{\partial z}})}_{5} + \underbrace{Q_C}_{6} \qquad (1)$$

The temporal local change of the tracer concentration C (1) and the mean advection term related to the mean tracer concentration field (2) is balanced by the following terms:

The horizontal advective Reynolds flux (3) is thought to be dominated by mesoscale motion (*Ledwell et al.*, 1998). One important mechanism for horizontal transport of momentum, mass and passive tracers by eddies is stirring (*Ferrari and Polzin*, 2005). However, *Badin et al.* (2011) point out that in the pycnocline submesoscale mixed layer instabilities are also very efficient for the lateral mixing of passive tracers. This is due to the fact that

mixed layer instabilities do not only effect the mixed layer but also interact with the pycnocline due to meso- and submesoscale coupling (*Ramachandran et al.*, 2014). Note that, mesoscale motion leads to a cascade of tracer variance towards smaller scales and thus can form small scale tracer filaments (*Ferrari and Polzin*, 2005). However, these small-scale tracer filaments are distinct from submesoscale filaments as they are not related to strong density gradients and the associated velocity anomalies, which are found at submesoscale fronts. This fact is important to keep in mind when interpreting small scale tracer distributions since these might be a result of mesoscale stirring of lateral tracer gradients instead of being caused by submesoscale frontal processes. The vertical Reynolds flux term (4) is influenced by meso- as well as submesoscale motion. Within the ocean interior, the mesoscale motion dominates the vertical Reynolds flux. However, close to the ocean surface at submesoscale density fronts, where isopycnals are strongly tilted and outcrop, submesoscale dynamics seem to dominate the fourth term in the equation (*Klein and Lapeyre*, 2009).

The fifth term describes irreversible mixing of different water masses across density layers which is parameterized here as a vertical diffusitivy term, where K_z represent the vertical diffusion coefficient. In the turbulent boundary layers, such as the mixed layer, microscale turbulence is dominant and keeps tracer concentrations homogeneous. The last term (6) describes sinks and sources of the tracers. Typical sinks could be the uptake of nutrients by growing phytoplankton or the consumption of oxygen by bactertia due to the remineralisation of organic matter.

It is important to note, that averaging at fixed height as done by *Levy et al.* (2012) implies that isopycnal mixing cannot be separated clearly from diapycnal mixing (*Eden et al.*, 2007). Thus the vertical Reynoldsterm (4) may also include small amounts of irreversible diapycnal mixing.

2.8 Physical-biogeochemical coupling in meso- and submesoscale flows

The vertical gradients of different oceanic tracers are particularly pronounced near the ocean surface. A vertical tracer profile is generally the result of the balance between local removal and production, advection by the mean flow, horizontal and vertical along-isopycnal eddy fluxes as well as diapycnal fluxes (section 2.7). Most tracers have their largest gradients directly below the mixed layer, where vertical velocities associated with meso- and submesoscale turbulence are also largest (*Capet et al.*, 2008a). Thus understanding the physical - biogeochemical coupling between meso- and submesoscale flows and biogeochemical cycles is crucial (*Klein and Lapeyre*, 2009).

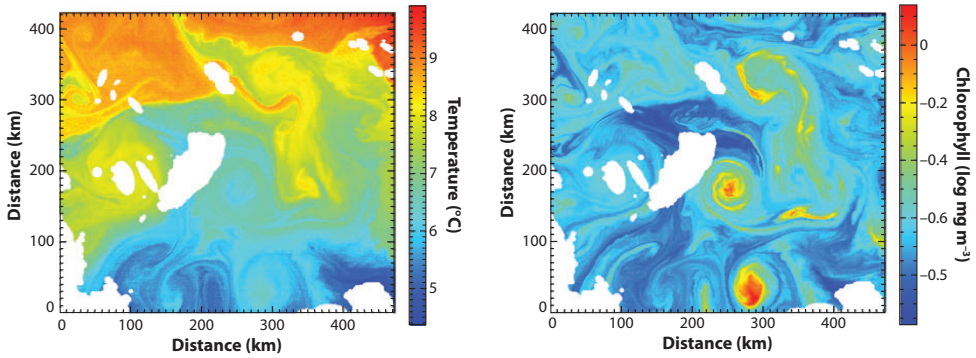

Figure 6: Sea surface temperature (left) and ocean color images (right) from satellite data. Figure and text taken from *Klein and Lapeyre* (2009)

Figure 6 shows images of sea surface temperature (left) and chlorophyll concentration (right) with both meso- and submesoscale features (*Klein and Lapeyre*, 2009). *Jenkins* (1988) calculated nitrate fluxes from the thermocline into the euphotic zone near Bermuda and highlighted the importance of mesoscale vertical biogeochemical tracer fluxes. Nutrient budget calculations indicate the importance of vertical fluxes caused by mesoscale eddies on the global scale (*McGillicuddy et al.*, 2007). However, there exists still a large discrepancy between the annual nutrient consumption for primary production and the supply rate caused by the vertical flux due to wintertime convection and mesoscale fluxes. Thus a large number of studies address this question and there is an ongoing debate about which physical mechanisms can possibly close the nutrient budget (*Garcon et al.*, 2001; *McGillicuddy et al.*, 2003; *Levy*, 2008).

Various model studies have focussed on the impact of mesoscale eddies on biogeochemical cycles. There are two conceptual views on the vertical exchange of biogeochemical tracers. The traditional view focuses on the vertical flux within the eddy interior, where often the strongest signal in sea surface height is present. Most of the existing studies focus on the so-called eddy pumping paradigm related to the dynamics within a mesoscale eddy (*Martin and Richards*, 2001). It states that phytoplankton growth is stimulated within a cyclonic eddy due to a shoaling of isopycnals and the associated upwelling of nutrients, whereas in anticyclonic eddies the isopycnals are deepened and no ecosystem response exists. Several observational based studies confirm the eddy pumping paradigm by showing higher productivity within cyclonic eddies (e.g. *Falkowski et al.*, 1991). Modeling studies with global realistic coupled physical-biogeochemical models resolving the mesoscale eddy field also highlight the importance of the vertical nutrient fluxes associated

with mesoscale eddies and confirm the eddy pumping mechanisms (*Oschlies and Garcon*, 1998; *Oschlies*, 2002; *McGillicuddy et al.*, 2003).

However, recently the focus has shifted to areas at the edges of eddies, between or outside the center of mesoscale eddies. There, vertical flow associated with ageostrophic motion becomes important. This more recent view is motivated by the fact that until now no convergence of model solutions for the biogeochemistry by increasing spatial resolution has been achieved pointing to the importance of sub-grid scale processes (*Mahadevan and Archer*, 2000; *McGillicuddy et al.*, 2003). Furthermore, several physical studies within the last decade found a strong increase in vertical velocities associated with an increasing grid resolution (*Capet et al.*, 2008c; *Levy et al.*, 2012).

Omand et al. (2015) used glider observations and regional high-resolution biogeochemical model simulations in the North Atlantic to show that up to 50% of the total spring bloom particulate organic carbon export is attributed to submesoscale eddy-driven subduction of non-sinking particles from surface water. A very recent study *Brannigan* (2015) used submesoscale permitting model simulations of mesoscale eddies to demonstrate that submesoscale instabilities are responsible for the vertical tracer fluxes within mesoscale eddies. Submesoscale vertical tracer fluxes might be the missing physical mechanism to close the nutrient budget but are not resolved in global biogeochemical models yet. *Glover et al.* (2008) found that about 50% of the total resolved variance of ocean color signal is associated with submesoscale length scales. This also highlights the importance of studying the small scale vertical supply pathways and thereby, learning more about the relative importance of these processes. Especially, experimental studies dealing with this interdisciplinary question are rare.

Whether submesoscale vertical velocities are able to bring nutrients to the euphotic layer depends on their occurrence in regions of strong nutrient gradients. Often the largest vertical velocities are found at the base of the mixed layer, which is often shallower than the nutricline. However, *Levy et al.* (2012) suggests a deeper penetration depth associated with submesoscale processes which might reach the nutricline. One important controlling factor is also the time scale of the associated processes. Submesoscale processes act on time scales O(hours - days) which is of the same order as the time scale of nutrient uptake by phytoplankton. Mesoscale motions are slower O(weeks-months) thus the nutrients stay longer in the euphotic layer, giving the organisms more time to take them up. Submesoscale motion is much faster giving the organisms less time to react. However, *Levy et al.* (2012) state that we are far away from understanding the role of the different time scales of meso- and submesoscale motions and their coupling to biogeochemistry. More research on this topic is clearly required.

3 Observational and model data

3.1 Multi-platform observational study in the Peruvian upwelling regime

The observational part of this thesis is based on a multi-platform observational campaign including research vessel, glider and mooring-based measurements carried out in the Peruvian upwelling regime between 12° and 14°S in January and February 2013. The deployment of seven Slocum gliders provides the backbone of the experiment and resulted in > 15000 profiles of temperature, salinity, oxygen and chlorophyll fluorescence. The extensive dataset allows a detailed high-resolution four-dimensional description of the circulation and tracer distribution found in the study area during the two months period. A detailed description of the experiment including data processing and calibration can be found in section 5.2, being part of a manuscript submitted to the Journal of Geophysical Research - Oceans.

3.2 Regional model simulation of the Peruvian upwelling regime

In addition to the observational dataset, a quasi-equilibrium simulation based on a regional ocean model (ROMS, (*Shchepetkin and McWilliams*, 2005, 2009)) of the Peruvian upwelling region is analyzed to put the instantaneous short term observations in a broader spatial and temporal context. In particular the model output is used to investigate the subduction pathways of newly upwelled water in submesoscale cold filaments. The model domain spans from 16°S to 4.5°S along the coast to about 880 km offshore at a horizontal resolution of 2.2 km and 42 terrain-following vertical levels (sigma coordinates). A detailed description of the model setup, model validation and the Lagrangian experiment can be found in section 6.2.2, being part of a manuscript submitted to the Geophysical Research Letters.

4 Seasonal cycle of the Peruvian upwelling regime

The seasonal cycle of the Peruvian upwelling regime is described in the following section to introduce the study area to the reader. This is done based on satellite observations, *in-situ* glider-measurements and a regional model simulation. The description includes the seasonality of the wind forcing, surface heat fluxes, SST and the near-coastal vertical temperature distributions. In particular, the time-variable mixed layer depth and lateral temperature gradient are investigated, as both parameters are important for the strength of submesoscale variability.

4.1 Wind forcing, surface heat fluxes and sea surface temperature distribution

The Peruvian upwelling regime is characterized by upwelling favourable wind conditions during the whole year (Fig. 7a-d). The southeasterly trades are mainly directed parallel to the Peruvian coastline resulting in an offshore Ekman transport and consequently upwelling of colder subsurface waters (*Strub et al.*, 1998). The signature of upwelling can be seen in a cold SST band along the coast (Fig. 7e-l). However, the strength of the wind forcing exhibits a strong seasonal cycle with minimum (maximum) windstress of 0.07 N/m^2 (0.15 N/m^2) in austral summer (winter) around 15°S and 80°W (Fig. 7a-d). The strength of the wind forcing also exhibits regional differences. During the whole year, strongest winds are found offshore of Cape of Pisco near 15°S. Around Pisco the lowest sea surface temperatures along the Peruvian coast are observed, suggesting an upwelling cell in this area (Fig. 7e-h).

The large scale SST distribution shows a pronounced seasonal cycle in both observations (Fig. 7e-h) and the model simulation (Fig. 7i-l). In summer (January - March), temperatures as high as 26°C and as low as 18°C are observed offshore and along the coast by the satellite measurements (Fig. 7e), respectively. In general much lower temperatures are observed in winter (July - September) where maximum temperatures of only 18°C are found offshore and drop down to 15°C near the coast at 14°S. The amplitude and structure of the seasonal cycle simulated by the model are similar to that of the satellite observations. Some important differences to the observations are present. They will be described in the following (Fig. 7 i-l). During January to March the model SST is too low with a bias of about 1°C offshore and up to 3°C inshore. Between April to June, the model shows a slightly better performance and mainly regional differences of upwelling cells are visible

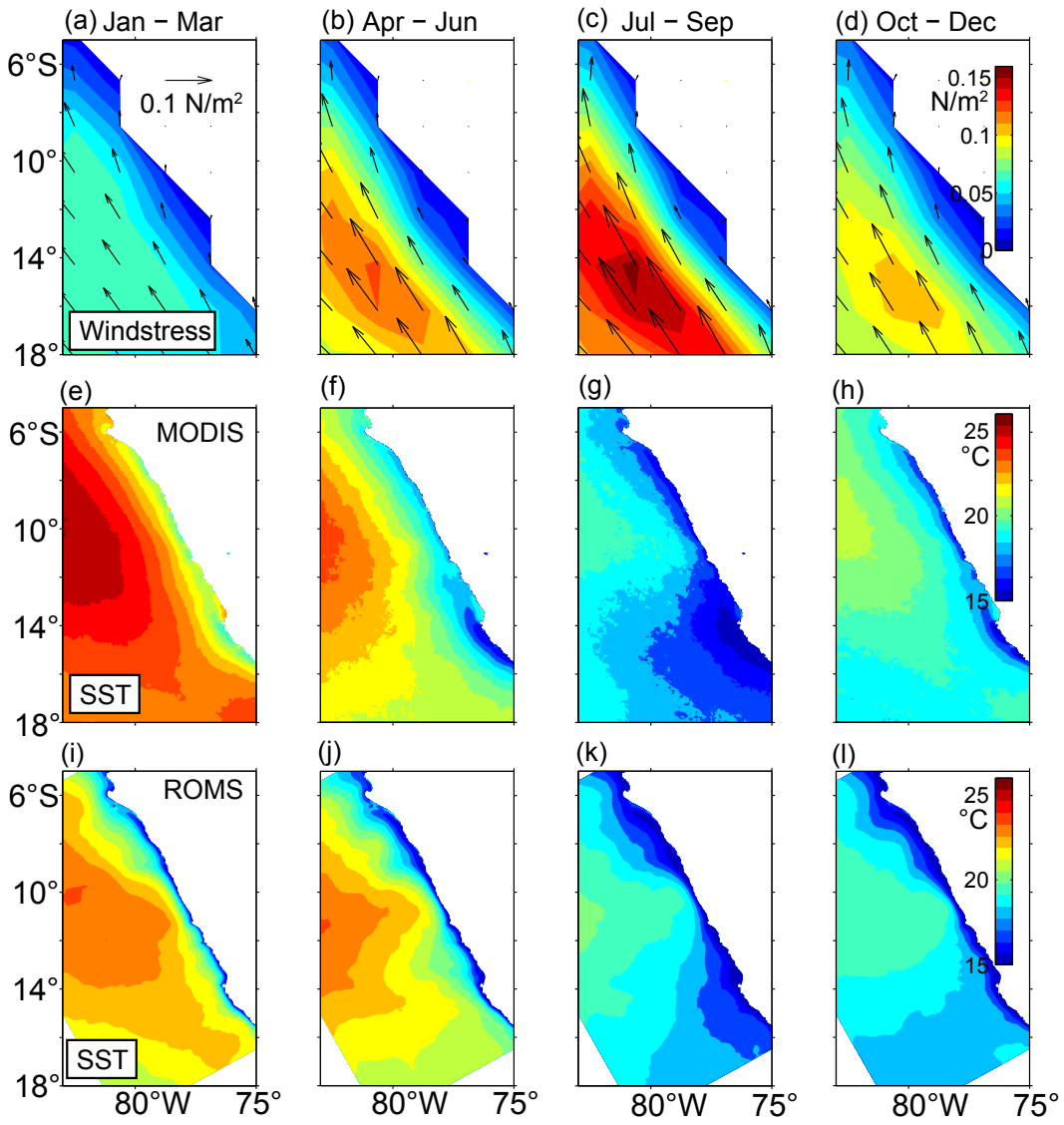

Figure 7: Seasonal windstress in N/m^2 (upper column), sea surface temperature from MODIS in °C (middle column) and modeled (ROMS) sea surface temperature in °C (lower coloumn).

between the observations and the simulation. The upwelling cell near Pisco at 15°S is not well captured by the model leading to increased temperatures within this area. On the other hand, the model shows enhanced upwelling cells in the northern area of the domain, which are not found in the satellite product. During July to September, the model performs quite well and only in the southern domain is a slightly positive temperature bias (~ 1°C) found.

In the following season from October to December, SST in this area is again slightly too low in the model. In summary, the model captures the seasonal cycle of the large scale SST distribution off Peru reasonably well although some differences exist.

The seasonal cycle of the large scale SST distribution is influenced by various processes such as seasonally varying surface fluxes, advection and upwelling strength. It is beyond the scope of this thesis to investigate the overall driving mechanisms of the seasonal cycle of the SST distribution off Peru. Instead we will focus on the comparison of the surface heat fluxes of the summer and winter seasons which is important for the analysis of subduction off Peru in section 6. In summer, positive surface heat fluxes between 80 W/m^2 offshore and 160 W/m^2 inshore are found off Peru (Fig. 8a). This results in a strong warming and buoyancy gain of newly upwelled water (section 6). In the winter time the surface fluxes are negative (down to -40 W/m^2 offshore) enabling newly upwelled water to penetrate into layers denser then their subsurface origin (Fig. 8b). The surface heat fluxes are also important for the depth of the mixed layer which will be investigated in the following section.

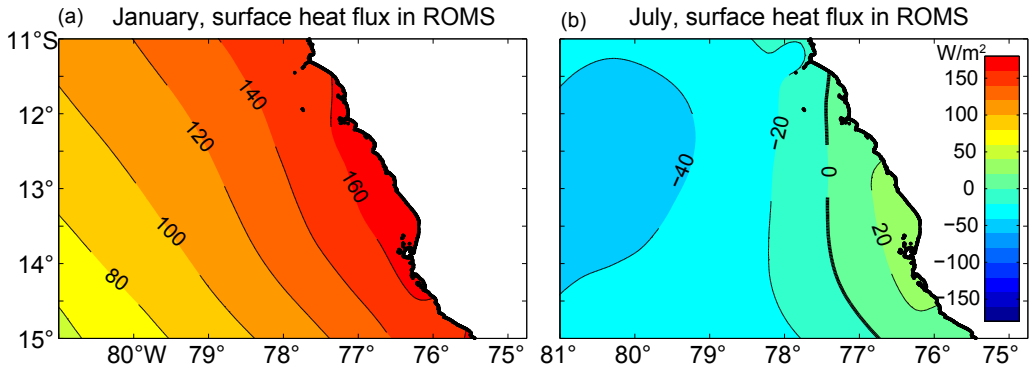

Figure 8: Surface heat fluxes in ROMS simulation in January (left) and July (right) in W/m^2.

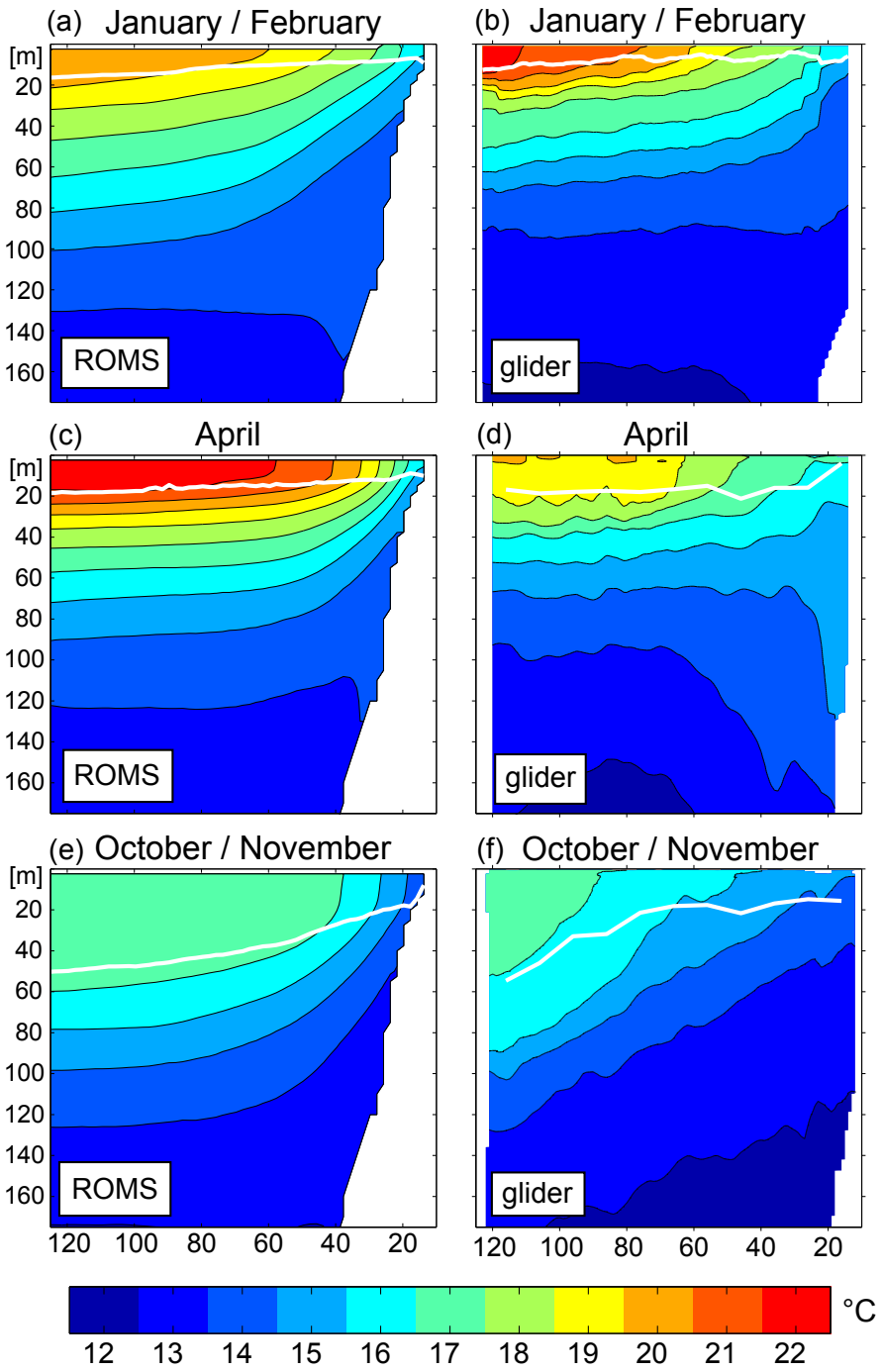

Figure 9: Average vertical temperature distribution along 14°S off Peru ROMS model simulation (left) and from glider observations (right) in January / February (top), April (middle) and October / Novemeber (below). The mixed layer depth, defined here as the depth were the surface temperature minus 0.2°C is found, is shown as a white line.

4.2 Cross-shore temperature distribution

The vertical temperature distribution across the upwelling front off Peru exhibits pronounced changes during the year which will be investigated in this section. Figure 9 shows cross-shore transects near 14°S from glider measurements and model simulations. The glider transects are based on three different observational campaigns consisting of one German study carried out in austral summer 2013 (section 3) and two French studies carried out in austral autumn 2010 (*Pietri et al.*, 2014) and in austral spring 2008 (*Pietri et al.*, 2013). More details on the deployments can be found in the associated publications (*Pietri et al.*, 2013, 2014). The model output has been temporally averaged over 5 years of model output during the period of the year when the glider observations were made. A seasonal cycle in the across-shore temperature distributions is clearly visible in both the observations and the model.

In summer, maximum temperatures of up to 22°C are encountered in the observations and the mixed layer is very shallow (< 10 m). The model simulations are about 1°C colder but they are in agreement with the overall structure of the upwelling front in terms of the lateral density gradient and the isopycnal slope. Even the reversal of the isopycnal slope at around 100 m depth is well captured by the model. In April, temperatures of around 20°C and 16°C are found in the observations offshore and near the coast, respectively. The positive temperature bias offshore causes a positive bias in the lateral temperature gradient in the model. The differences between the model and observations may be explained by the fact that the model does not capture the locally intensified upwelling cell at 15°S near Pisco as discussed in section 4.1. In October, near-surface temperatures of about 17°C (14°C) are found offshore (inshore) in both the observations and the model simulations. However, in the model simulations the upwelling front is much narrower associated with much stronger lateral temperature gradients, whereas in the observations a much broader upwelling front is found.

It is important to note that the single year glider observations do not represent a mean climatological perspective. The measurments also include large intra-seasonal and inter-annual variability. For example a coastal trapped wave, which results in strong upwelling and lower near surface temperatures off Peru, was observed in April (Fig. 10c), as described in detail in *Pietri et al.* (2014). However, the glider data is used here for comparison, because their high horizontal resolution allows a detailed view on the upwelling front structure at small scales, which is not possible with coarse resolution climatologies.

An important feature of the Peruvian upwelling regime is that the sea-

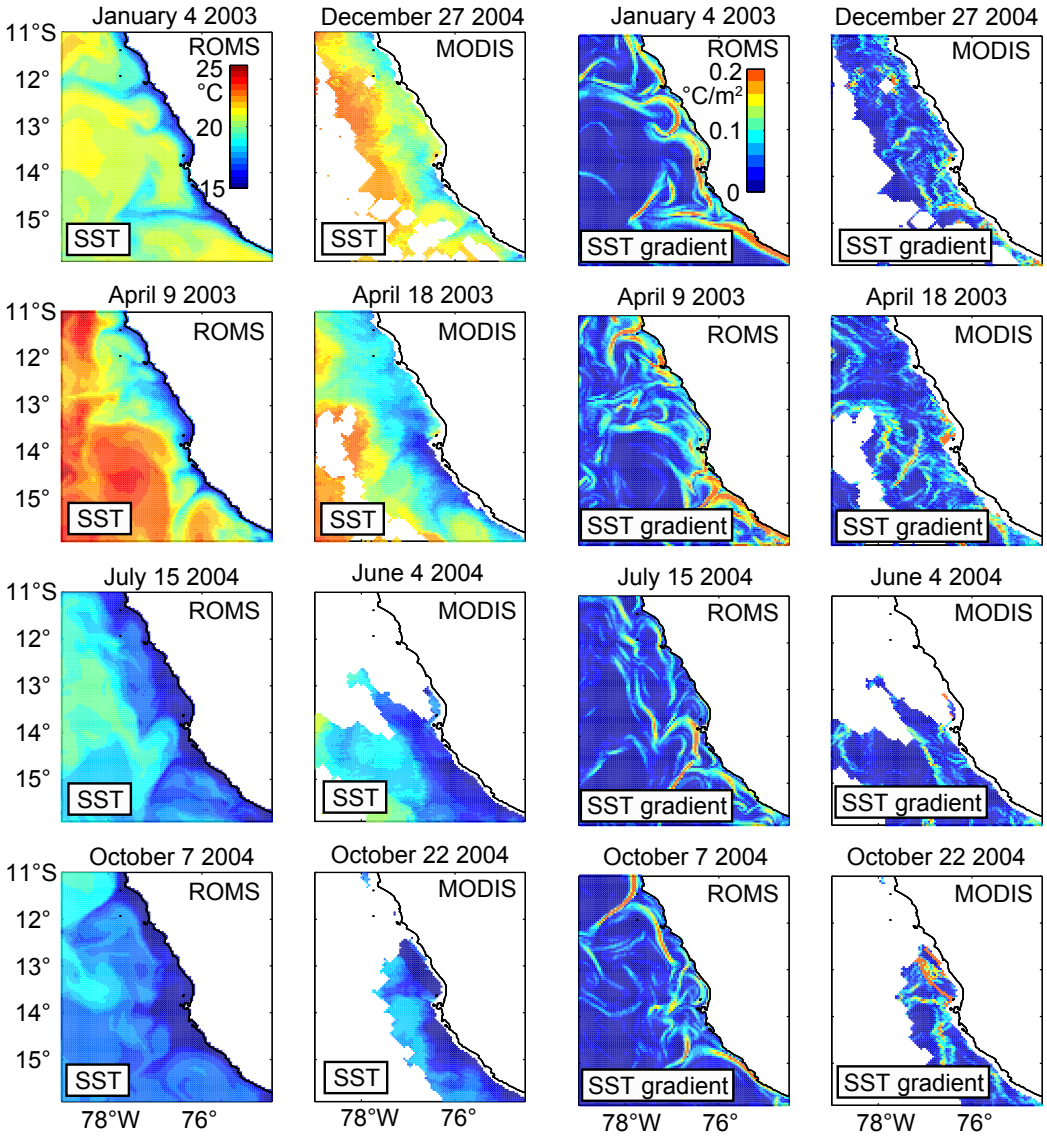

Figure 10: Daily snapshots of observed (MODIS Aqua/Terra satellite, left column) and modeled (ROMS, 2nd column) sea surface temperature and observed (3rd column) and modeled (4th column) magnitude of the sea surface temperature gradient ($|\nabla SST| = ((\partial SST/\partial x)^2 + (\partial SST/\partial y)^2)^{1/2}$).

sonal chlorophyll maximum is observe in austral summer (*Echevin et al.*, 2008). Thus it does not coincide with strongest upwelling in winter, when the wind forcing is highest. The seasonality of the mixed layer depth, which is shallowest in austral summer and deepest in winter, and the associated dilution effect can explain this apparently paradoxical seasonal cycle (*Echevin*

et al., 2008). Close to the coast, mixed layer depths between 10 - 20 m are found during January / February (Fig. 9a,b). In October / November, the mixed layer can be up to 60 m deep (Fig. 9f).

4.3 Submesoscale variability

The lateral temperature gradients off Peru exibit a clear seasonal cycle (*Vazquez-Cuervo et al.*, 2013). Maximum values are reached in April just after the summer season when the winds start to increase. Both the seasonal cycle of the mixed layer depth (*Penven et al.*, 2005) and the lateral temperature gradient are of major importance for the seasonal cycle of submesoscale variability, because a stronger lateral buoyancy gradient and a deeper mixed layer results in enhanced submesoscale variability (*Fox-Kemper and Ferrari*, 2008). Consequently, we expect to find enhanced submesoscale variability during April and May.

Figure 10 shows daily snapshots of SST and SST gradients off Peru for four different seasons. In each season filaments and strong SST fronts are present, which indicates that submesoscale processes are an important part of the SST variability found off Peru. The sharpest SST gradients are found within a 200 km band along the coast associated with cold filaments. Using these daily snapshots, it is difficult to describe a seasonal cycle quantitatively.

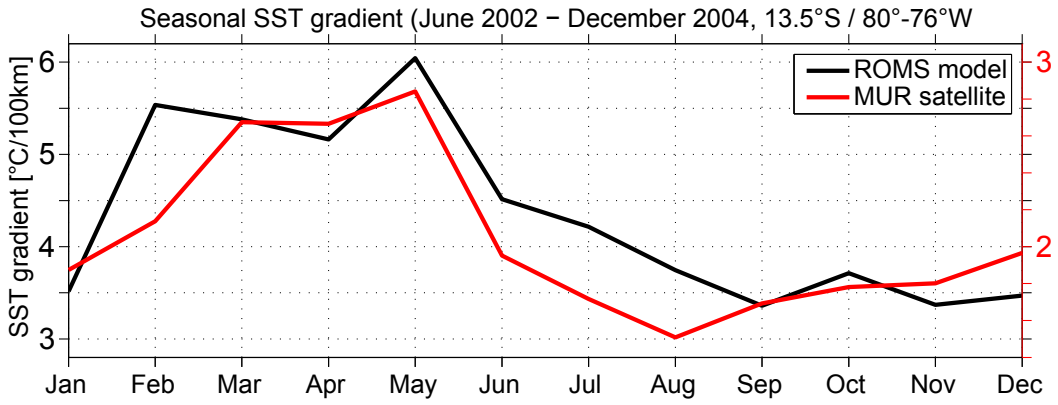

Figure 11: Seasonal cycle of magnitude of SST gradient ($|\nabla SST| = ((\partial SST/\partial x)^2 + (\partial SST/\partial y)^2)^{1/2}$) in ROMS model (black) and Multi-scale Ultra-high Resolution (MUR) satellite observations (red) averaged along a line at 13.5°S between 80° - 76°W. Note the different scales of the y-axis.

Vazquez-Cuervo et al. (2013) analyzed various SST products and found a pronounced seasonal cycle of the SST gradients, which can be associated

with submesoscale fronts and is therefore used as a proxy for submesoscale variability here. Following *Vazquez-Cuervo et al.* (2013), the lateral SST gradients are calculated from satellite observations and are compared to the high-resolution model output. The Multi-scale Ultra-high Resolution (MUR) SST product (http://mur.jpl.nasa.gov) is used for the calculation, as it represents the only product which has data at all locations during all days. A clear seasonal cycle of the SST gradient is present in both the MUR satellite observations and the ROMS simulations (Fig. 11). The satellite based estimates peak in May with maximum values of 2.8°C/100 km and the ROMS model SST gradient also peaks in May but with values of up to 6°C/100 km. Minimum values are found in August (MUR 1.5°/100 km) and September (ROMS 3.4°C/100 km). The timing of the seasonal cycle is well captured by the model but the absolute values of the SST gradients are about 2 times higher compared to the MUR data set. Given that the MUR product commonly uses low resolution satellite measurements (microwave) when clouds are present and thus no high-resolution infrared measurements are available it probably underestimates the real SST gradients on average.

Snapshots of daily MODIS SST data (infrared) show similar magnitudes of SST gradients compared to the model data (Fig. 10). Hence it is assumed that the large difference between the gradients based on the MUR product and the model is mainly caused by too low gradients in the MUR product. Similar results were found by *Colas et al.* (2012), where probability density functions of SST gradients based on satellite observations were compared with ROMS model output.

4.4 Summary

Both observations and model show a pronounced seasonal cycle of the lateral and vertical temperature distribution off Peru. We showed that some differences exists between the modeled and observed temperature distribution. However, the model captures the seasonally changing SST distribution relatively well and especially the timing of the seasonal cycle in the lateral temperature gradient (Fig. 11). Furthermore, the seasonally changing mixed layer depth, which is another important parameter for the strength of submesoscale variability, is well captured by the model (Fig. 9).

5 The formation of a subsurface anticyclonic eddy in the Peru-Chile Undercurrent and its impact on the near-coastal salinity, oxygen and nutrient distributions

Sören Thomsen, Torsten Kanzow, Gerd Krahmann, Richard J. Greatbatch, Marcus Dengler, Gaute Lavik[1]

Abstract

The formation of a subsurface anticyclonic eddy in the Peru-Chile Undercurrent (PCUC) in January and February 2013 is investigated using a multi-platform four-dimensional observational approach. Research vessel, multiple glider and mooring-based measurements were conducted in the Peruvian upwelling regime near 12°30'S. The dataset consists of $>$ 10000 glider profiles and repeated vessel-based hydrography and velocity transects. It allows a detailed description of the eddy formation and its impact on the near-coastal salinity, oxygen and nutrient distributions. In early January, a strong PCUC with maximum poleward velocities of $\sim$ 0.25 m/s at 100 to 200 m depth was observed. Starting on January 20 a subsurface anticyclonic eddy developed in the PCUC downstream of a topographic bend, suggesting flow separation as the eddy formation mechanism. The eddy core waters exhibited oxygen concentrations $< 1\,\mu$mol/kg, an elevated nitrogen-deficit of $\sim 17\,\mu$mol/l and potential vorticity close to zero, which seemed to originate from the bottom boundary layer of the continental slope. The eddy-induced across-shelf velocities resulted in an elevated exchange of water masses between the upper continental slope and the open ocean. Small scale salinity and oxygen structures were formed by along-isopycnal stirring and indications of eddy-driven oxygen ventilation of the upper oxygen minimum zone were observed. It is concluded that mesoscale stirring of solutes and the offshore transport of eddy core properties could provide an important coastal open-ocean exchange mechanism with potentially large implications for nutrient budgets and biogeochemical cycling in the oxygen minimum zone off Peru.

5.1 Introduction

The Peruvian upwelling system is characterized by permanent Ekman-driven coastal upwelling forced by sustained trade winds largely parallel to the Pe-

[1]This section has been submitted as a manuscript to Journal of Geophysical Research - Oceans and is currently under review.

ruvian coastline (*Strub et al.*, 1998). The upwelling brings cold and nutrient rich water to the surface resulting in a band of low sea surface temperatures and high primary production along the coast (*Pennington et al.*, 2006). It is one of the most productive areas of the world ocean and consequently of great economic and scientific interest. Despite covering only 0.1% of the world ocean surface about 10 % of the world fish catch occurs in the Peruvian upwelling system (*Chavez et al.*, 2008). Being one of the four major eastern boundary upwelling systems, the Peruvian upwelling regime comprises one of the largest oxygen mininum zones (OMZs) (*Karstensen et al.*, 2008; *Fuenzalida et al.*, 2009; *Paulmier and Ruiz-Pino*, 2009). A combination of poor ventilation of thermocline water masses and enhanced microbial subsurface respiration induced by high primary production and the associated export of organic matter results in an OMZ characterized by dissolved oxygen concentration of less than 1 μmol/kg (*Revsbech et al.*, 2009; *Kalvelage et al.*, 2013). The oxycline depth off Peru is often very shallow and varies between 10 m and 80 m (*Hamersley et al.*, 2007; *Gutiérrez et al.*, 2008). Due to the low oxygen concentrations, the Peruvian upwelling system is considered to be an important region for oceanic nitrogen-loss (*Cline and Richards*, 1972; *Codispoti and Packard*, 1980; *Hamersley et al.*, 2007; *Gruber*, 2008; *Lam et al.*, 2009).

The near-coastal current system off Peru is mostly wind-driven (*Gunther*, 1936; *Strub et al.*, 1998). Two currents, the Peru Coastal Current and the Peru-Chile Undercurrent (PCUC), are of relevance for this study. The Peru Coastal Current flows equatorward in the Ekman layer at the surface (*Penven et al.*, 2005). Below this surface current, the subsurface PCUC flows poleward with a mean core speed of 0.10 - 0.15 m/s at 100 to 150 m depth between 12°S and 15°S (*Wyrtki*, 1963, 1967; *Brink et al.*, 1983; *Huyer et al.*, 1991; *Strub et al.*, 1998; *Penven et al.*, 2005; *Kessler*, 2006; *Colas et al.*, 2012; *Chaigneau et al.*, 2013).

The Peruvian upwelling system encompasses pronounced mesoscale variability (*Penven et al.*, 2005), which is the focus of this study. Based on 15 years of altimeter data, *Chaigneau et al.* (2008) show that coherent mesoscale eddies off Peru are generated near the coast and subsequently propagate westward. *Chaigneau et al.* (2013) use Argo float-based CTD data to show that anticyclones (cyclones) tend to have their cores located below (within) the thermocline. They suggest that anticyclones might be formed by instabilities of the PCUC and cyclones by instabilities of the equatorward surface currents. Based on regional eddy-resolving model simulations, *Colas et al.* (2012) find a skewness of vorticity towards anticyclonic rotation between 100 and 150 m depth off Peru. The authors relate this vorticity dominance to subsurface anticyclonic coherent vortices and suggest that they arise from in-

stability of the PCUC. These eddies, traditionally referred to as submesoscale coherent vortices, may exhibit a wide range of sizes. Yet, they are in general smaller than the first baroclinic Rossby radius of deformation (*McWilliams*, 1985). Different nomenclatures for subsurface anticyclonic eddies with convex lense shaped density field found off Peru and Chile have been used in the recent literature e.g. Equatorial Pacific 13° water eddies (*Johnson and McTaggart*, 2010), subsurface anticyclonic coherent vortices (*Colas et al.*, 2012), intra-thermocline eddies (*Hormazabal et al.*, 2013; *Combes et al.*, 2015) and mode-water eddies (*Stramma et al.*, 2013). Here, we use the term subsurface anticyclonic eddy because two important eddy characteristics are automatically defined with this term.

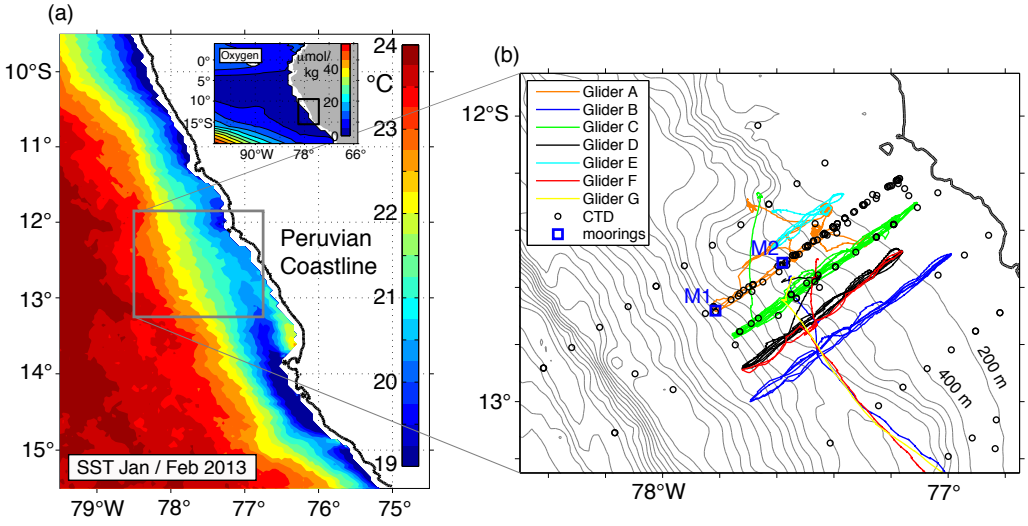

Figure 12: Mean sea surface temperature off Peru during January and February 2013 from remote sensing (Modis Aqua/Terra) is color shaded (a, large panel). The small inlet shows oxygen concentration in μmol/kg in the eastern tropical Pacific at $\sigma_\theta = 26.8\, kg/m^3$ as obtained from the MIMOC climatology (*Schmidtko et al.*, 2013) (a, small inlet). The right panel (b) shows the water depth (grey contours, 200 m interval), glider tracks (colored lines), conductivity temperature and depth (CTD) stations (black circles) and the two mooring positions (blue squares).

Submesoscale coherent vortices are observed at various places in the world ocean (*McDowell and Rossby*, 1978; *D'Asaro*, 1988; *Karstensen et al.*, 2015; *Bosse et al.*, 2015) and are often shed by boundary currents near sharp topographic bends (*Bower et al.*, 1995, 1997; *Bosse et al.*, 2015; *Molemaker et al.*, 2015). Their generation mechanism is puzzling and studies investigating this phenomena have a long history (*McWilliams*, 1985; *D'Asaro*, 1988; *Prater*, 1992). Based on submesoscale-resolving model simulations *Molemaker et al.* (2015) shows the complexity of the eddy generation mechanism. It includes flow-separation, upscale transport of kinetic energy, submesoscale instabilities and small scale dissipation. The study further highlights the important role of the dissipative bottom boundary layer for the generation of anticyclonic vorticity and of low potential vorticity water, that is found in the core of these eddies. These aspects have also been suggested in the conceptual model of *D'Asaro* (1988).

Mesoscale eddies have large effects on the horizontal and vertical transport of momentum, heat and tracers (*Klein and Lapeyre*, 2009). They strongly influence the near-surface chlorophyll distribution and biological productivity through various mechanisms and can enhance biological production in low-nutrient regions (*Jenkins*, 1988; *Falkowski et al.*, 1991; *McGillicuddy et al.*, 1998; *Oschlies and Garcon*, 1998; *McGillicuddy et al.*, 2007; *Gaube et al.*, 2014). In eastern boundary upwelling regions, eddies are thought to induce a net reduction of biological productivity by exporting nutrients from the productive near-coastal region into the open ocean (*Rossi et al.*, 2008, 2009; *Lathuilière et al.*, 2010; *Gruber et al.*, 2011).

OMZs are characterized by a sluggish mean circulation and thus mesoscale eddies are important for ventilating OMZs by means of along-isopycnal stirring (*Wyrtki*, 1962; *Luyten et al.*, 1983b,a; *Stramma et al.*, 2010; *Hahn et al.*, 2014; *Brandt et al.*, 2015). *Holte et al.* (2013) describe the vertical structure of cyclones and anticyclones in the southeast Pacific based on *in-situ* measurements. They find that both types of eddies may trap coastal waters and transport them towards the open ocean. Subsurface anticyclonic eddies originating from the continental margin found in the open ocean OMZ off Peru and Chile can exhibit distinct physical and biogeochemical water mass anomalies such as low oxygen concentrations and elevated nitrogen-deficits (*Stramma et al.*, 2013, 2014). *Kalvelage et al.* (2013) carried out nitrogen budget calculations based on nutrient measurements, experimentally determined nitrogen transformation rates and modeled export production for the eastern tropical South Pacific. They state that a large export of nitrogen-deficient shelf waters into the open ocean OMZ is required to close their nitrogen budget. Near-coastal observations showing the eddy formation together with its initial physical and biogeochemical properties and subsequently the

Table 1: Glider acronyms, measurement periods, number of profiles and maximum diving depth. Please note that for glider B, F and G only profiles and maximum diving depths during their presence north of 13°15' S have been considered.

glider	measurement period	profiles	max. depth [m]
A	Jan. 7 - 25, Jan. 27 - Feb. 28	2593	450
B	Jan. 18 - Feb. 16	2599	200
C	Jan. 7 - Mar. 1	3099	200
D	Jan. 24 - Feb. 18	1042	735
E	Jan. 15 - 25	480	450
F	Jan. 17 - 30	761	305
G	Jan. 16 - 20	179	305

impact of these eddies on the near-coastal OMZ have, however, until now not been available.

This study is based on multi-platform observations including research vessel, glider and mooring-based measurements carried out off Peru near 12°30'S in January and February 2013. The extensive dataset allows a detailed high-resolution four-dimensional description of the formation of a subsurface anticyclonic eddy occurring in the study area and its impact on the distribution of properties in the water column along the continental margin. The paper is structured as follows. In the next section the different datasets used in this study and the data processing are explained. The oceanographic setting is described in section 5.3.1. Subsequently, the eddy formation chronology is shown in section 5.3.2 and the formation mechanism is discussed in section 5.3.3. In section 5.3.4 the changes in the salinity and oxygen distributions are directly related to the changing horizontal flow field, including the role of the eddy for the ventilation of the near-coastal OMZ off Peru. In section 5.3.5 we investigate the impact of the horizontal circulation on the nutrient distribution. In section 5.4 we discuss our results and relate them to other recent studies. This is followed by a short summary and conclusions in section 5.5.

5.2 Data and methods

In January and February 2013, a multi-platform four-dimensional observational experiment was conducted in the Peruvian upwelling system between 12°S and 14°S to investigate the near-coastal meso- and submesoscale variability. In this study we focus on measurements conducted in an area of $\sim$ 100 km by $\sim$ 100 km centered near 12°30'S (Figure 12). The experiment

was carried out in the framework of the interdisciplinary "SFB 754 Climate-Biogeochemistry Interactions in the Tropical Ocean" project and included research vessel, multiple glider and mooring-based measurements.

A multiple glider survey with seven Slocum gliders (Teledyne Webb Research) is the central component of the multi-platform approach (*Rudnick et al.*, 2004; *Testor et al.*, 2010). The first glider was deployed January 7, 2013 during the R/V Meteor cruise 92 (M92, January 5 - February 3) and the last glider was recovered March 1, 2013 during the R/V Meteor cruise 93 (M93, February 7 - March 9). See Table 1 for more details.

A conductivity, temperature and depth (CTD) cell is mounted on each glider operating at a sampling rate of 1 Hz. Most gliders are equipped with an unpumped CTD (glider G used a pumped CTD). Therefore it is important to correct for the thermal mass of the conductivity cell in order to obtain reliable salinities (*Johnson et al.*, 2007). In this study two methods are combined to provide the correction, which depends on the flushing rate of the conductivity cell, which in turn depends on the glider's speed through the water. The thermal mass correction by *Garau et al.* (2011) is applied, however using a modeled velocity, instead of the glider velocity, calculated from the temporal derivative of pressure. This modeled velocity is estimated using the flight model of *Merckelbach et al.* (2010). This approach eliminates the influence vertical motion of the glider stemming from internal waves. These vertical motions are observed by the glider's pressure sensor but are not associated with forward movements of the glider. Thus they do not lead to changes of the flushing rate used for the thermal mass correction. Internal wave motion is large in the coastal zone of the study area. Parameters such as conservative temperature, absolute salinity and density are calculated using the Thermodynamic Equation Of Seawater - 2010 Matlab Toolbox Version 3.04 (*McDougall and Barker*, 2011).

Aanderaa optodes are mounted on the tail of the gliders to measure concentrations of dissolved oxygen. Following *Hahn et al.* (2014) a two point lab calibration (0 % and 100 % saturation) of the optodes was carried out on the ship after the deployment. Optodes on gliders exhibit response times between 5 - 175 s (*Bittig et al.*, 2014), which result in a hystereses between up- and downcasts. These response times were estimated by minimizing the difference of oxygen in up- and downcasts. Finally, shipboard CTD profiles close to the glider measurements were used to determine and remove offsets in the final temperature, salinity and oxygen measurements. The corrected sensor data was gridded on a one decibar vertical grid. The gliders have maximum diving depths between 200 m and 735 m (Table 1). About one dive (two profiles) was carried out per hour by each glider with lateral resolutions of about 200 m to 1 km depending on the maximum diving depth

of the individual glider. This resulted in about 10750 glider CTD profiles within the study area during the two month deployment (Table 1).

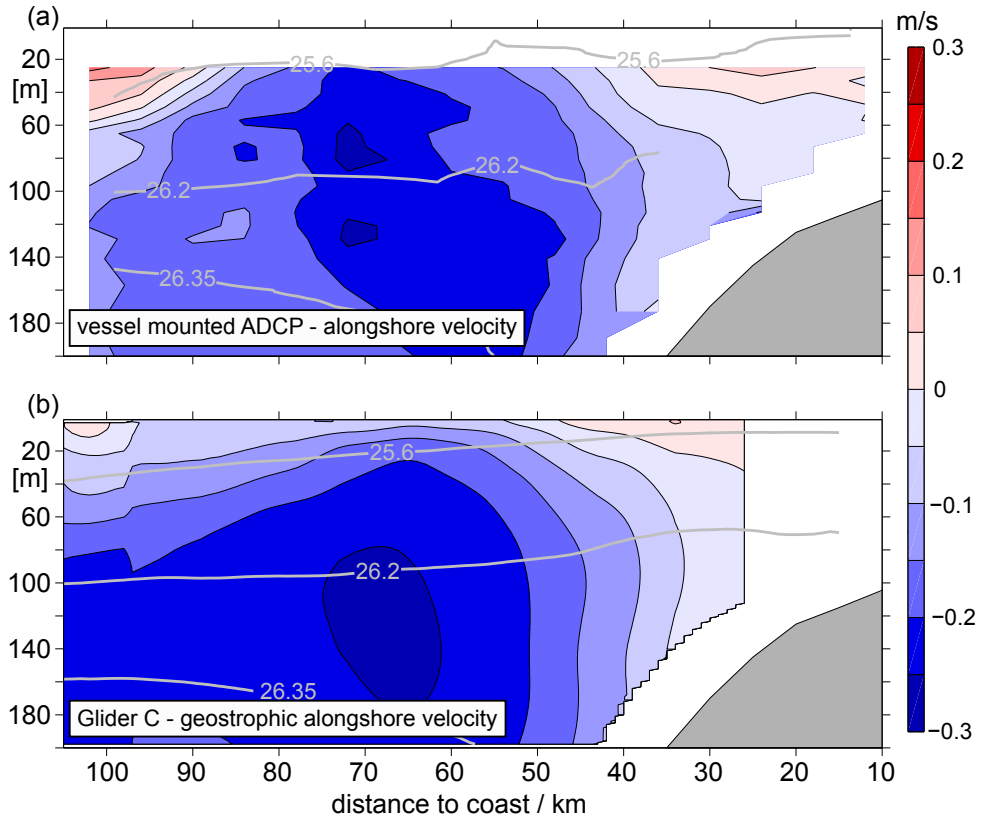

Figure 13: The poleward flow within the Peru-Chile Undercurrent across 12°30'S as observed by the vessel mounted ADCP and glider C between January 10 and 15. The alongshore velocity observed by vmADCP measurements (upper panel) and geostrophic velocity calculated from glider based hydrography measurements and referenced by the depth averaged velocities computed from the vehicle displacement between two dives (lower panel). Positive/negative velocities correspond to equatorward/poleward (into/out of the page) flow. The black contours have a spacing of 0.05 m/s. Isopycnals are denoted by grey lines.

Gliders can also be used to infer horizontal circulation (*Pietri et al.*, 2013, 2014). The difference between the dead-reckoned and the actual surfacing position of the gliders is used to infer the horizontal depth-averaged velocity between two surfacings, which then is used to reference the relative cross-track geostrophic velocities calculated from the glider-based hydrographic CTD measurements. To reduce the influence of ageostrophic short term sig-

nals (e.g. tides and internal waves) the density field and the depth-averaged velocities have been smoothed prior to calculating the geostrophic shear by a simple rectangular window of 25 km similar to *Pietri et al.* (2013, 2014).

The horizontal circulation was measured by two vessel mounted acoustic doppler current profilers (vmADCPs) during both cruises M92 and M93. The 38 kHz and 75 kHz ocean surveyor ADCPs (Teledyne RD Instruments) cover depth ranges between 17 m to 800 m and 11 m to 245 m, respectively. The standard bin size of the ADCPs was set to 16 m for the 38 kHz ADCP and to 8 m for the 75 kHz, and the ping rates for both instruments were 2-3 s. On the shelf, referred here to water depths shallower than 200 m, the 75 kHz ADCP was occasionally set to 4 m bins to achieve a higher vertical resolution. A comparison of the vmADCP velocity measurements and the glider-based estimates of the geostrophic flow within the PCUC between January 10 and 15 is shown in Fig. 13. In both estimates the PCUC core has a speed of ~ 0.25 m/s with the core being located between $100 - 150$ m depth about 70 km away from the coast. Differences between the two estimates are most pronounced close to the surface. The roots-mean-square difference does not exceed 0.05 m/s below 50 m but increases to 0.1 m/s at 25 m depth. This is likely due to ageostrophic processes, which are more important close to the surface. Furthermore, both platforms did not observe the highly variable flow field at exactly the same time.

A lowered SeaBird SBE 9-plus CTD system equipped with two sets of pumped sensors measuring conductivity, temperature and oxygen at 24Hz was used during M92/M93. The CTD was mounted on a General Oceanics rosette with 24 bottles (10l) which where used to take discrete water samples for sensor calibration and biogeochemical parameters. Salinity samples were measured on board with a Guildline Autosal 8 model 8400B salinometer to calibrate the sensor based salinity measurements. The calibrated absolute salinity measurements have an accuracy of 0.002 g/kg. The CTD oxygen sensor was calibrated by a combined approach using Winkler titration of discrete water samples obtained from the rosette (*Winkler*, 1888; *Grasshoff et al.*, 1983) and STOX (Switchable Trace amount OXygen) sensor measurements at low oxygen concentrations (*Revsbech et al.*, 2009; *Kalvelage et al.*, 2013). Note that the classical Winkler titration method is not reliable at oxygen concentrations found in the Peruvian OMZ core and results in too high oxygen estimates. To minimize this bias we only used Winkler samples showing oxygen concentrations > 20 μmol/kg. The STOX sensor shows oxygen concentrations of about 0.01 - 0.05 μmol/kg in the OMZ core, which are use to calibrate the CTD oxygen sensor at these depths and resulted in an overall accuracy of the CTD oxygen data of about 1 μmol/kg. Nutrient concentrations were determined onboard the ship by autoanalyzer (Quaatro

from Seal Analytical) using standard photometric methods (*Grasshoff et al.*, 1983).

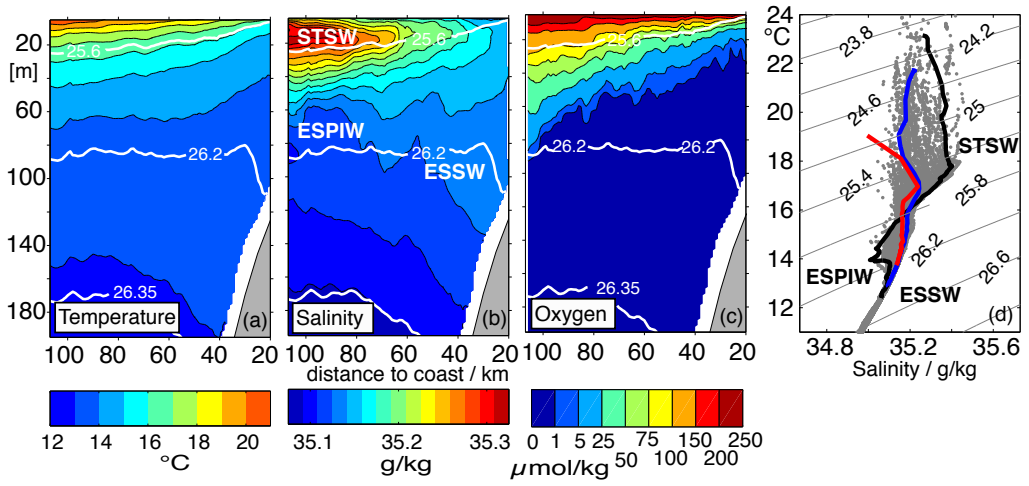

Figure 14: Mean conservative temperature in °C (a), absolute salinity in g/kg (b) and dissolved oxygen (nonlinear color scale) in μmol/kg (c) distributions near 12°30'S between January 10 and February 27 measured by glider C (Fig. 12b). Twelve transects have been horizontally smoothed on a 1 km grid by a rectangular 5 km running mean window and subsequently temporally averaged. Isopycnals are contoured in white. All CTD measurements are shown with grey dots in the T/S diagram (d). The following water masses: Subtropical Surface Water (STSW), Eastern South Pacific Intermediate Water (ESPIW) and Equatorial Subsurface Water (ESSW) are marked in (b) and (d). Three representative glider profiles (offshore (black), (blue) and upper shelf (red)) are overlaid and can be found in the transect in Figure 21h.

For this study, data from two moorings, subsequently referred to as M1 and M2 are analyzed (see blue squares in Fig. 12b). They were deployed during M92 in January 2013 on the continental slope off Peru at 700 m and 1700 m water depth, 12°30.8' S; 77°34.8' W and 12°40.0' S; 77°48.9' W, respectively. Both moorings were recovered during M93 at the end of February 2013. M1 was equipped with an upward looking ADCP (RDI, 300 kHz) at 123 m depth which measured the horizontal velocity every minute in 4 m bins over the depth range of 17 m to 117 m. M2 was equipped with an upward looking ADCP (long ranger RDI, 75 kHz) at 328 m depth measuring the horizontal velocity every 3 minutes in 4 m bins between 55 m and 300 m.

5.3 Results

5.3.1 Oceanographic setting

Being typical for the summer season, moderate southeasterly winds where observed during the two cruises within the study area. Close to the coast (< 50 km) generally weak winds of 5 m/s in the mean (often below 1 m/s) were measured. Further offshore the winds increased to 9 m/s at 150 km distance from the coast (not shown). At the beginning of our measurement campaign, from January 10 - 15 2013, a strong PCUC with maximum poleward alongshore velocities of $\sim$ 0.25 m/s between 100 and 200 m depth was observed extending from the textbfupper continental slope at 400 m water depth to about 80 km offshore (Fig. 13). A near-surface current is seen to be most pronounced around 90 - 100 km offshore with equatorward velocities of up to 0.1 m/s, possibly associated with the Peru Coastal Current (Fig. 13). On the shelf, at water depths shallower than 150 m, the flow is southwestward with velocities lower than 0.1 m/s.

During January and February, different water masses are encountered along the main transect near 12°30'S off Peru (glider C, Figs. 12b and 14). Near surface temperatures reach maximum values of 21.5°C at 100 km offshore and decrease to about 17°C towards the coast. As is typical for the summer season in this region the thermocline is very shallow and no surface mixed layer is discernible (Fig. 14a). About 80 km offshore, a subsurface salinity maximum of about 35.3 g/kg is found within the thermocline at 20 m depth (Fig. 14b). The salinity maximum can be associated with Subtropical Surface Water (STSW, Fig. 14b,d). This is a highly oxygenated water mass found both in the mixed layer and the upper thermocline off Peru originating from the eastern flank of the subtropical gyre (*Wyrtki*, 1967; *Karstensen and Quadfasel*, 2002; *Fiedler and Talley*, 2006; *Silva et al.*, 2009). Below the thermocline, the relatively salty and low-oxygen Equatorial Subsurface Water resides (ESSW, Fig. 14b,d), which is transported southward in the PCUC (*Gunther*, 1936; *Fonseca*, 1989; *Silva et al.*, 2009; *Montes et al.*, 2010). In the same density range as the ESSW but offshore, the Eastern South Pacific Intermediate Water (ESPIW, Fig. 14d) is present. The ESPIW originates off southern Chile and is characterized by a distinct salinity minimum in the T/S diagram at densities of about $\sigma_\theta = 26\,kg/m^3$ (*Schneider et al.*, 2003). It has also been referred to as Shallow Salinity Minimum Water (*Karstensen*, 2004). For simplicity we shall refer to STSW and ESPIW in most cases just as high and low salinity water masses, respectively. The oxygen concentrations are highest close to the surface with mean values of up to 240 μmol/kg (Fig. 14c). They decrease rapidly with depth and are < 1 μmol/kg below $\sim$ 30 m on the shelf and at $\sim$ 80 m further offshore, respectively.

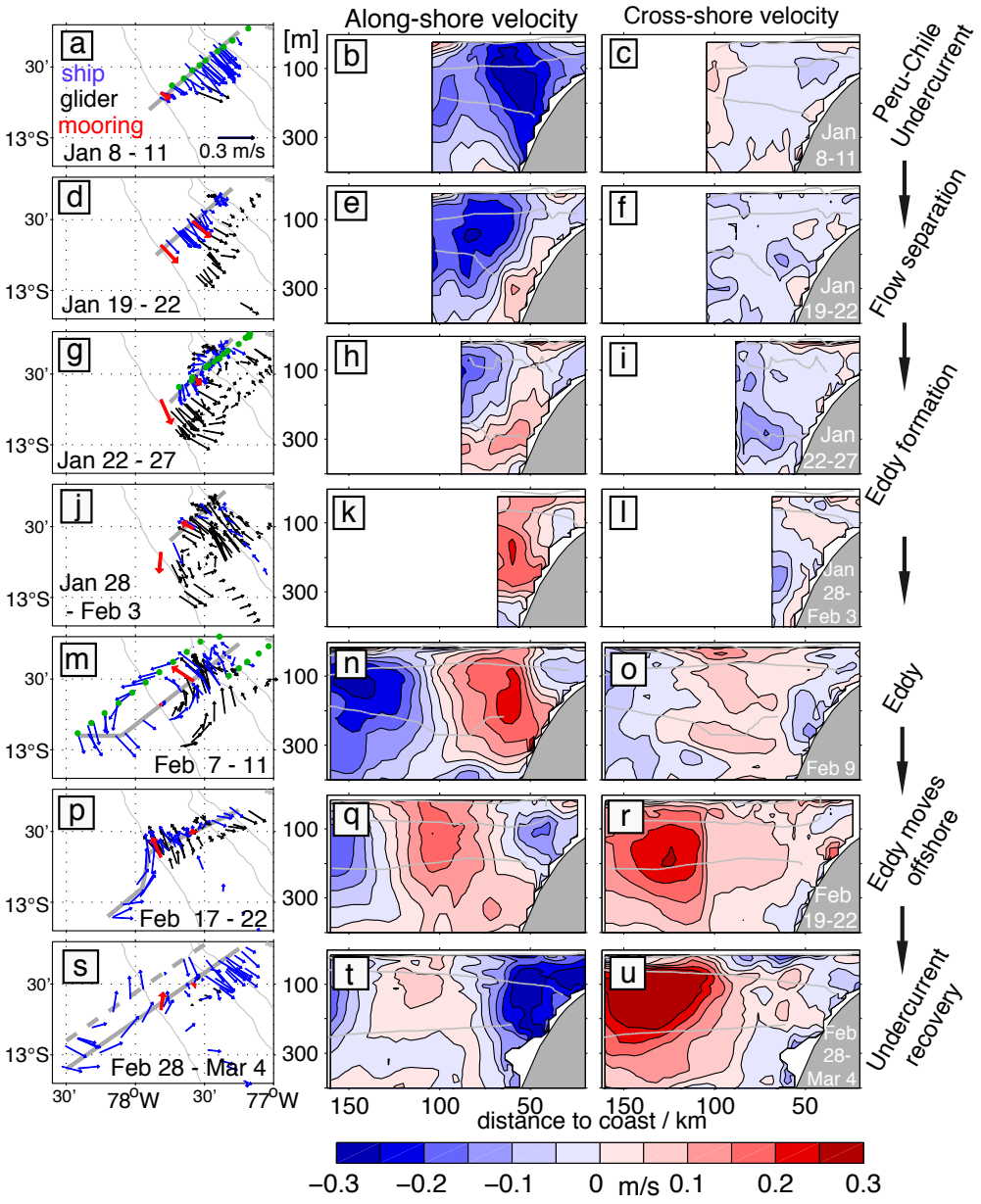

Figure 15: The left column shows the depth-averaged horizontal circulation for eight selected periods based on vmADCP (blue), moored ADCP (red) and glider drift-inferred velocities (black). The 200 m, 400 m and 2000 m isobath is contoured in black. The middle and right column show the temporal evolution of the along- (positive/negative = equatorward/poleward = into/out of the page) and cross-shore (positive/negative = onshore/offshore = to the left/right) velocity components (vmADCP) respectively along the grey transects (left column). Isopycnals (25.6, 26.2 and 26.4) are contoured in grey. The green dots in the left column indicate the position of the nutrient measurements shown in Figure 25.

5.3.2 Eddy formation

The near coastal horizontal circulation off Peru near 12°30'S exhibited pronounced changes in January and February 2013 due to the formation of a subsurface anticyclonic eddy. The chronology of the eddy formation is subsequently described. While a persistent PCUC was observed until January 19, the current core moved offshore during the following week (Fig. 15). Concurrently, an equatorward flow appeared along the upper continental slope between 250 - 350 m depth (Fig. 15e,h,k). Small scale velocity fluctuations and a first eddy-like structure were observed between January 22 - 27 (Fig. 15g). It developed into a coherent eddy centered at around 77°30' W, 12°45'S between January 28 and February 3 (Fig. 15j). A week later, between February 7 and 11, the eddy centre was located directly at the M2 mooring (Fig. 15m), where velocities close to zero were measured during this period. A complete vmADCP-based velocity transect through the eddy was obtained on February 9 (Fig. 15n). Maximum velocities of 0.25 m/s were found between 100 and 200 m depth. The eddy diameter, here defined as the distance between the two velocity maxima, was about 90 km (Fig. 15n). Strong across-shore velocities were found during and after the eddy formation at and offshore of the continental slope (Fig. 15g,j,m). At the southern eddy periphery, onshore velocities advected offshore water towards the continental slope with velocities near 0.25 m/s (Fig. 15r,u). North of the eddy, coastal waters were advected offshore (Fig. 15m). These eddy-induced cross-shore velocities might be crucial, as they potentially provide an important coastal open-ocean exchange mechanism.

On the upper continental slope, poleward velocities of about 0.1 m/s were again observed in mid-February and subsequently increased to values of more than 0.2 m/s by early March (Fig. 15t). This is close to the initial state of the PCUC encountered in early January (Fig. 15b).

In mid-February the eastern eddy edge was still clearly visible at around 78°W (Fig. 15p). The centre had moved to about 12°45' S and 78°10'W, covering a distance of 40 km in 6 days. This translates into a westward drift of about 0.08 m/s. In early March (i.e. at the end of the study period) velocity measurements close to the eddy core where carried out again (Fig. 15s).

Sea surface height anomaly data from satellite observations (AVISO) provided no reliable means to track the eddy path during and after the field campaign. In fact, during the formation of the eddy close to the continental slope, the geostrophic surface velocity field strongly disagreed with our in-situ velocity measurements. This might be explained firstly by known problems of altimetry products close to the coast (*Vignudelli et al.*, 2011)

and and secondly the fact that the rapid changes of the flow field during the formation process could not be captured by the sparse altimetry measurements. However, a clear isolated sea level anomaly signal was also not detectable offshore by the end of the study period. Such a signal is required to track the eddy path by established tracking algorithms (*Okubo*, 1970; *Weiss*, 1991). The subsurface eddy is probably not seen by altimetry because of its small size and its weak or sometimes absent surface velocities. The uppermost vmADCP measurement deviate by up to 0.25 m/s from the subsurface velocity (e.g. Fig. 15n). Furthermore, the eddy with a radius of 45 km is of relative small size when considering the mapping scale of 250 km used by AVISO in the tropics (*Ducet et al.*, 2000). Thus, it is an important finding that energetic subsurface eddies exist off Peru, which are not visible in altimetry products. Nevertheless, we expect that the eddy propagated further westward after our study period as we were able to observe its strong potential vorticity (PV, see below) anomaly in the eddy core right until the end of our observations (Fig. 16t). This indicates that the eddy was still intact at the point.

5.3.3 Potential vorticity and eddy generation mechanism

Subsurface anticyclones similar to the one observed here are often characterized by very low PV and this is thought to play an important role during eddy formation (*McWilliams*, 1985; *D'Asaro*, 1988; *Molemaker et al.*, 2015). Ertel's PV is defined as $PV = \omega_a \cdot \nabla b$, where $\omega_a = (f\mathbf{k} + \nabla \times \mathbf{u})$ is the absolute vorticity with f being the Coriolis parameter, $\mathbf{k}$ the vertical unit vector and $\mathbf{u}$ the velocity vector (*Gill*, 1982). The buoyancy is given by $b = -g\rho/\rho_0$, where g is the gravitational acceleration, ρ the potential density and ρ_0 a reference density. PV is conserved in the absence of tracer and/or momentum mixing and is thus an ideal to identify and track water masses.

We approximate PV by the part associated with the stratification ($N^2 = \partial b/\partial z$) and the vertical component of the absolute vorticity ($\zeta_{abs} = f + \zeta_z$), where $\zeta_z = \partial v/\partial x - \partial u/\partial y$ is the vertical component of the relative vorticity. In cases of weak lateral buoyancy gradients as observed here and below the mixed layer, this is usually a good approximation. Only one component of the vertical relative vorticity ($\partial v/\partial x$) is calculated, as we are only able to compute the spatial derivative of the alongshore velocity from the data. Thus, here we compute $PV \approx N^2(f + \partial v/\partial x)$, where v is the alongshore velocity and x points towards the coast. Given that observed PV structure is largely dominated by distribution of N^2 (Fig. 16, third and fourth column) the omittance of one term in the relative vorticity has a minor effect. Note that f is negative in the southern hemisphere and therefore negative PV

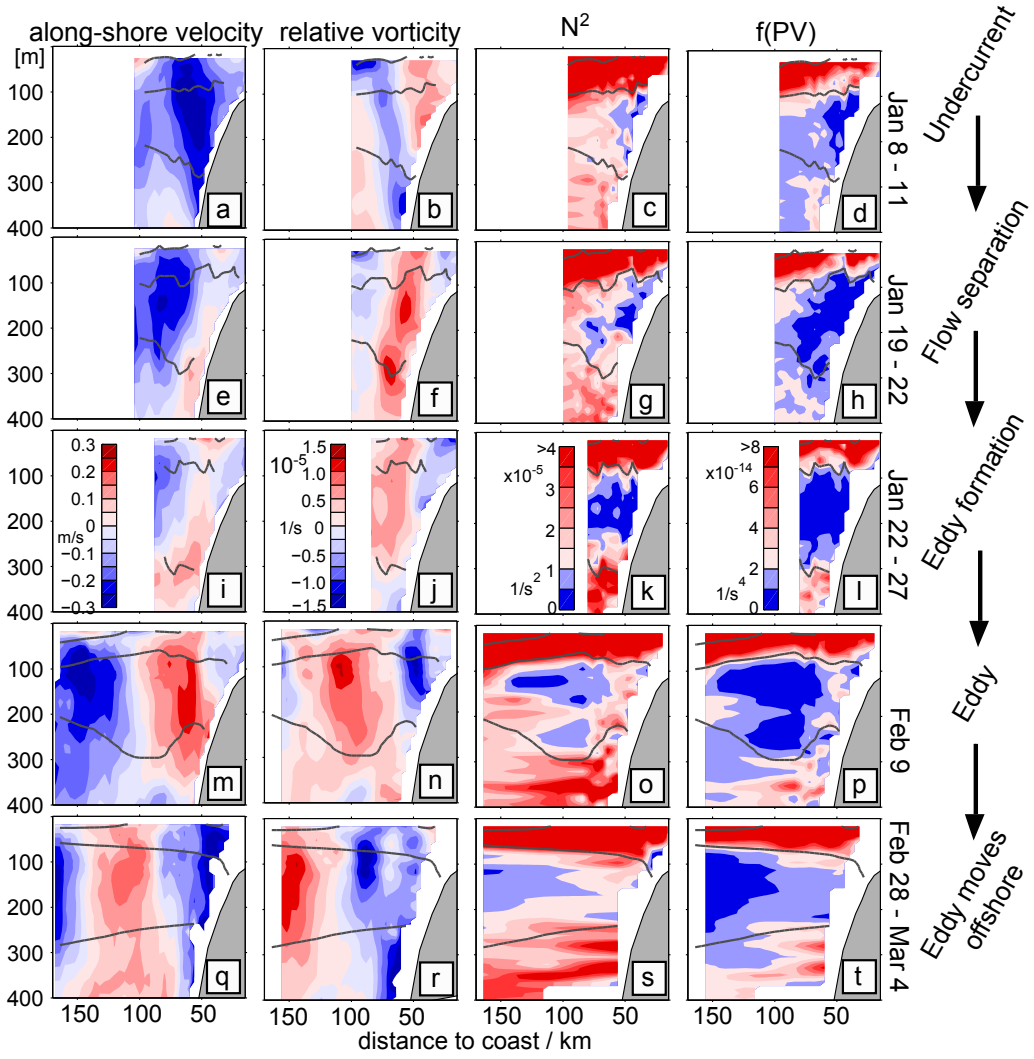

Figure 16: The first column shows the alongshore velocity (vmADPC) in m/s where positive/negative values correspond to equatorward/poleward (into/out of the page) flow. The second column show the two-dimensional relative vertical vorticity ($\zeta^z = \partial v/\partial x$, where v is the alongshore velocity and x points towards the coast). The third column shows the stratification ($N^2 = -(g/\rho_0) \cdot (\partial\rho/\partial z) - (g/c_s)^2$, with g being the gravitational acceleration, ρ the potential density, ρ_0 a reference density and c_s the sound speed). The last column shows the PV times f, with $PV = N^2(f + \partial v/\partial x)$. Isopycnals (25.6, 26.2 and 26.45) are contoured in grey. All transects go along the main transects as marked with grey in the left column of Fig. 15. Only the last transect is slightly further north of the main transect to be closer to the eddy core (dashed grey line in Fig. 15s.)

values reflect stable conditions in respect to symmetric instability (*Hoskins*, 1974; *Thomas et al.*, 2013). Thus we multiply the PV with the local Coriolis parameter f to obtain positive PV values, which allows an easier comparison with northern hemisphere estimates. For simplicity we shall refer to fPV as PV in the following.

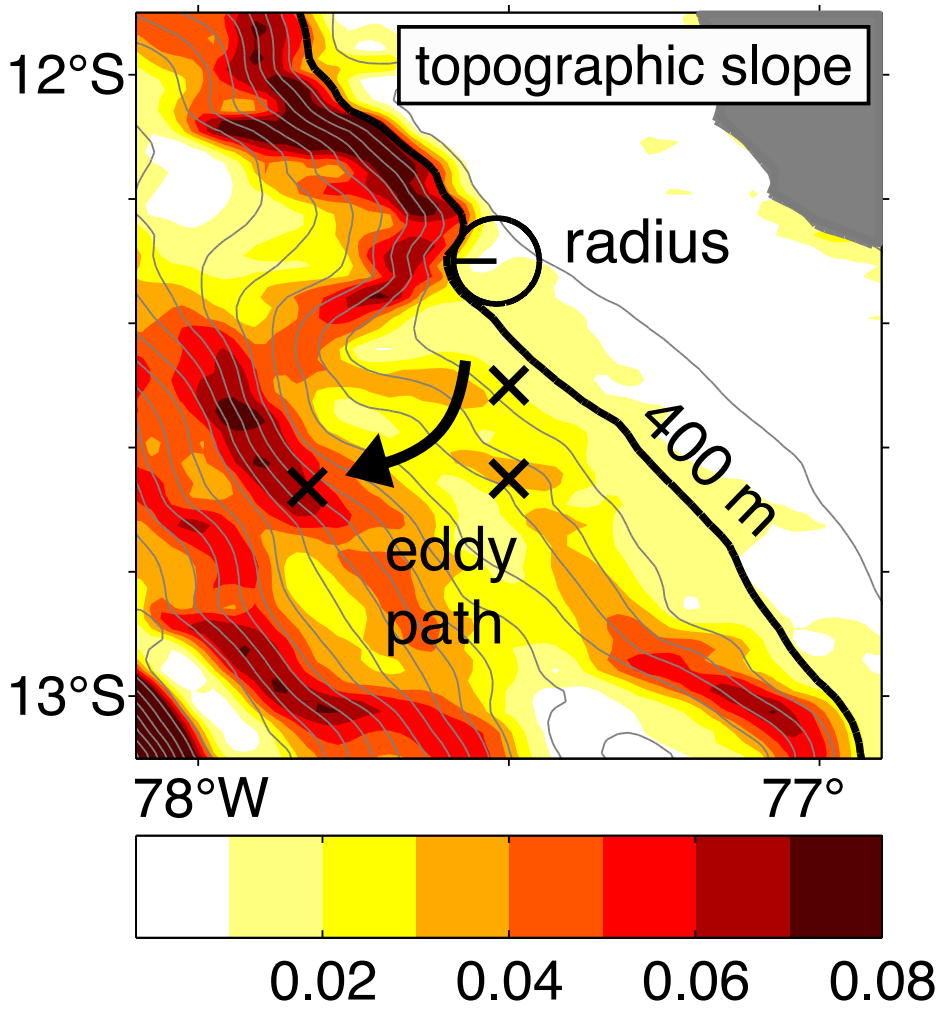

Figure 17: The bottom slope $s = ((\partial H/\partial x)^2 + (\partial H/\partial y)^2)^{1/2}$ (color coded) and water depth (grey contours, 200 m interval) are shown. The radius of the topographic curvature and the 400 m isobath are shown in black. The three black crosses indicate the position of the eddy centre during three different time periods (Jan. 22 - 27, Jan. 28 - Feb. 3 and Feb. 7 - 11).

At the beginning of our observations positive (negative) relative vorticity (Fig. 16b) is found onshore (offshore) of the PCUC core and the stratification is weakest near the bottom at the continental slope (Fig. 16c). The combination of positive relative vorticity and weak stratification results in a band of PV close to zero in the bottom boundary layer at 100 to 250 m depth (Fig. 16d). The negative vorticity band further offshore acts in the opposite direction and increases PV. When the eddy starts to form end of January, both the band of positive relative vorticity and the low stratification move further offshore (Fig. 16f,g). Consequently, the low PV patch increases in size during the ongoing eddy formation. At this point it is no longer restricted to the area close to the topography (Fig. 16l). When the eddy has finally separated from the topography, minimum PV values are found in its core in a depth range between 100 to 300 m (Fig. 16p). These PV values agree well with the observed values close to the bottom on the continental slope prior to the eddy formation. The relative vorticity increases towards the eddy core and maximum values around $1.2 \cdot 10^{-5}$ $1/s$ (0.38f) are found between 100 and 150 m depth. Note that we only compute the component of the relative vorticity associated with $\partial v/\partial x$ and thus the full relative vorticity in the eddy core should be up to factor of 2 larger (around 0.75f) assuming solid body rotation. This is in good agreement with relative vorticity values found in the high-resolution model simulation of *Molemaker et al.* (2015).

About three to four weeks after the first transect through the fully developed eddy (Fig. 16m) another transect was obtained towards the end of the observations (Figs. 15s and 16q). It shows that the low PV within the eddy core has moved offshore as a result of the eddy's westward propagation.

Given that the absolute vertical vorticity is dominated by f, pure adiabatic vortex stretching (e.g. due to unforced flow instabilities) will result in increased cyclonic vorticity. It thus cannot explain the low stratification in the core of the observed eddy, because the relative vorticity there is anticyclonic. Thus the low stratification must have been caused by diapycnal mixing prior to the eddy formation near the surface (*McWilliams*, 1985) or near boundaries (*D'Asaro*, 1988). The latter case is of importance here, as the eddy core waters originate from the equatorial region and moved within the PCUC along the continental slope before they end up in the eddy. As our observations were made in the summer season when atmospheric cooling events do not occur, it cannot explain the reduction of the PV locally. As subsurface eddies tend to be anticyclones the classical baroclinic and barotropic instability mechanisms alone cannot explain their formation, because such eddies have no preferred symmetry (*McWilliams*, 1985; *Molemaker et al.*, 2015). In agreement, off Peru a skewness towards anticyclonic vorticity is found at depth (*Colas et al.*, 2012). A plausible explanation for this might

be the geometry of the PCUC flowing poleward along the continental slope, which results in anticyclonic vorticity between the PCUC core and topography.

D'Asaro (1988) and *Molemaker et al.* (2015) point out the importance of sharp topographic variations for the separation of the low PV boundary water from the topography. This will be investigated in the following. Indeed, we observed the first appearance of an eddy-like structure just downstream of an abrupt change in the curvature of the isopleths (Fig. 15g, Fig. 17). Thus we hypothesize that flow separation is responsible for the eddy formation. This is supported by our observations as will be shown in the following. Firstly, the PCUC core flows along the 400 m isobath (Fig. 15b) which exhibits two sharp bends in the study area (Fig. 17). The second bend is of relevance here as it can force the PCUC to separate. In this region, the offshore displacement of the PCUC is seen in the velocity measurements prior to the eddy formation (Fig. 15d-i). Secondly, the initial disturbances developing into an eddy-like structure (Fig. 15d) are found about 15 km downstream from the topographic bend shown in Figure 17. Black crosses in Figure 17 show the position of the eddy centre directly after its formation. The eddy is clearly formed downstream of the second topographic bend and then propagates westward.

Marshall and Tansley (2001) propose that the separation of a barotropic boundary current at a vertical sidewall takes place when $r < L = (U/\beta)^{1/2}$. Here r represents the radius of curvature of the coastline, which is 7.5 km at the location shown in Figure 17. U is the boundary current speed, here 0.25 m/s and β is the planetary vorticity gradient in the downstream direction ($1.8 \cdot 10^{-11}$ 1/s). This yields a length scale L of about 120 km. As $r << L$ this suggests that flow separation would occur for a case with a vertical sidewall. However, given that the PCUC flows along the topographic slope we propose to use $\beta_{eff} = fs/H$, instead of the usual β, where f is the Coriolis parameter, $s = ((\partial H/\partial x)^2 + (\partial H/\partial y)^2)^{1/2}$ is the bottom slope and H the depth scale of the boundary current, in order to account for the topographic beta effect. Following the early work of *Pedlosky* (1979) on the inertial boundary layer problem, *Kinsella et al.* (1987) used the same formula to investigate the interaction of the Labrador current with the topography of a canyon. With H set to 400 m the topographic beta is around $2.5 \cdot 10^{-9}$ 1/s near this bend and decreases further downstream. This implies that β_{eff} is about two orders of magnitudes larger than β and thus probably more important for the dynamics of the PCUC. Using β_{eff} near the bend instead of β yields $L = 10$ km, which is still larger than the radius of the bend and suggests flow separation. However, given that the separation criteria of *Marshall and Tansley* (2001) does not account for topographic effects,

further research is required to validate our proposed modification.

Given that the swirl velocity and both the relative vorticity and PV anomalies did not lose their strengths, even towards the end of our study period, we suspect that the eddy continued to propagates further westward into the open ocean. The pronounced PV anomaly first would have had to dissipate before the eddy may decay. However, as we are not able to track the eddy via altimetry, we can only speculate about its further propagation and life cycle.

5.3.4 Impact of the horizontal circulation on the distributions of salinity and oxygen

Pronounced variability in salinity and oxygen is observed in the upper ocean along the continental margin off Peru during January and February 2013. The extensive hydrographic dataset allows a detailed description of the evolution of salinity and oxygen characteristics prior, during and after the eddy formation. Three processes are of major importance for the distributions of salinity and oxygen in the study area during the observational period: advection along isopycnals in a vertically sheared flow, mesoscale stirring and eddy-driven ventilation. Each process will be discussed in a separate subsection. A summary schematic is given in Figure 18 to guide the reader through the complex data and should be seen as a hypothesis at this point, which is supported by our observations in the later sections. The schematic is based on both the observed distributions of salinity and oxygen on selected isopycnals (Fig. 19) and the three-dimensional fields (Fig. 20). The analysis focusses mainly on two water bodies characterized by distinct salinity and oxygen concentrations (Figs. 19 and 20). As our first measurements were made in early January, we cannot say much about the history of these water mass patches prior to this period, besides their broad formation area (see section 5.3.1). In the following subsection (5.3.4.1), we describe the formation of isolated oxygen patches in the OMZ. We suggest that they are formed prior to the eddy formation by advection along isopycnals in the upper part of the PCUC that exhibits a pronounced vertical shear of the horizontal flow (Fig. 18a-d). During the eddy formation, the two water bodies are thought to be found south of the study area (Fig. 18e,f). After the eddy formation the near-coastal flow reverses toward northward flow and the water bodies are advected into the study area again (Fig. 18g,h). In subsection 5.3.4.2 we investigate the role of mesoscale stirring for the generation of small scale salinity and oxygen structures by describing the formation of such salinity structures at the eddy edge in detail (Fig. 18g,h). Finally, in subsection 5.3.4.3 we investigate the role of the eddy for the ventilation of the near-

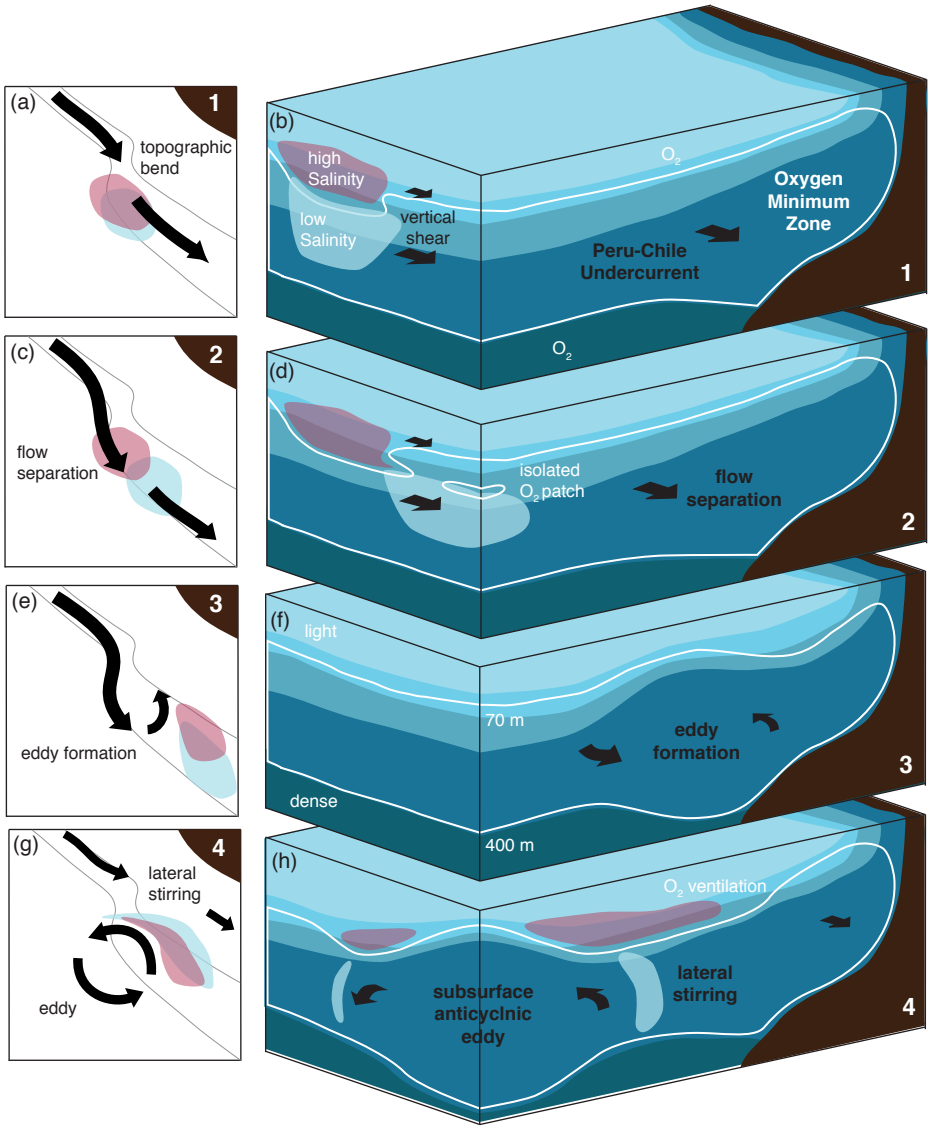

Figure 18: Schematic showing the formation history of the subsurface anticyclonic eddy as horizontal maps (left column) and as three dimensional views (right column). We highlight the impact of the circulation on the salinity and oxygen distributions, including the formation of isolated oxygen patches by advection along isopycnals in a vertically sheared flow (a-d), the formation of low salinity structures at the eddy periphery and the ventilation of the near-coastal oxygen minimum zone both by lateral stirring (g,h). The horizontal circulation is represented with black arrows. Two grey lines in the left column represent topography contours. The high and low salinity water bodies are shown in red and light blue, respectively. The oxycline is represented by the white line and the density stratification is shown by different shades of blue (from dark blue / dense to light blue / light).

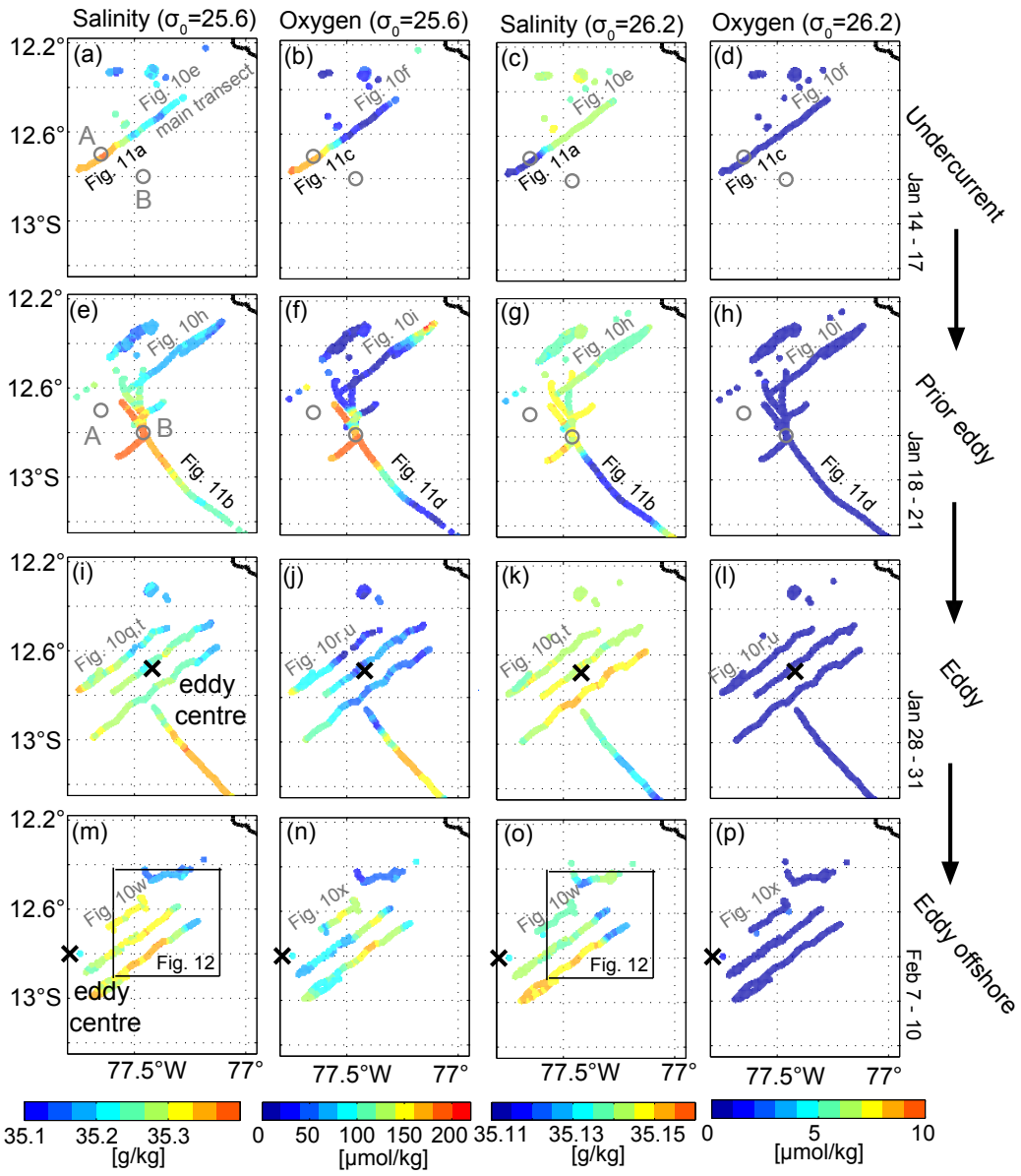

Figure 19: Absolute salinity [g/kg] in the σ_0 range of 25.61 - 25.63 kg/m^3 (1st column) and 26.19 - 26.2 kg/m^3 (3rd column) and corresponding oxygen concentrations [μmol/kg], respectively (2nd and last column) at four different time spans (prior to the eddy formation (upper two rows), just after the eddy formation (3rd row) and about a week after the eddy formation (4th row). All glider and CTD salinity and oxygen data has been gridded prior plotting using a simple gaussian mapping algorithm with a small influence radius of 1 km (1.5 km cut off radius).

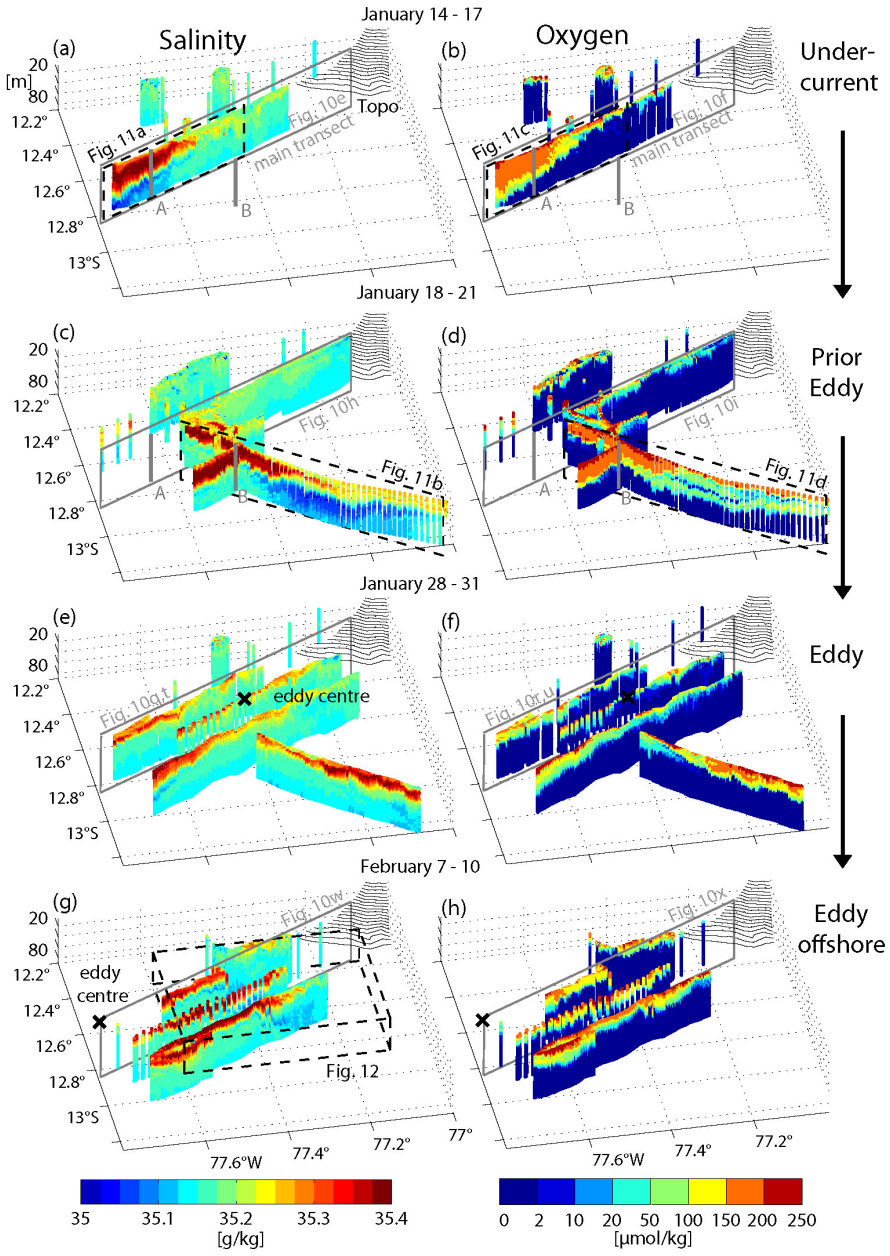

Figure 20: Snapshots of three-dimensional absolute salinity [g/kg] (left panels) and oxygen concentrations [μmol/kg] (right panels) fields around 12°45'S and 77¡ 24'W between 10 m and 90 m at four chosen time spans (prior to the eddy formation: a-d, just after the eddy formation: e,f and about a week after the eddy formation: g,h). The main transect (Figure 21, glider C) is marked by grey boxes. The dashed black boxes mark the transects shown in Figure 22, and the three-dimensional salinity field at the eddy edge (Figure 23). The points A and B (vertical grey lines) are discussed in section 5.3.4.1.

coastal OMZ, which is indicated by a deepening of the oxycline in Fig. 18h.

5.3.4.1 Formation of isolated oxygen patches by advection along isopycnals in a vertically sheared flow prior to the eddy formation

When tracers are advected along isopycnals in a vertically sheared flow, they will separate horizontally due to the different speeds at different depths. Given that along-isopycnal salinity and oxygen gradients are observed in regions of vertically sheared flow, it can be expected that this separation process might contribute to the observed distributions of salinity and oxygen.

The temporal evolution of the along-shore geostrophic velocity and the vertical distributions of salinity and oxygen along the main transect near 12°30'S (glider C) between January 10 and February 27 is shown in Figure 21. During the first three transects prior to the eddy formation, a well-defined PCUC is observed and low-salinity water is present below 50 m and 70 - 100 km offshore (Fig. 21b,e,h). In the thermocline above this low-salinity water, a well-oxygenated water mass with much higher salinities is observed (Fig. 21e,f, Fig. 22a,c). Until around January 22, the horizontal circulation is dominated by the along-shelf flow and both water bodies are transported poleward by the PCUC with a speed of 0.15 - 0.25 m/s (Fig. 15). The low-salinity water is advected southward at higher speeds than the high salinity water, as it is closer to the PCUC core. This can be seen in the along-coast transect of glider G, which sampled the same water bodies during their poleward advection along the coast (Figs. 19a-h, 20c,d and 22b,d).

In contrast to the salinity distribution, the oxygen distribution is more straightforward to interpret. High oxygen levels of up to 250 μmol/kg are restricted to the uppermost layers, while oxygen concentrations below 80 m rarely exceed 1 μmol/kg. However, at depth shallower than 80 m (or at densities smaller than 26.0 kg/m^3) along-isopycnal gradients of oxygen are present in this region (Fig. 14). In the following we focus on the well-oxygenated water body found near the surface between 80 and 100 km offshore on the main transect between January 14 and 18 (Figs. 21f,i and 22c). This water body is of particular interest since it shows strong along-isopycnal oxygen gradients, which are required for eddy-driven along-isopycnal oxygen fluxes (Fig. 22c,d). Note that the vertical oxygen gradient is not perfectly collocated with the vertical salinity gradient. Hence, the upper part of low salinity water still shows comparably high oxygen concentrations, which fall below 2 μmol/kg at densities larger than $\sigma_\theta \approx 26\, kg/m^3$. During the southward advection of these waters isolated oxygen patches are formed in the depth range between 40 to 60 m south of the main transect (Figs. 20d and 22d).

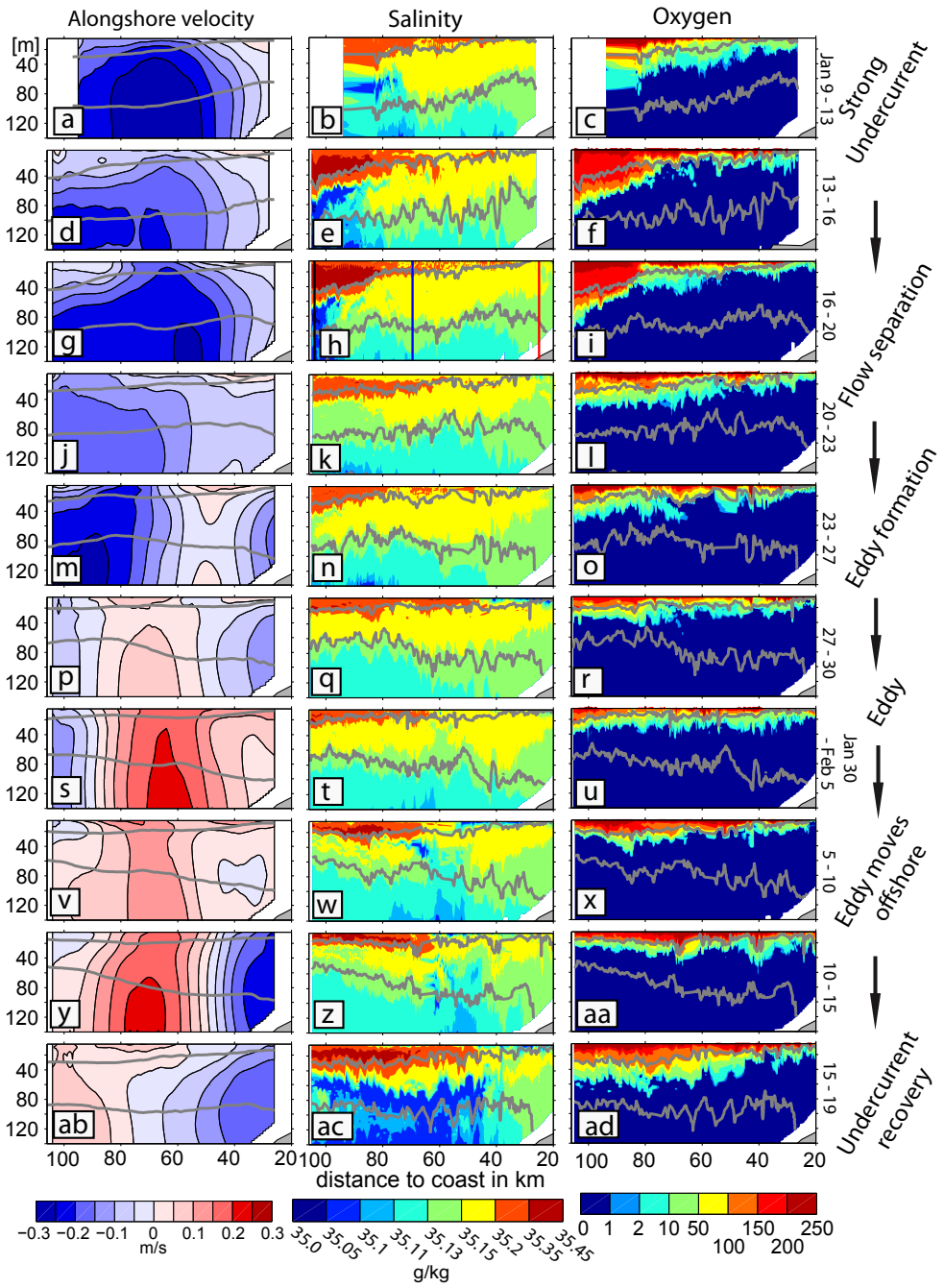

Figure 21: Alongshore geostrophic velocity (positive/negative = equatorward/poleward = into/out of the page) in m/s (left column), vertical distributions of salinity in g/kg (middle column) and oxygen in μmol/kg (right column) along 12°30'S as measured by glider C between January 10 and February 23 2013. The geostrophic velocity is color coded (0.05 m/s interval) and isopycnals (25.6 and 26.2 kg/m^3) are contoured in grey.

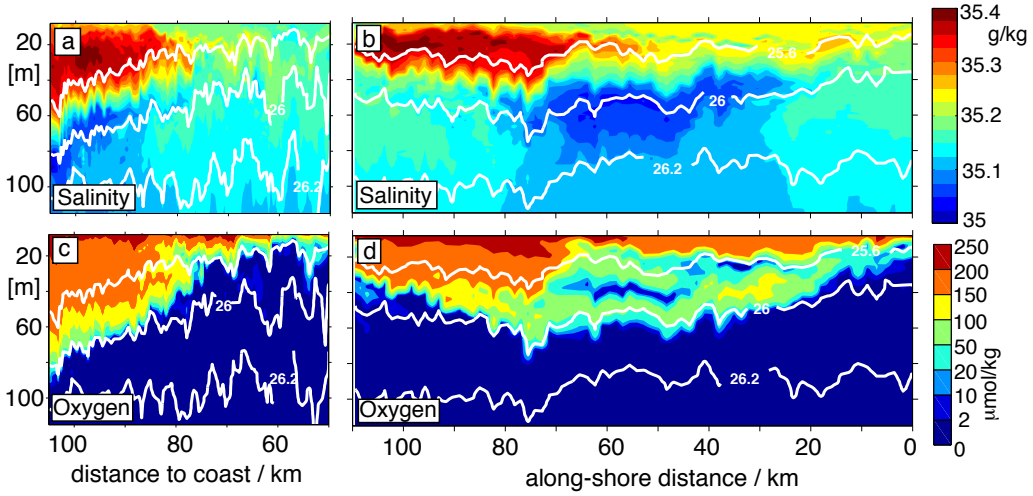

Figure 22: Absolute salinity [g/kg] (upper row) and oxygen concentration [μmol/kg] (lower row) transects observed by glider C between January 13 - 16 (left column) and glider G between January 17 - 22 (right column) within the Peru-Chile Undercurrent prior to the eddy formation. Isopycnals are shown by white lines. Please note the different orientations of the two transects in space (upper = across-shelf, lower = along-shelf), as shown with dashed black rectangulars in Figure 20a-d.

It follows that advection along isopycnals in a vertically sheared flow might explain the separation of the high and low salinity waters and the formation of the isolated oxygen patches described above. This hypothesis is tested using a simple calculation of linear tracer advection along the slope relying on the observed value for the flow speed and the distributions of salinity and oxygen at two depth levels, namely 30 m and 70 m. This simple setup is inspired by the typical PCUC flow structure showing mainly southward currents in the domain up until January 22. Based on our measurements we assume that salinity and oxygen are advected southward along the coast with speeds of 0.15 m/s and 0.25 m/s at a depths of 30 m and 70 m, respectively (Fig. 21). This translates into a horizontal displacement of 30 km at 30 m depth and 50 km at 70 m depth between point A (Fig. 19a-h, 20a-d, 12°42'S and 77°39'W, January 16 06:00) and point B (Fig. 19a-h, Fig. 20a-d, 12°48'S and 77°28'W, January 18 12:00)) over a period of 54 h. This duration corresponds to the time difference between the measurements taken at the two points shown in Figure 20. The distance between the points is ~23 km. Consequently, the saline water mass still is present at point B at around 30 m depth on January 18 12:00 (Fig. 19e, 20c), while larger velocity

at 70 m has allowed the advection of the deeper low salinity water further downstream (Fig. 19g, 20c). Our calculation thus supports the assumption of advection along isopycnals in a vertically sheared flow as an explanation for the observed separation of the high and low salinity water and formation of isolated oxygen patches.

5.3.4.2 Formation of small scale salinity and oxygen structures by mesoscale stirring after the eddy formation Mesoscale stirring of along-isopycnal tracers gradients (e.g. of salinity and oxygen) has to be shown to result in the formation of small scale tracer structures (*Smith and Ferrari*, 2009). Our observations show small scale salinity and oxygen structures in the upper ∼150 m and ∼80 m of the water column, respectively (Fig. 21, middle and right column). As along-isopycnal salinity and oxygen gradients exist in these depth ranges (Fig. 14b,c), we propose mesoscale stirring of along-isopycnal salinity and oxygen gradients as the primarily process generating the structures. In the following we describe the formation of small scale salinity structures at the eddy periphery as an example of mesoscale stirring (Figs. 21w,z and 23).

No distinct salinity and oxygen patches are found along the main transect covered by glider C cutting through the newly formed eddy (Fig. 21t,u). Rather, the eddy core exhibits homogeneous temperature (12 - 14°C), salinity (35 to 35.15 g/kg) and oxygen (< 1 μmol/kg) fields. This is confirmed by the three-dimensional salinity and oxygen fields shown in Figure 20e,f. During the subsequent offshore propagation of the eddy, small-scale salinity features appear at its onshore edge between 50 - 150 m depth at a distance of 60 km from the coast (Fig. 21w). In a two-dimensional (distance to coast vs. depth) view the tilted orientation of the tracer structures at their early stage might suggest that vertical advection could be responsible for their formation (Fig. 21w,z). However, our three-dimensional observations (Figs. 20g and 23) imply that vertical advection is unlikely as a mechanism for the occurrence of the salinity structures. First of all, the structures cross isopycnals (Fig. 21w). This should not be the case as advection moves water parcels predominantly along isopycnals. Secondly, the water properties (potential density, salinity and temperature) in the structures do neither match those at the surface nor those at greater depths. Thirdly isopycnals outcropping at the surface did not show density values as high as those in the structures throughout the entire measurement period.

Instead our observations suggest that lateral stirring by the rotational currents around the eddy periphery is a plausible mechanism for the formation of these structures. Figure 23 shows the formation of the salinity structures at the eddy edge (see black dashed box in Fig. 20g) in more detail. At the

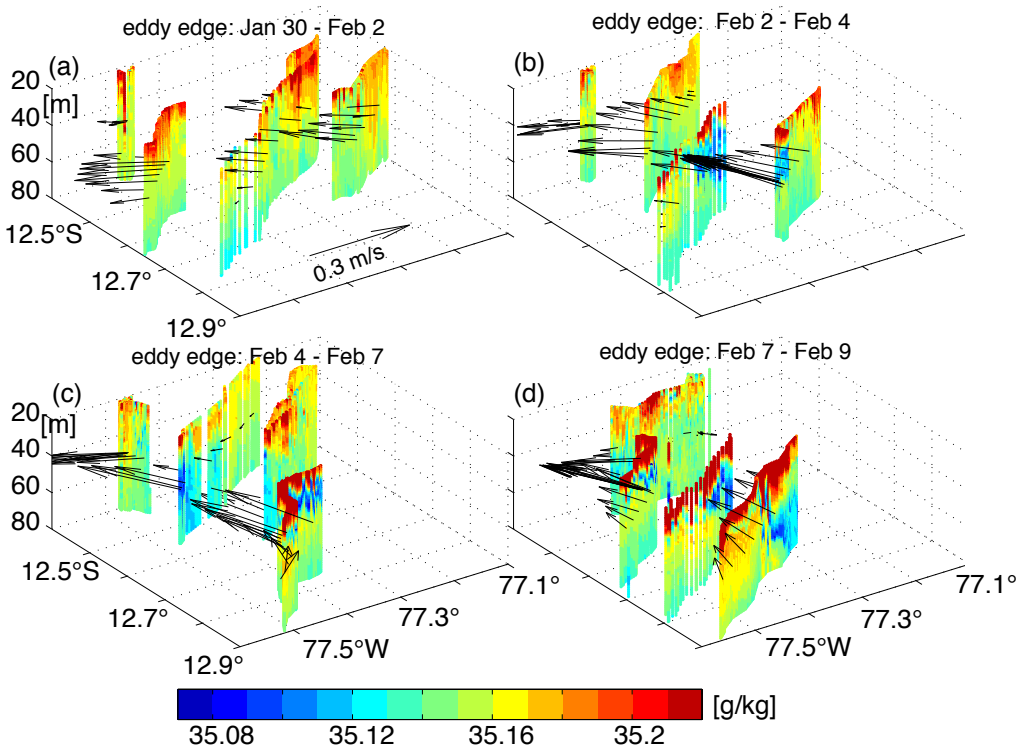

Figure 23: Snapshots of the near-surface (20 - 80 m) absolute salinity [g/kg] at the inshore eddy edge during four different time periods (of 2.5 days length) between January 30, 18:00 and February 9, 18:00. The depth averaged velocity is shown by the black arrows. The location of this box is shown in Figure 20g.

early stage of the newly formed eddy, no salinity structures are found at the eddy edge (Fig. 23a). However, 60 hours later, a low-salinity structure shows up at the two southern transects (Fig. 23b). Several days later, this feature is found along all transects (Fig. 23c,d). The three dimensional observational approach thus clearly indicates that the small scale salinity structures at the eddy edge are formed by lateral advective flow around the eddy periphery. The potential density range and the temperature and salinity characteristics of the waters fit well to those of the low salinity water seen in the first three transects of glider C described above (Fig. 21b,e,h). This further supports that lateral processes are at work.

The fact that low oxygen values and thus also no pronounced oxygen gradients are detectable below 80 m can explain why no small scale oxygen structures are found below 80 m. However, at shallower depths along-isopycnal oxygen gradients are indeed present (Fig. 14c). Consequently, eddy-driven

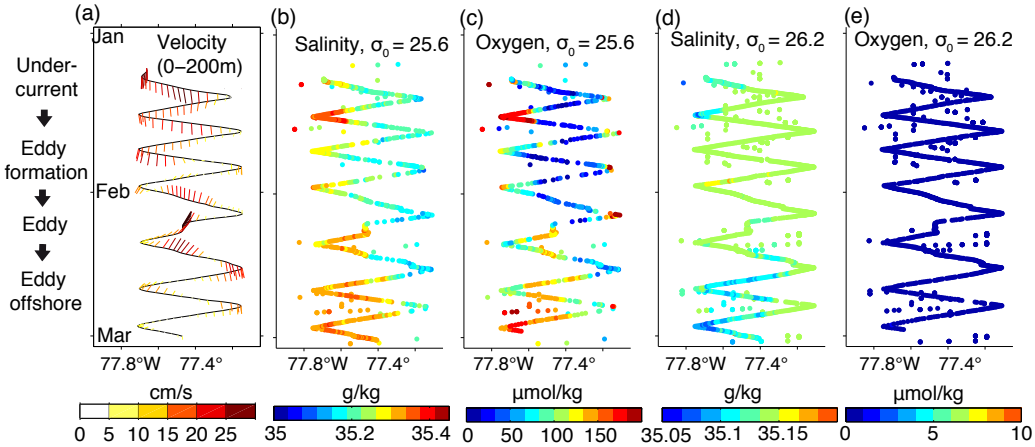

Figure 24: Hovmoeller diagram of the depth averaged (0 - 200 m) horizontal velocity in m/s (a), absolute salinity in g/kg at σ_0 range of 25.61 - 25.63 kg/m^3 (b) and 26.19 - 26.2 kg/m^3 (c) and oxygen concentration in μmol/kg respectively (d), (e) along 12°30'S measured by glider C (doted lines) and the ship based CTD (single dots), which were taken close to the glider transect.

oxygen ventilation of the shallow near-coastal OMZ can be expected.

5.3.4.3 Eddy-driven ventilation of the near-coastal oxygen minimum zone In order to visualize the effects of the mesoscale stirring on the distributions of salinity and oxygen in more detail, we now analyze the temporal evolution of salinity and oxygen on two different isopycnals along the main transect (glider C) near 12°30'S (24b-e). Both density surfaces are also shown in Figure 22 as white contours. The lighter density interface (25.6 kg/m^3) resides in relatively saline and oxygen-enriched water, while the denser density interface (26.2 kg/m^3) represents the oxygen depleted and relatively fresh waters within the OMZ. A close relationship between salinity and oxygen can be seen on the 25.6 kg/m^3 isopycnal, where high salinities go along with elevated oxygen concentrations. However, very close to the coast high oxygen concentrations are found which do not coincide with high salinities. This is due to the outcropping of the isopycnal into the well-oxygenated mixed layer close to the coast.

The temporal change of the depth averaged (0 - 200 m) horizontal velocity along the glider track, that goes along with the eddy formation, can be seen in Figure 24a. By mid-February the velocities reveal an onshore component, which results in the onshore advection of high salinity, well-oxygenated waters on the 25.6 kg/m^3 isopycnal. On this density surface, relatively low oxygen concentrations between 10 to 20 μmol/kg were observed in the center of

the transect during January, while it showed values well-oxygenated (> 100 μmol/kg) after the eddy had formed (Fig. 24b,c). This can also be seen in the transects of the other gliders, which all show elevated oxygen values after the eddy had moved offshore (Fig. 19n).

At greater depths, on the 26.2 kg/m^3 isopycnal, changes in salinity are also observed during the measurement period. After the eddy is formed, a fresher water mass shows up (see discussion section 5.3.4.2). However, more importantly no significant correlation between oxygen and salinity on the 26.2 kg/m^3 isopycnal can be established, as the oxygen concentrations (< 1 μmol/kg) are below the detection limit. Consequently, no pronounced oxygen structures are advected on this density surface.

In summary, the eddy clearly supplied oxygen-enriched waters to the near-coastal OMZ on the 25.6 kg/m^3 isopycnal, which points to the importance of mesoscale stirring for the ventilation of the near-coastal OMZ off Peru.

5.3.5 Impact of the horizontal circulation on the distributions of nitrate, nitrite and nitrogen-deficit

The changing circulation during the eddy formation also impacts the nitrate (NO_3^-), nitrite (NO_3^-) and nitrogen-deficit (N*) distributions (Fig. 25). N* is often used as an indicator for nitrogen sink/source processes in the water column (*Gruber and Sarmiento*, 1997). However, it is important to note that enhanced N* values are not an indicator of active nitrogen-loss processes but represent the accumulated nitrogen-loss of the past. Here we define N* = $(NO_3^- + NO_2^-) - 16PO_4^{3-}$, with ($PO_4^{3-}$) being phosphate, following *Altabet et al.* (2012) and *Stramma et al.* (2013) in order to allow a direct comparison to their findings. We focus on the exchange of NO_3^-, NO_2^- and N* between the continental slope and the open ocean, but not on the upper shelf (< 150 m), where the eddy has less influence on the water mass distribution (section 5.3.2, 5.3.4).

Prior to the eddy formation NO_3^- (NO_2^-) concentrations were mainly above 21 μmol/l (below 4 μmol/l) offshore of the continental slope (Fig. 25d,g). In contrast, NO_3^- (NO_2^-) concentrations below 18 μmol/l (above 7 μmol/l) are observed at the continental slope, especially near the bottom, coinciding with N* values below -17 μmol/l (Fig. 25j). Given that all three parameters show along-isopycnal gradients, eddy-driven cross-shore fluxes can be expected. Note that the NO_3^- and N* concentrations decrease towards the coast along-isopycnals, while NO_2^- concentrations increase. Thus onshore fluxes of NO_3^- and N* (which corresponds to offshore fluxes of nitrogen-deficit waters) and offshore fluxes of NO_2^- are expected.

The eddy formation is associated with across-shore velocities. They cause

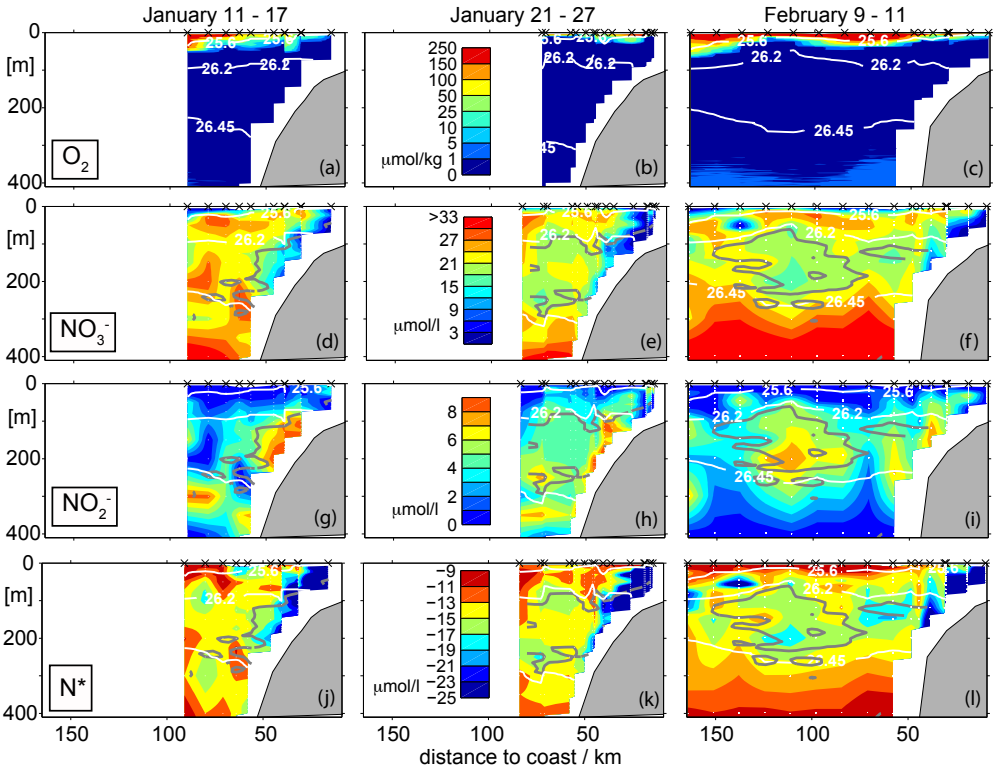

Figure 25: Oxygen in μmol/kg (1st row), nitrate (NO_3^-) in μmol/l (2nd row), nitrite (NO_2^-) in μmol/l (3rd row), nitrogen-deficit ($N^* = (NO_3^- + NO_2^-) - 16PO_4^{3-}$) in μmol/l (4th row) at three different time periods: prior to the eddy formation (left column, January 11 - 17), during the eddy formation (middle column, January 21 - 27) and when the eddy is fully developed (February 9 - 11). The positions of the nutrient measurements are marked with green dots in Figure 15a,g,m. The white dots indicate position of the nutrient measurements. The grey line shows the $fPV = 1.1 \cdot 10^{-14}$ $1/s^4$ contour.

an exchange of waters across the continental slope, leading to a change in the nutrient distribution (Fig. 25, middle column). As a result NO_3^- (NO_2^-) concentrations as low as 15 μmol/l (between 4 - 8 μmol/l) are found offshore between 50 to 300 m depth (Fig. 25e,h). Note that the low PV distribution (indicated by the grey contour in Fig. 25) supports our interpretation that these waters originate from bottom boundary layer along the continental slope (see section 5.3.3).

After the eddy has formed a transect through the eddy was obtained (Fig. 25, right column). We observe NO_3^- concentrations between 15 and 21

μmol/l (Fig. 25f), NO_2^- concentrations of up to 8 μmol/l (Fig. 25i) and a nitrogen-deficit near 17 μmol/l close to the core of the newly formed eddy (Fig. 25l).

In summary, similar to the low PV originating from the bottom boundary at the continental slope, the eddy also advects nitrogen-deficient waters from the region into the open ocean.

5.4 Discussion

To date, only indirect observational evidence for the importance of the PCUC for the generation of subsurface anticyclonic eddies off Peru has been obtained, based both on water mass analyses (*Johnson and McTaggart*, 2010) and the fact that most anticyclones are first detected close to the shelf (*Chaigneau et al.*, 2011). The aim of this study is to provide direct observational evidence that subsurface anticyclones off Peru are indeed formed by instability of the PCUC. The study is based on a multi-platform four-dimensional observational approach. The extensive dataset described here allows a detailed description of the eddy formation process and its impact on the near-coastal salinity, oxygen and nutrient distributions.

The observations suggest that flow separation due to a sharp bend of the continental slope plays an important role for the eddy generation. This implies that the strength of the PCUC is an important parameter, which determines whether a subsurface anticyclone may be generated at this location by flow separation or not. Indeed we observed a relatively strong PCUC ($\sim$0.25 m/s observed core speed, long term mean $\sim$0.15 m/s (*Chaigneau et al.*, 2013)) prior to the eddy formation. Remotely forced coastal trapped waves strongly influence the PCUC (*Chaigneau et al.*, 2013; *Pietri et al.*, 2014) and thus might play an important role in modulating the strength of the subsurface anticyclonic eddy formation process.

A numerical modeling study by *Colas et al.* (2012) indicates that subsurface anticyclonic eddies contribute to the eddy variability off Peru. The authors found anticyclonic vorticity to dominate off Peru with a maximum between 100 to 150 m depth. They relate this finding to subsurface anticyclonic coherent vortices formed by instability of the PCUC. This supports the view that these coherent eddies are important in this region. Clearly, our study is limited to a single eddy formation event. The representativeness of this event for the generation of subsurface anticyclonic eddies in the Peruvian upwelling system thus remains an open question. However, in a recent study *Hormazabal et al.* (2013) investigate the properties and origin of subsurface anticyclonic eddies off central Chile using hydrographic observations, satellite altimetry and a regional eddy resolving ocean model. In

their study observations of two subsurface anticyclonic eddies are presented. Both eddies were first detected close to a sharp coastline variation near 37°S, thus we suggest that flow separation might be responsible for their formation. In general, high mesoscale variability is found off Peru (*Penven et al.*, 2005). We expect that beside flow separation also other instability and forcing mechanisms contribute to the overall eddy field as pointed out by *Liang et al.* (2012) for the northeastern tropical Pacific.

The result that flow separation might be responsible for the formation of subsurface coherent anticyclones in boundary currents is in line with a study by *D'Asaro* (1988) and a recent very high-resolution modeling experiment of the California Undercurrent by *Molemaker et al.* (2015). Both studies investigate the generation mechanism of submesoscale coherent vortices and the boundary currents separate behind sharp topographic bends. *Molemaker et al.* (2015) point out the complexity of the full eddy generation mechanism, which involves not only boundary-current separation but also submesoscale instabilities and upscale flow self-organization. Several aspects of their results agree with the observations presented here: We find unorganized small scale velocity structures prior to the eddy formation; a much more organized coherent structure at a later stage; and a growth of the first coherent eddy structure to a much larger eddy within a few days (Fig. 15j,m). An interesting finding by *Molemaker et al.* (2015) is the importance of the frictional boundary layer for the generation of anticyclonic vorticity and low PV found in the eddy core. This was already suggested by *D'Asaro* (1988). It implies that a large amount of the core water might originate from the bottom boundary layer at the continental slope. In agreement, we observe very low PV in water residing on the topography of the continental slope prior to the eddy formation. Evidence is presented showing that this water ends up in the eddy core during its formation. Thus our observations support the findings of *D'Asaro* (1988) and *Molemaker et al.* (2015) regarding the bottom boundary layer being an important source region of the eddy core water.

The nutrient measurements taken during the formation of the anticyclonic subsurface eddy should give new insights into the role of these eddies for the nitrogen cycling and loss off Peru. In general, the water masses on the continental margin off Peru and Chile are increasingly depleted in biologically available nitrogen during their poleward transport within the PCUC due to nitrogen-cycling processes (*Zamora et al.*, 2012; *Kalvelage et al.*, 2013; *Loescher et al.*, 2014), and near-coastal nutrients measurements off Peru often show reduced NO_3- and N* concentrations in the bottom boundary layer (*Codispoti and Christensen*, 1985; *Hamersley et al.*, 2007; *Lam et al.*, 2009; *Franz et al.*, 2012; *Loescher et al.*, 2014). This is also the case for the nutrient values present in this study (Fig. 25), where enhanced nitrogen-deficits are

observed close to the topography of the continental slope.

In a relatively young eddy close to the shelf near 16°S *Stramma et al.* (2013) observe a nitrogen-deficit anomalies of 35 μmol/l at 50 m and 20 μmol/l in 150 m depth, as well as NO_3^- and NO_2^- core concentrations of <5 μmol/l and ∼10 μmol/l, respectively. They suggest that the high N* and low NO_3^- is due to enhanced nitrogen-loss activity in the eddy. Our observations could be interpreted such that a substantial part of the nitrogen-deficits documented further offshore both close to a mesoscale eddy (*Altabet et al.*, 2012) and inside anticyclonic subsurface eddies (*Stramma et al.*, 2013) might result from nitrogen-loss processes on the upper continental slope and shelf region (*Kalvelage et al.*, 2013), and are subsequently transported towards the open ocean by the eddy.

Whereas measured nitrogen-loss rates reported in shelf waters are high (0.05 - 0.5 μmol/l/day) (*Hamersley et al.*, 2007; *Kalvelage et al.*, 2013) and in combination with benthic nitrogen-loss (*Bohlen et al.*, 2011) can significantly change N* within days to weeks, the nitrogen-loss reported from open ocean is usually well below 0.01 μmol/l/day (*Ward et al.*, 2009; *Canfield et al.*, 2010; *Kalvelage et al.*, 2013)).

In order to distinguish between anomalies that originate at the coast or are induced in the eddy itself, observations of the initial core water mass properties are crucial, but have been missing so far in previous studies. Thus in future studies one should strive to observe the full eddy life cycle including the formation and offshore propagation. In particular the source waters of the eddy core, which are known to change within the PCUC along the coastline (*Zamora et al.*, 2012), should be captured. In a recent study by *Bourbonnais et al.* (2015), the authors sampled one eddy during two occasions one month apart from each other. They find a reduction of NO_3- of about 4 μmol/l in the density range between 26.2 and 26.3 kg/m^3 between the two surveys. However, it remains unexplained how much of the already enhanced nitrogen-deficit of 35 μmol/l during the first survey results from coastal and/or eddy-induced nitrogen-loss processes.

In this study we describe in detail that eddy driven along-isopycnal stirring due to both rotational currents around the eddy periphery and water mass trapping inside the eddy results in an exchange of water masses between the continental slope and the open ocean. The export of nitrogen-deficient water from the continental margin to the open ocean provides a mechanism which might help to explain the observed discrepancies between nitrogen-loss activity and accumulated nitrogen deficit (*Kalvelage et al.*, 2013). Thus mesoscale eddies might be crucial in resupplying NO_3^- to the productive continental margin at depth where nitrogen-loss processes and organic matter export are thought to be highest (*Kalvelage et al.*, 2013).

Our observations show that the horizontal circulation has a large effect on the near-coastal salinity and oxygen distributions and results in the formation of various small scale salinity and oxygen structures. *Pietri et al.* (2013) discuss the formation of small-scale salinity structures in the Peruvian upwelling regime at around 14°S similar to the ones we describe in this study. Our observations confirm their interpretation that lateral stirring of along-isopycnal salinity gradients by mesoscale eddies is mainly responsible for the formation of the fine scale structures. Their additional hypothesis that vertical advective motion driven by submesoscale frontal subduction processes might be responsible for the formation of the salinity structures, can not be confirmed by our study. This hypothesis, however is discussed in recent literature (*Mechoso et al.*, 2014; *Messié and Chavez*, 2014). Here, we want to note that the interpretation of two-dimensional small scale tracer structures by a single glider has to be done with utmost caution, as horizontal processes such as mesoscale stirring can form a wide range of tracer structures. However, our three-dimensional approach might help to interpret small scale salinity and oxygen structures found in future high-resolution two-dimensional observations.

Quantitative eddy-driven oxygen fluxes cannot be estimated from our observations due to the short time period, which only covers one single eddy event. However, the signature of the eddy-driven oxygen ventilation of the near-coastal OMZ is clearly visible in our dataset. *Stramma et al.* (2010) and *Brandt et al.* (2015) came up with rough oxygen budget estimates based on climatological oxygen distributions and an assumed assumed value for the an eddy diffusivity. They suggest that 45 % of total oxygen supply in the eastern tropical South Pacific OMZ is provided by eddy-driven lateral mixing.

5.5 Summary and conclusions

The formation of a subsurface anticyclonic eddy in the Peru-Chile Undercurrent in January and February 2013 is investigated based on four-dimensional multiple-platform observations. The main results are listed below:

1. A strong Peru-Chile Undercurrent with maximum poleward velocities of about 0.25 m/s was observed in early January 2013 off Peru. Isolated oxygen patches are found within the oxygen minimum zones. The differential advection along isopycnals in the vertically sheared upper part of the Peru-Chile Undercurrent is suggested to be their formation mechanism.

2. After January 20, a subsurface anticyclonic eddy was shed by the Peru-

Chile Undercurrent. The eddy core was characterized by potential vorticity close to zero, which seems to have originated from the bottom boundary layer on the continental slope. The eddy formed just downstream of a sharp topographic bend of the 400 m isobath. This suggests flow separation as likely eddy formation mechanism.

3. The eddy-induced circulation strongly modifies the near-coastal salinity and oxygen distributions. Horizontal rotational currents around the eddy periphery (mesoscale stirring) result in the formation of small scale salinity structures at the eddy edge. Across-shelf velocities advect the saline and well-oxygenated Subtropical Surface Water within the thermocline towards the coast. This points to the importance of mesoscale eddies for the ventilation of the upper near-coastal oxygen minimum zone off Peru.

4. The eddy core shows temperature and salinity values characteristic of Equatorial Subsurface Water and oxygen concentrations < 1 μmol/kg. Additionally, an elevated nitrogen-deficit of about 17 μmol/l and enhanced NO_2^- concentrations near 7 μmol/l are found within the eddy just after its formation. They are thought to result from near-shelf nitrogen-loss processes prior the eddy formation.

Our study highlights the impact of the subsurface anticyclonic eddy shed by the Peru-Chile Undercurrent on the tracer distributions in the Peruvian oxygen minimum zone both on a local scale and on larger scales. On the one hand, the eddy stirs local tracer (salinity, oxygen and nutrient) gradients. On the other hand it traps water mass properties (e.g vanishing oxygen, enhanced NO_2- concentrations and nitrogen-deficits) from the upper continental slope and transports them offshore into the open ocean oxygen minimum zone during its westward propagation. As anticyclonic subsurface eddies may exist for several months and travel large distances (*Stramma et al.*, 2014), they can carry water mass properties to very remote places. A large number of studies highlight the general importance of eddies for modulating both biogeochemical productivity and biogeochemical cycles (*Jenkins*, 1988; *Falkowski et al.*, 1991; *Oschlies and Garcon*, 1998; *McGillicuddy et al.*, 1998, 2007; *Lathuilière et al.*, 2010; *Gruber et al.*, 2011; *Gaube et al.*, 2014). However, most global biogeochemical model studies investigating oxygen minimum zones use models which do not resolve mesoscale eddies. Thus their effects have to be parametrized. This might cause uncertainties in forecasting long term oxygen trends (*Stramma et al.*, 2008, 2010) or in the response of oxygen minimum zones to a changing climate (*Stramma et al.*, 2012). More recent high-resolution model studies exist which have suffi-

ciently high resolution to allow eddies to evolve (*Dietze and Loeptien*, 2013; *Montes et al.*, 2014; *Duteil et al.*, 2014). However, these studies focus mostly on the improvements in representing the equatorial current band as a result of enhanced resolution as these currents seem to have a large impact in reducing the bias between simulated and observed nutrient and oxygen distributions. We suggest using these high-resolution simulations to focus on the large-scale effect of mesoscale eddies on oxygen minimum zone dynamics. This is difficult to assess quantitatively even with high-resolution observations. Our high-resolution four-dimensional observational study can help to validate and improve these simulations, since we provide observations of the variability seen in physical and biogeochemical parameters. This study highlights the need for high spatiotemporal resolution observations in eastern boundary upwelling regimes in order to understand the mechanisms driving the observed fast changes in physical and biogeochemical parameters.

6 Do submesoscale processes ventilate the oxygen minimum zone off Peru?

Sören Thomsen, Torsten Kanzow, Francois Colas, Vincent Echevin, Gerd Krahmann, Anja Engel[2]

Abstract

The Peruvian upwelling system shows pronounced submesoscale variability and encompasses the most intense and shallowest oxygen minimum zone (OMZ) in the ocean. We make use of high-resolution glider-based observations carried out off Peru during austral summer 2013 to investigate whether submesoscale frontal processes do ventilate the near-surface Peruvian OMZ. We present observational evidence for the subduction of highly oxygenated surface water in a submesoscale cold filament. The observed subduction event ventilates the upper oxycline but does not reach into OMZ core waters. Lagrangian diagnostics are used to study the pathways of newly upwelled water in a regional submesoscale permitting model. In the model about 50 % of the newly upwelled floats leave the mixed layer within 5 days emphazising a hitherto unrecognized importance of subduction for the ventilation of the Peruvian oxycline.

6.1 Introduction

The Peruvian upwelling region, being one of the four major eastern boundary upwelling systems in the global ocean, is characterized by pronounced meso- and submesoscale variability such as eddies and filaments (*Capet et al.*, 2008b; *McWilliams et al.*, 2009). This variability plays a key role for the offshore and downward export of physical and biogeochemical properties from the productive surface coastal region (*Rossi et al.*, 2008, 2009; *Lathuilière et al.*, 2010; *Gruber et al.*, 2011; *Nagai et al.*, 2015). Submesoscale frontal processes, defined here as operating on horizontal scales of less than the deformation radius, drive large vertical velocities and enhance vertical tracer fluxes in the upper ocean (*Mahadevan and Tandon*, 2006; *Capet et al.*, 2008a; *Thomas et al.*, 2008). The highly productive Peruvian upwelling region encompasses the most intense and shallowest oxygen minimum zone (OMZ) in the ocean (*Karstensen et al.*, 2008) with oxygen concentrations below 1 μmol/l in its core (*Revsbech et al.*, 2009; *Kalvelage et al.*, 2013). The oxycline (i.e. the transition from the oxygenated surface waters to the OMZ) is

[2]This section has been submitted as a manuscript to Geophysical Research Letters.

often very shallow O(30 m) near the coast and strong vertical oxygen gradients are found close to the surface (*Hamersley et al.*, 2007). Due to the vicinity of the well-oxygenated mixed layer and the OMZ waters below, vertical advective motion driven by submesoscale frontal dynamics might be a key process for the vertical supply of oxygen into the OMZ. While a large number of observational and model studies have addressed the role of upwelling filaments for the offshore transport of physical and biogeochemical properties in the Californian (*Flament et al.*, 1985; *Strub et al.*, 1991; *Kadko et al.*, 1991; *Barth et al.*, 2002; *Nagai et al.*, 2015)), Iberian/Canarian (*Barton et al.*, 2004; *Cravo et al.*, 2010), and Benguela upwelling systems (*Lutjeharms et al.*, 1991), the Peru region has received less attention. *Pietri et al.* (2013) use high-resolution (2 km) glider observations to investigate the formation of submesoscale hydrographic structures due to mesoscale stirring. The authors hypothesize that subduction might also be important for the formation of finescale structures. Yet no observational evidence for the subduction of highly oxygenated surface waters off Peru driven by submesoscale processes has been presented. Here we investigate whether submesoscale frontal processes ventilate the Peruvian OMZ. To this end we make use of high-resolution glider-based observations carried out off Peru near 14°S in austral summer 2013 during active upwelling. Additionally, the output of a submesoscale-permitting regional ocean circulation model is analyzed to put the instantaneous short term observations in a broader spatial and temporal context.

6.2 Observational and model data

6.2.1 Glider and satellite observations

The observational part of this study is based on glider high-resolution measurements collected during a multi-platform observational campaign in January and February 2013 off Peru between 12° and 14°S in the framework of the interdisciplinary collaborative research center SFB 754 "Climate - Biogeochemistry Interactions in the Tropical Ocean" funded by the Deutsche Forschungsgemeinschaft. Temperature, salinity, oxygen and fluorescence (chlorophyll) measurements of the upper 70 m at a horizontal and vertical resolution of about 1 km and 1 m respectively are shown along a 100 km transects perpendicular to the coast near 13°30'S (Fig. 26a). The transects capture the signature of an evolving submesoscale cold filament during an upwelling event between January 21 and February 11 2013 (Figs. 26, 27).

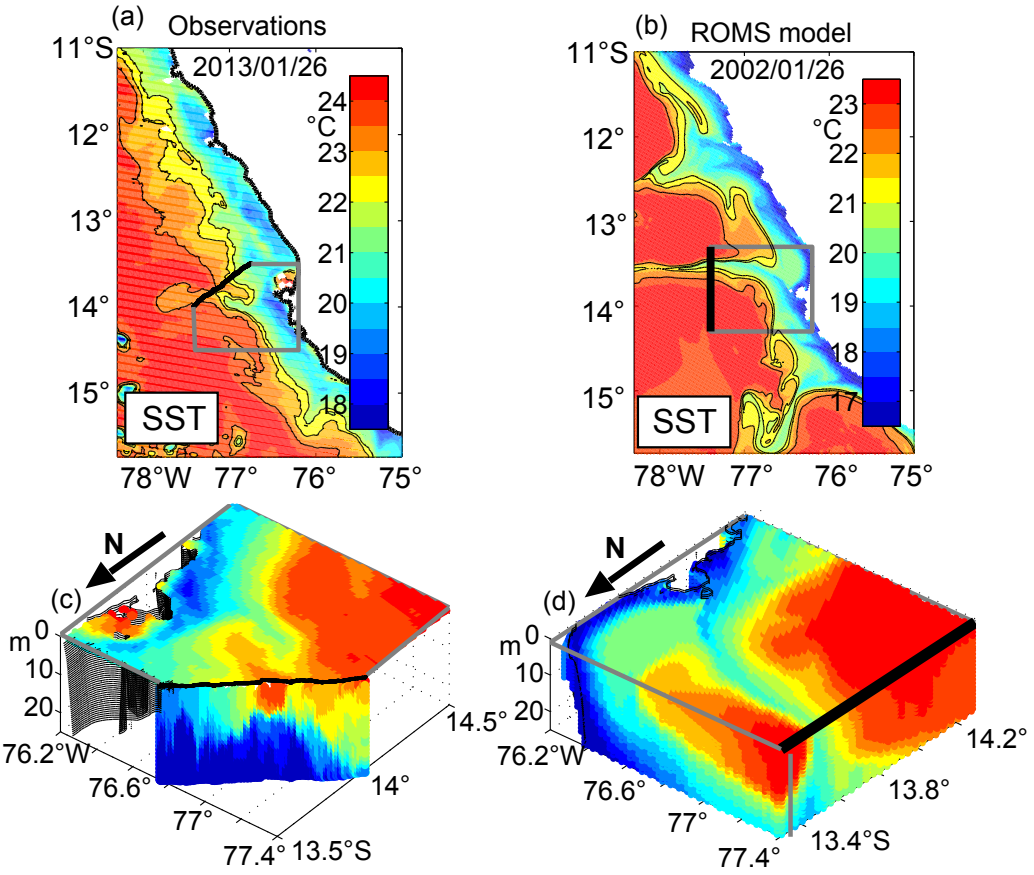

Figure 26: Snapshots of observed (left) and modeled (right) sea surface temperature (SST) and three-dimensional near-surface temperature fields associated with a submesoscale cold filament off Peru. The glider transect is marked by a black line in (a) and (c) and the SST box in grey. Note the different colorbars in (a,c) and (b,d).

The thermal mass of the pumped conductivity cell of the glider was corrected following *Garau et al.* (2011), to improve salinities [Johnson et al., 2007]. A two point lab calibration (0 % and 100 % saturation) of the optodes, which measured dissolved oxygen concentrations, was done on board after the deployment (*Hahn et al.*, 2014). Optodes on gliders exhibit response times between 5 - 175 s (*Bittig et al.*, 2014), which result in a hystereses between up- and downcasts. The response time of the optode was estimated at 23 s by minimizing the difference between oxygen in up- and downcasts. Constant offsets in salinity and dissolved oxygen concentrations were determined by a comparison with nearby ship-based measurements.

Daily sea surface temperature MODIS Aqua / Terra (http://oceandata.sci.

gsfc.nasa.gov) between January and February 2013 were used to put the glider measurements into a regional context.

6.2.2 Regional ocean model

A regional ocean model quasi-equilibrium simulation (ROMS, (*Shchepetkin and McWilliams*, 2005, 2009)) simulation of the Peruvian upwelling region is used to investigate the subduction pathways of newly upwelled water in submesoscale cold filaments. The model domain spans from 16°S to 4.5°S along the coast to about 880 km offshore at a horizontal resolution of 2.2 km and 42 terrain-following vertical levels (sigma coordinates). It is nested offline in a Peru-Chile model with 7.5 km horizontal resolution as in *McWilliams et al.* (2009) and uses boundary conditions from the climatological simulation analysed by *Colas et al.* (2012). The model is forced with the Scatterometer Climatology of Ocean Winds (SCOW) (*Risien and Chelton*, 2008) and the Comprehensive Ocean Atmosphere Data Set (COADS) surface fluxes.

The model shows a realistic near-coastal circulation with a mean poleward Peru-Chile Undercurrent of 0.15 m/s centered at 150 m depth at 15°S (not shown), which compares well with observational estimates (*Chaigneau et al.*, 2013). The model shows pronounced submesoscale variability such as temperature fronts and cold filaments in the sea surface temperature distribution comparable with the observations (Figs. 26, 27 and 28). However, please note that the model shows slightly colder temperatures (~ 1 °C) compared to the observations. In section 6.3.2 the model is further validated by comparing an evolving filament with observations.

To study the circulation of newly upwelled water, virtual floats are seeded in the upper water column of the model and advected offline by the modeled flow using the ROMS offline tool (*Carr et al.*, 2008; *Capet et al.*, 2004). The pathways of Lagrangian floats are computed offline using 4-hour-average velocity fields. We let the floats advect for one day and then only considered floats that entered the mixed layer from below during this day in order to represent newly upwelled water. This procedure explains the spatially inhomogenous distribution of the initial float positions, which are more abundant in areas of strong upwelling (Fig. 28a-c). Then floats were advected forward in time for 20 days. This procedure was repeated ten times (corresponding to ten consecutive starting days) in mid January. Only the last four years of the five-year-long simulation are analyzed to avoid the model spin up period. All together 8000 float trajectories were used for the statistics.

6.3 Results

6.3.1 Observed subduction of surface water in a submesoscale cold filament

The formation and decay of a submesoscale cold filament was captured by satellite and glider based observations off Peru near 14°S (Figs. 26a and 27). The temporal evolution of the sea surface temperature is shown in Figure 2 (upper column). Two distinct water mass features are present in the upper 40 m of the water column in the glider observations. Low salinity (35.05 - 35.24 g/kg) features are found at temperatures between 16.75 - 20°C and high oxygen (> 245 μmol/kg) features are present at slightly higher temperatures (17.5 - 22°C) indicated in black and white contours respectively (Fig. 27 rows 3 and 4). In the following we use these distinct water mass characteristics to learn about the pathways of these features during the formation and decay of the filament.

Both low salinity and high oxygen concentrations are found close to the surface above 10 m depth during the formation of the filament (Fig. 27i,m). High oxygen concentration in surface waters close to the coast result from equilibration with atmosphere and biological production. About 240 μmol/kg oxygen in newly upwelled waters may be explicable by saturation with atmospheric oxygen in coldest waters of about 18°C. However, our observations show oxygen supersaturation (> 100%) pointing to high oxygen production by phytoplankton blooming in the newly upwelled, nutrient-rich waters as indicated by high chlorophyll fluorescence of 20 μg/l (Fig. 27q).

Four days later the filament is fully developed (Fig. 27b) and salinity and oxygen features with similar characteristics are found 90 - 120 km offshore at 10 to 20 m depth (Fig. 27j,n). Finally, after the decay of the filament and the relaxation of the upwelling front the salinity and oxygen features are found within the thermocline 75 - 100 km offshore at around 25 m depth (Fig. 27l,p). Net oxygen production at this depth is likely insignificant as chlorophyll a concentrations are reduced (2 - 4 μg/l, Fig. 27t) compared to 20 μg/l found during active upwelling (Fig. 27q). These observations suggest that the water masses were subducted within the submesoscale cold filament. As the subduction process is three-dimensional, our observations do not necessarily capture the same water masses at each transect but likely waters with similar characteristics that were formed along the coast.

An important finding is that the subduction of the highly oxygenated water mass does not reach into the OMZ core itself, defined here as the zone with oxygen concentrations below 1 μmol/l. In this case the observed subduction only reaches into the oxycline (Fig. 27p).

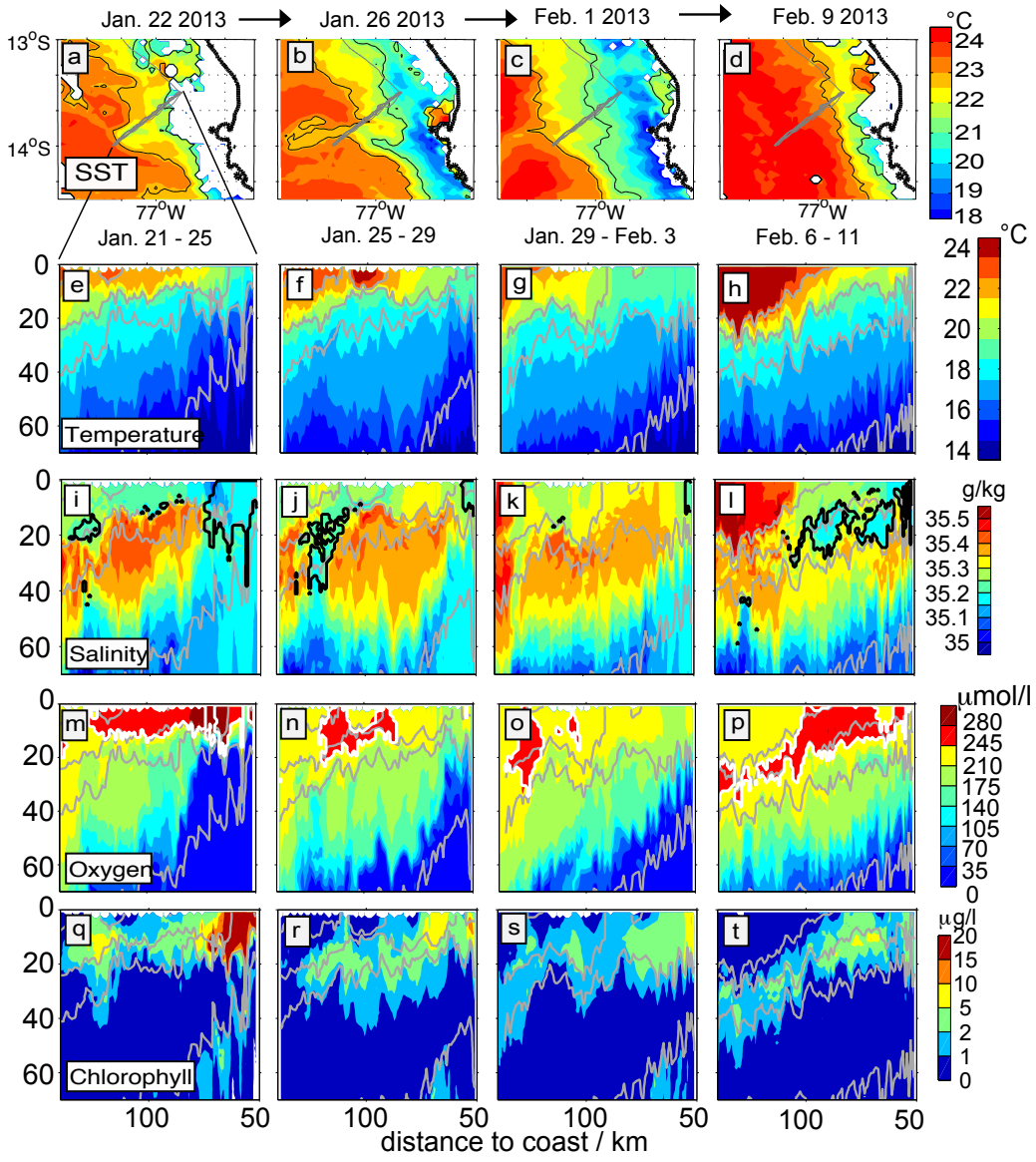

Figure 27: The sea surface temperature associated with the formation and decay of a submesoscale cold filament off Peru in January / February 2013 is shown in the upper panel. Repeated glider transect of the near-surface temperature, salinity, oxygen and chlorophyll (top to bottom) distribution are shown in the panels below. Newly upwelled water of low temperature (16.75 - 20°C) / and low salinity (35.05 - 35.24 g/kg) and medium temperature (17.5 - 22°C) / high oxygen (> 245 μmol/l) are marked by black and white contours, respectively. Isopycnals (24.2, 25, 25.5 and 26 kg/m^3) are shown as grey contours.

6.3.2 Modeled subduction of newly upwelled water

To put our instantaneous short term observations in a broader spatial and temporal context, we now make use of a regional model simulations. The evolution of a simulated filament (Fig. 28), whose horizontal and vertical structure and hydrography compare reasonably well to the observed one (Fig. 27), is described in the following. The chosen filament evolves in mid January to be compareable with our observations. Salinity intrusions of horizontal and vertical scales of about 10 km and 20 m respectively are found in the model (Fig. 28j-l), which compare well to the observed structures (Fig. 27i-l). The modeled salinity intrusions shown here reach down to about 60 m but only to about 40 m in the observations. This might be related to the slightly too broad thermocline in the model but could also be due to the fact that we only compare two snapshots. The simulated vertical velocities are downward within the cold filaments (Fig. 28d-f) as can be expected from filament frontogenesis (*Gula et al.*, 2014; *McWilliams et al.*, 2015). They have locally a magnitude of up to 45 m/day. This supports our interpretation that the observed and modeled tracer structures result from downward motion within the filaments.

The model is able to simulate subduction taking place in filaments with horizontal and vertical scales and hydrography compareable to our high-resolution observations. Thus we will use the model in the following to put the observational results on subduction into broader spatial and temporal context. In particular we want to investigate whether the subduction close to the coast is a regular phenomenon and how it compares to the magnitude of upwelling. Furthermore we want to test whether the observed subduction depth is typical for the summer season.

The initial float positions for a typical Lagrangian experiment are shown in Figure 28a together with the simulated surface temperature field. After the upwelling event the floats follow two different pathways, which are shown with example trajectories of float A and B in Figure 28. Float A remains within the mixed layer and crosses several isopycnals thus reaching lower densities during its offshore movement (Fig. 28). In contrast, float B is subducted mainly along isopycnals and reaches 55 m depth after 10 days of drift (Fig. 28i,l).

A large portion of the floats which move offshore are advected by the cold filaments, as suggested by Figures 28b-c. We now present in Figure 29 a synthetic view of the subducted water mass pathways taking into account all the cold filaments that were present in mid January to mid February in four consecutive model years. The maximum subduction depth of about 65 m (Fig. 29e) is reached within a few days (Fig. 29a). The change of density

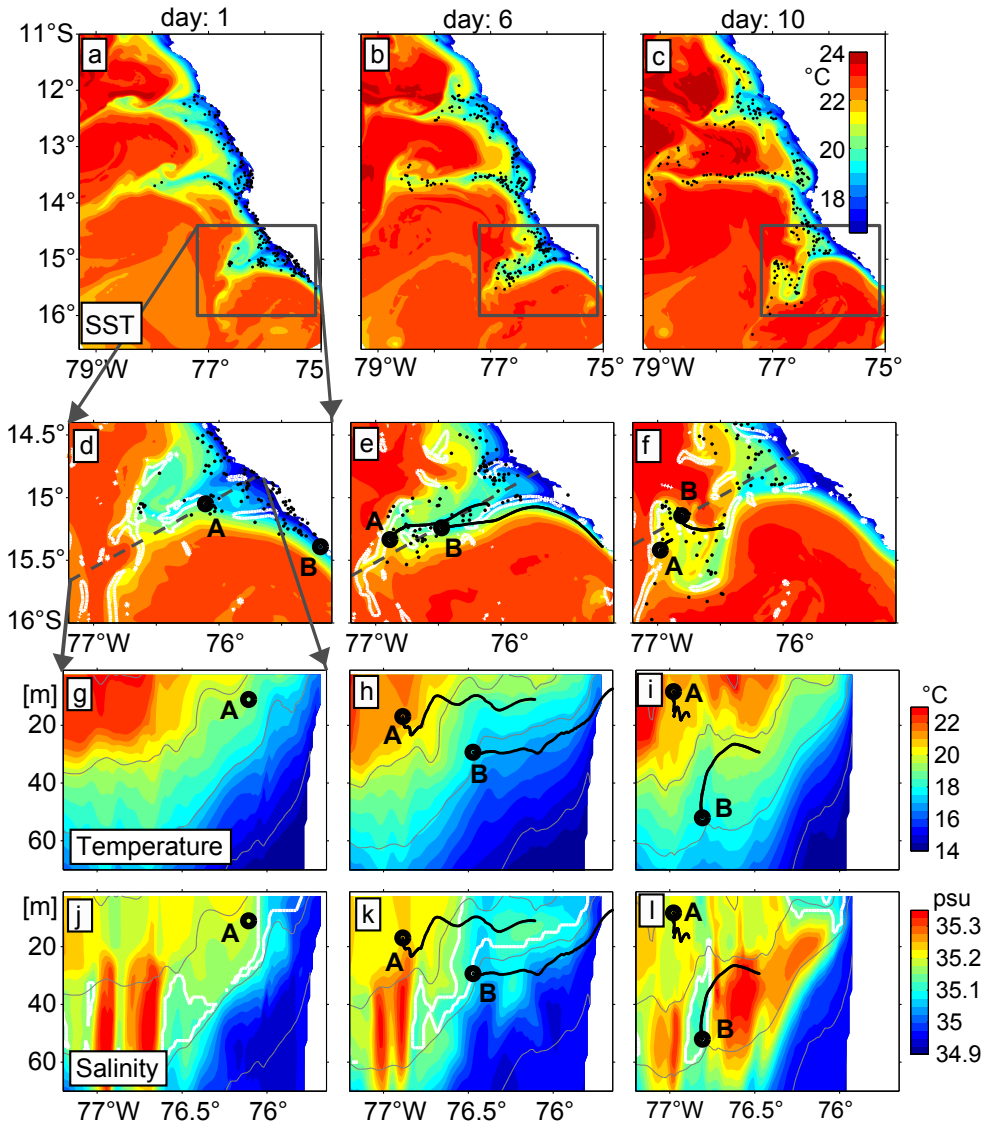

Figure 28: The upper row shows the modeled temperature at 2 m depth along the Peruvian coast at three different times together with the float position; the floats were released at day 0. The second row zooms in into one filament. The white contours indicate downward velocities of w = 6.5 m/day at 15 m depth. The third (fourth) row show the temperature (salinity) distribution of the upper 70 m of the water column during the formation and decay of the filament. The white contours indicate water masses with temperatures between 17.6 - 20 °C and salinities below 35.17 psu. The position of two example floats A (stays in mixed layer) and B (is subducted) are shown by thick black dots. The black tails indicate their pathway since the previously shown position. Note that the filament shown here evolves as the one observed by the glider survey (27) in mid January.

of the floats is strongly associated with their pathway. Floats that stay in the mixed layer while moving offshore tend to cross isopycnals as they get warmer and therefore less dense (Fig. 29c). In summer more than 99.5 % of the floats get less dense during the time they stay in the mixed layer (Figs. 29c,e,g) due to strong surface heating occurring off Peru in summer. In contrast the floats that are subducted tend to keep their density (Fig. 29c). The less time they spend in the warming mixed layer while moving offshore, the deeper they are subducted (Fig. 29e). This points to the importance of the water mass transformation for the pathway of newly upwelled floats. In particular the amount of buoyancy gain (e.g. due to atmospheric warming and lateral mixing with warmer offshore waters) is crucial for the final subduction depth (Fig. 29e).

The simulation-based results may help to interpret the glider-based measurements. The latter demonstrate the absence of highly oxygenated waters below 30 m depth (Fig 27o,p). This can be explained by the fact that it takes several days until the newly upwelled oxygen-depleted water becomes oxygen enriched by both air-sea gas exchange and oxygen production by a phytoplankton bloom (Fig. 27q). At first the newly upwelled, nutrient-rich water experiences a plankton bloom resulting in oxygen production (Fig. 27m). During this time the waters are found close to the surface where they are advected offshore and gradually warm. These results imply that the subduction of newly upwelled water in the summer season, when surface warming is present, cannot reach into the density range of the OMZ. However, the oxycline is indeed ventilated by this rapid subduction process as the newly upwelled water carries a large amount of oxygen once it has either equilibrated to the atmosphere or received oxygen by photosynthesis (Fig. 27p).

In order to see how much of the newly upwelled water is subducted within a few days, we separated the simulated floats into the ones which stay in the mixed layer (e.g. float A) and those which are subducted (e.g. float B) (Fig. 28). The temporal evolution of the mixed layer float inventory is shown in Fig. 29h. The short term oscillations of the inventory result from a diurnal cycle of the mixed layer depth driven by diurnal surface forcing. We varied the starting day of the float release and carried out the same diagnostic in four different years of the model quasi-equilibrium solution to test for robustness. We found that a relatively stable fraction of 50 % of the floats is subducted within about 5 days. This implies that 50 % of the newly upwelled water leaves the mixed layer already within about 5 days and ventilates the oxycline.

6.4 Discussion and conclusion

We have presented observational evidence for the subduction of newly upwelled, well oxygenated surface water within a submesoscale cold filament near 14°S off Peru. A submesoscale permitting numerical model simulation is used to analyse the evolution of newly upwelled water using Lagrangian diagnostics. The simulation of the floats supports our interpretation that the subduction of previously upwelled water can occur within filaments off Peru. Furthermore we find that the final subduction depth depends crucially on the buoyancy change the newly upwelled water experiences in the mixed layer. The floats which are able to escape from the warming mixed layer are subducted to up to 65 m depth in summer. The fact that 50 % of the floats seeded in the newly upwelled water are subducted below the mixed layer five days after being upwelled highlights the importance of this process in ventilating the oxycline off Peru. However, the subduction does not reach into the OMZ itself because the newly upwelled waters gain buoyancy due to surface heating during summer. Therefore they cannot be subducted into the density range of OMZ waters but instead ventilate the upper oxycline.

In the upwelling system off Peru, the thermocline is characterized by a strong decrease in oxygen concentration, primarily due to high heterotrophic microbial activity sustained by the downward flux of organic matter. *Kalvelage et al.* (2015) observed enhanced oxygen consumption rates near the upper boundary of the OMZ. The authors suggest that a 1-dimensional diffusion model might not be able to balance the measured oxygen consumption rates, pointing to the possible importance of advective oxygen supply. The authors further state that even submicromolar oxygen concentrations can be sufficient to maintain aerobic microbial activities and organic matter remineralization rates in the upper OMZ (*Kalvelage et al.*, 2015). On the other hand small amounts of oxygen inhibit nitrogen loss processes such as denitrification and anaerobic ammonium oxidation (*De Brabandere et al.*, 2014). Thus, subduction of oxygen-rich surface waters into the oxycline and possibly associated enhanced diapycnal fluxes of oxygen deeper to the OMZ core may be important to meet the high oxygen demand of aerobic remineralisation processes and to reduce nitrogen losses in the OMZ off Peru.

Given that our model does not fully resolve the submesoscale regime we expect that the vertical exchange intensity is probably underestimated at this resolution (*Capet et al.*, 2008a). Also the effect of high-frequency winds and atmosphere-ocean coupling is not included in the simulations as we use monthly wind forcing. Thus small scale effects are not included e.g. if local winds are aligned with submesoscale fronts Ekman buoyancy fluxes might lead to a deeper subduction depth (*Thomas and Lee*, 2005b). However,

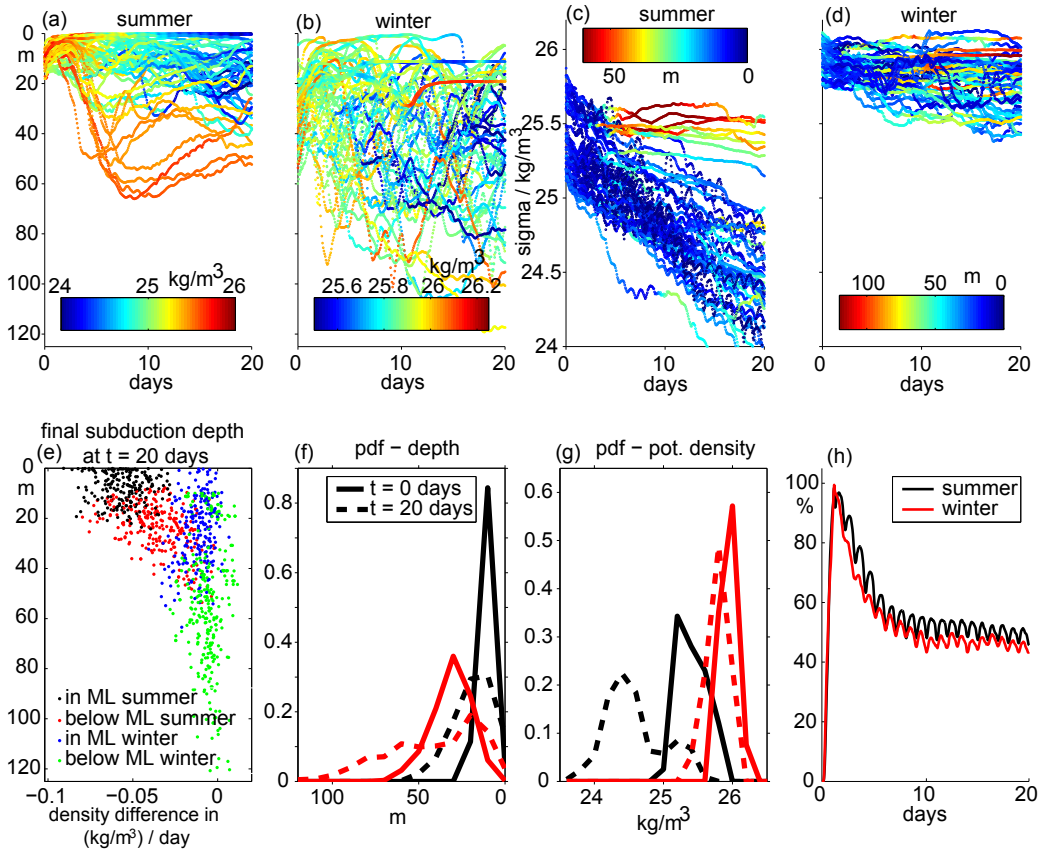

Figure 29: Temporal evolution of 50 example float trajectories in depth space (color coding: density) during summer (a) and winter (b) and density space (color coding: depth) during summer (c) and winter (d). The relationship between the final subduction depth after 20 days and the density difference ($\rho_{day=20}$ - $\rho_{day=1}$) is shown for 500 example floats in e (black (blue) in mixed layer in summer (winter), red (green) below mixed layer in summer (winter). Probability density function of all floats (depth (f) and density (g)) in summer (black) and winter (red) at day 0 and 20. The temporal evolution of the fraction of floats residing within the mixed layer are shown in (g) for summer (black) and winter (red).

given that the winds are relatively steady off Peru, we assume that these effects on the behaviour of the floats are minor.

Several recent studies point out the importance of submesoscale eddy-driven export of surface waters into the ocean interior. *Gula et al.* (2014) carried out a regional high-resolution model study in the Gulf Stream region and highlight the role of submesoscale cold filament dynamics for the subduction of surface waters into the pycnocline. In the subpolar North Atlantic *Omand et al.* (2015) carried out multi-platform observations and a regional high-resolution biogeochemical model study to investigate the export of particulate organic carbon due submesoscale eddy-driven subduction. In both studies much larger subduction depths ($\sim$ 250 - 300 m) than those reported here were reached. In *Gula et al.* (2014) this might be related to the density front of the Gulf Stream which reaches much deeper than that off Peru and thus allows much deeper along-isopycnal pathways. The vertical scale of a front is crucial for vertical penetration of submesoscale eddy fluxes (*Ramachandran et al.*, 2014). Secondly, the water is cooled at the surface in the Gulf stream region, resulting in a density increase and thus greater subduction depths (*Gula et al.*, 2014). This contrasts with the summer situation in our case. However subduction depths might increase during winter.

To further investigate the seasonal variability of subduction, we carried out a float experiment in the winter season from mid June to mid July, when surface cooling is found off Peru. Indeed we find much deeper subduction depths of up to 120 m off Peru in the model (Fig. 29b,f). This can be partly explained by the deeper mixed layer in winter, which goes down to 65 m (Fig. 29e,f) and also by the cooling experienced by the newly upwelled waters (Fig. 29g). While in summer less than 0.5 % of the floats become denser after being upwelled, in winter around 15 % experience a buoyancy loss and most floats mainly keep their initial density (Fig. 29g). The absense of strong warming after the upwelling event in winter thus allows ventilation along-isopycnals to deeper depth compared to summer. We therefore suggest that submesoscale processes may ventilate the upper part of the OMZ during winter. However as high-resolution glider measurements in winter are missing further observations are necessary to test this hypothesis. In particular because a seasonal cycle of the oxygen distribution exists off Peru, which includes variations in the depth and verticle structure of the oxycline (*Czeschel et al.*, 2015).

Filaments and fronts are common features within eastern boundary upwelling systems, all of which encompass large OMZs. However, most state of-the-art large and regional scale physical-biogeochemical ocean models do not resolve submesoscale fronts and filaments and the associated downward transport of oxygen and other tracers. Even if the subduction event observed

off Peru only reaches into the oxygenated part of the thermocline, the associated ventilation mechanism likely influences the shape and depth of the upper boundary of OMZs, which would probably be shallower without this process.

7 Summary and Synthesis

In this section we summarize and synthesize the main findings of sections 4, 5 and 6 and address each of the three questions raised in the introduction of the thesis.

7.1 How is the near-coastal circulation influenced by meso- and submesoscale motion?

The formation of a subsurface anticyclonic mesoscale eddy in the Peru-Chile Undercurrent is investigated in section 5. The lens-like shape of this subsurface eddy is schematically illustrated in Figure 30. As the eddy is formed just downstream of a sharp topographic bend, flow separation is suggested as the eddy formation mechanism. The fact that the eddy core consists of low PV water originating from the bottom boundary layer, supports this finding. In contrast pure vortex stretching associated with unforced flow instabilities would result in cyclonic rather than the observed anti-cyclonic vorticity. This implies that the low PV water must have been formed prior to the eddy formation by diapycnal mixing in the dissipative boundary layer.

The mesoscale eddy influences the cross-shore exchange in two distinct ways. During the formation of the eddy strong cross-shore velocities are observed, which result in an elevated exchange of water masses between the open ocean and the upper continental slope. Furthermore, the eddy captures low PV water from the bottom boundary layer in its core, which is then transported offshore due to the eddy translation. Although the eddy cannot be tracked via satellite altimetry after our observational campaign, it is very likely that these core properties are transported further offshore as reported for other subsurface eddies in the region (*Stramma et al.*, 2013, 2014). As the eddy has a maximum velocity anomaly at around 100 to 150 m depth its strongest impact is in this depth range. However, the eddy also influences the circulation above 100 m depth in the depth range of the upper oxycline of the Peruvian OMZ.

The role of submesoscale processes for the ventilation of the near-coastal OMZ is investigated in section 6. Compared to mesoscale motion associated with the subsurface eddy formation the influence of the submesoscale dy-

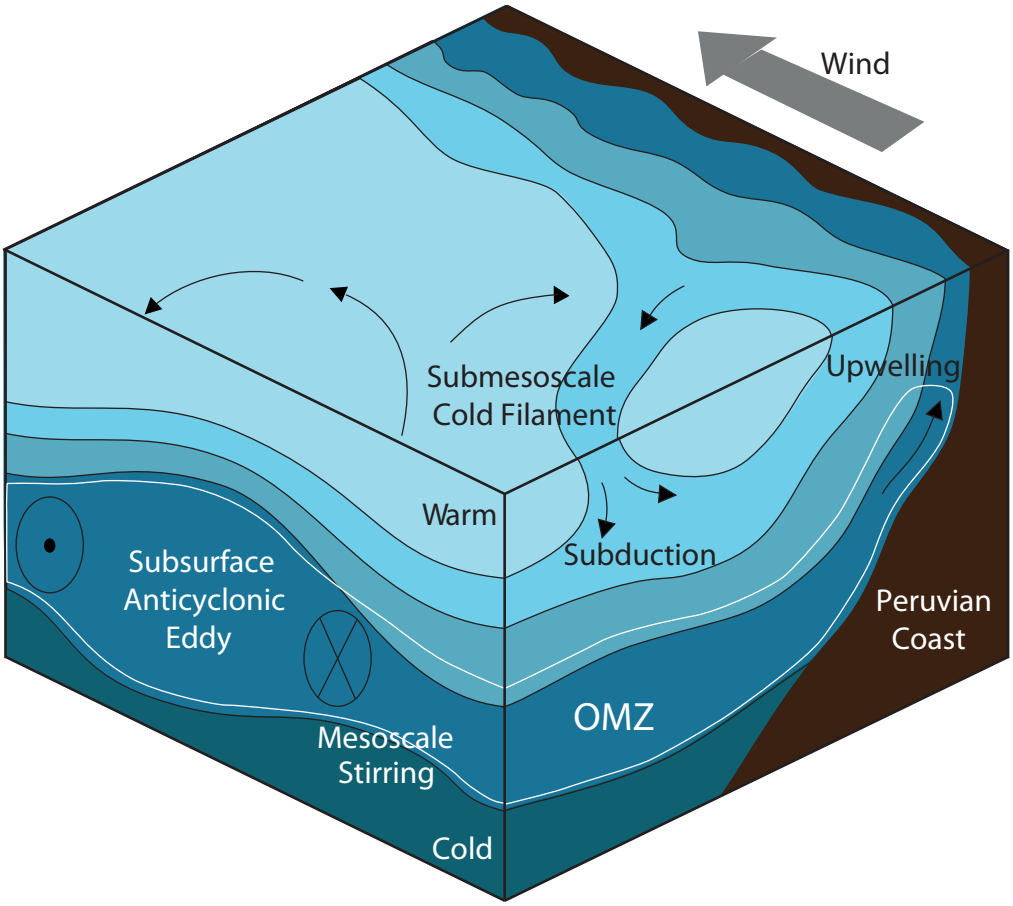

Figure 30: Schematic showing a subsurface anticyclonic mesoscale eddy and a submesoscale cold filament off Peru. The black lines indicate isopycnals. The white lines indicate the boundary of the oxygen minimum zone, which is defined here as oxygen concentrations below 1 μmol/kg. The arrows indicate the direction of the flow field.

namics is restricted to the mixed layer and upper thermocline. Within the newly upwelled water strong biogeochemical processes such as phytoplankton growth and biological oxygen production occur. Thus, the biogeochemical water mass properties are changed rapidly after being upwelled. Also physical water mass properties, such as the density, are changed during the upwelling event due to surface heat fluxes. This will be discussed further below.

We find that submesoscale cold filaments are important for transporting this newly upwelled surface water offshore within a few days. During the offshore movement these waters get subducted in the filaments. This is also

shown in the schematic in Figure 30. Using Lagrangian floats in a numerical model simulation we quantify the importance of this subduction process and compare it with the magnitude of upwelling. In the model, around 50 % of the newly upwelled numerical floats are subducted again within about 5 days. This model result points to the importance of submesoscale subduction for the ventilation of the upper oxycline. The mixed layer depth is shallowest in austral summer (∼15 m) and deepest in winter (∼60 m), which is important for the subduction in submesoscale cold filaments. In the model, a maximum subduction depth of around 60 m is found in summer but the subduction reaches down to 120 m in winter. Beside the mixed layer depth, the surface heat fluxes are also crucial for the maximum subduction depth. In summer the newly upwelled water becomes lighter due to surface warming in the model. Consequently, the density of the newly upwelled water decreases during the offshore transport, and thus it cannot be subducted along isopycnals into the density range of the OMZ. In winter the density of the upwelled water remains constant or even increases due to negative surface heat fluxes, and thus much deeper subduction is found in the model.

It can be summarized that both meso- and submesoscale processes are important for the exchange between the open ocean and coastal waters. Whereas mesoscale dynamics are more important for the circulation at depth below the thermocline, submesoscale motion is more pronounced near the surface in the mixed layer and upper thermocline.

7.2 How do meso- and submesoscale processes impact on the near-coastal tracer distribution?

It is important to know the background tracer distribution to understand the possible influence of meso- and submesoscale motion on the tracer fluxes, which depend on the tracer gradients. Various tracers such as salinity, oxygen and nutrients show complex distributions within the near-coastal region off Peru (*Pietri et al.* (2013), sections 5 and 6). The distributions are strongly influenced by the turbulent motion driven by meso- and submesoscale processes as described in sections 5 and 6.

Mesoscale eddies influence tracer distributions by along-isopycnal stirring. During the induced lateral advection small scale structures of the tracers are formed. In section 5.3.4.2 we describe the formation of small scale salinity structures at the edge of a mesoscale eddy, nicely demonstrating the effect of mesoscale stirring. The rotational currents advect the salinity structures around the eddy periphery, resulting in finescale structures. With our three-dimensional dataset we have been able to describe the mesoscale stirring in detail, which allows us to show that lateral processes are at work rather than

vertical advective motion, as was hypothesized by a previous study on the hydrographic finestructure in the same region off Peru (*Pietri et al.*, 2013).

Another important impact of the eddy formation described in section 5.3.3 is that the low PV boundary layer water, which feeds the eddy core, is transported offshore. This low PV water is also characterized by enhanced NO_2- and large nitrogen-deficits. In section 5.4 it is suggested that the eddy-driven cross-shore transport might be crucial for the nitrogen-budget in the Peruvian OMZ. The nitrogen reduced waters are replenished with nitrogen enriched water from offshore towards the continental slope due to the onshore velocities associated with the eddy. This exchange mechanism between the open ocean and the continental slope might be important to balance the enhanced nitrogen-loss rates close to the coast (*Kalvelage et al.*, 2013).

In section 6 we investigated the role of submesoscale motion for the near-coastal salinity and oxygen distribution. We find that small scale salinity and oxygen structures are transported offshore and subducted along-isopycnals in submesoscale cold filaments. Compared to mesoscale stirring, which in our observations occurs primarily at larger depth below the thermocline, the submesoscale tracer transport takes places in the mixed layer and the upper thermocline.

The tracer distributions likely change during the year. So far, no winter time observations are available, although they are necessary to understand the seasonal cycle off Peru.

7.3 What is the role of meso- and submesoscale processes for the ventilation of the near-coastal OMZ off Peru?

In section 5 the formation of a subsurface anticyclonic eddy in the PCUC and its impact on the oxygen distribution is described. This also includes the role of the eddy in ventilating the near-coastal OMZ off Peru. In section 6 the role of submesoscale frontal processes for the vertical oxygen ventilation is investigated.

The main results of both sections related to oxygen ventilation are summarized in Figure 31. Nutrient-rich water with very low oxygen concentration is upwelled near the coast and enters the mixed layer. Rapid air-sea gas exchange and biological production result in a fast increase of the oxygen concentration. Thus, an oxygen source is present in the upper water column near the coast, which is crucial for the oxygen ventilation as it results in a strong along-isopycnal oxygen gradient with enhanced oxygen concentra-

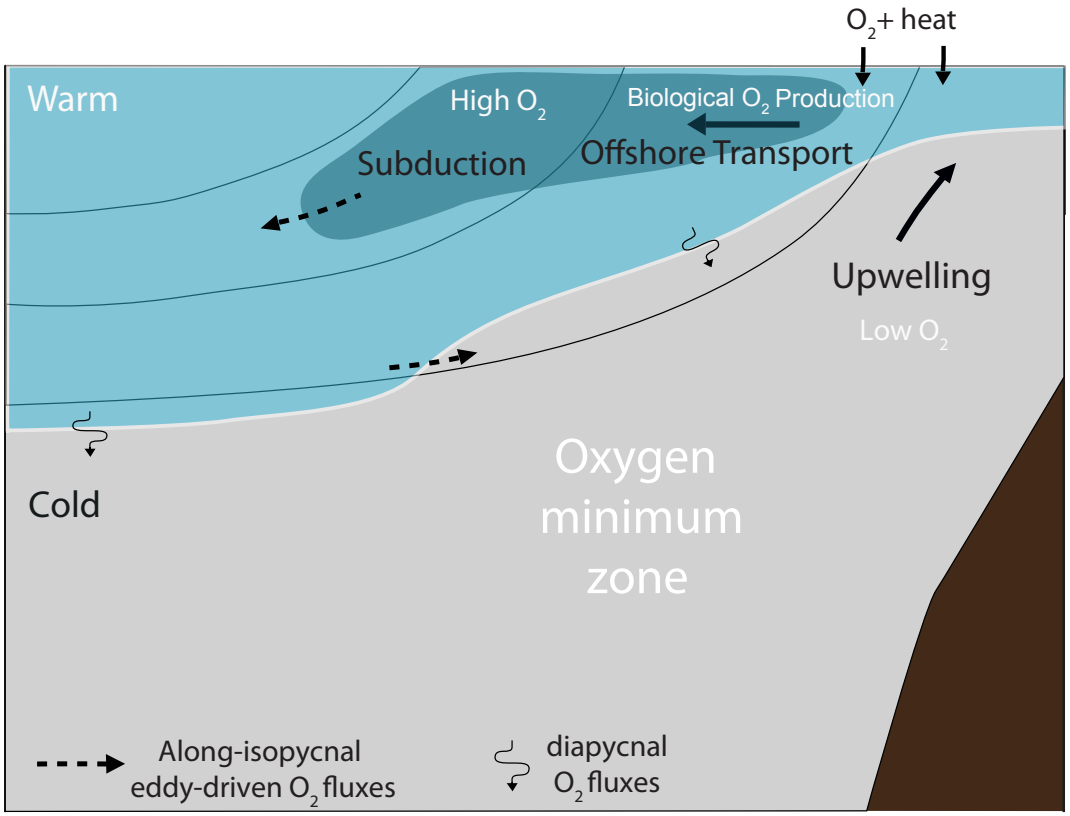

Figure 31: Schematic showing along-isopycnal eddy-driven oxygen fluxes (dashed arrows) due to meso- and submesoscale processes and diapycnal oxygen fluxes (thin curved arrows) during summer off Peru. The surface warming due to atmospheric heat fluxes and the oxygen fluxes due to air-sea gas exchange are shown with small back arrows. The oxygen concentrations above the oxygen minimum zone are marked with two different blue shadings where light blue represents medium and dark blue enhanced oxygen concentrations. The oxygen minimum zone is marked by a grey shading. The surrounding thick white line represents oxygen concentrations of below 1 μmol/l.

tions close to the coast. During its offshore movement the water is gradually warmed in summer due to surface heating. This newly upwelled water moves offshore primarily in cold water filaments and a large fraction is subducted at submesoscale density fronts within a few days. This results in an along-isopycnal ventilation of the upper oxycline. So in principle the water can move along two different pathways namely by either staying in the mixed layer or by being subducted into the thermocline.

One important finding is that the strong warming in the mixed layer during summer leads to a density decrease of the newly upwelled water. Thus it is not possible for the water to re-enter the density range of the OMZ in summer. It can be concluded that submesoscale processes indeed play a role for the ventilation of the upper oxycline. However, the subduction does not reach into the OMZ itself during the summer season in which our observations were carried out. However, in winter the situation is different as no surface warming is present and even surface cooling can be found in some areas off Peru. Thus there is very little change in density of the newly upwelled water during the offshore transport and partly also an increase in density. Therefore the newly upwelled water might be able to enter the density range of the OMZ during the subduction process. It is thus hypothesised that in winter, direct ventilation of the upper OMZ via submesoscale frontal processes might be possible, but so far observational evidence is missing. For more details on proposed future research see also section 9.

At greater depth there is also an along-isopycnal oxygen gradient, however with decreasing oxygen concentrations towards the coast (Fig. 31). Thus time-varying motion such as the formation of a mesoscale eddy (as described in detail in section 5) results in the down-gradient oxygen ventilation of the near-coastal OMZ by offshore waters originating from the edge of the subtropical gyre. Thus the deep OMZ is ventilated laterally by remote water masses. This is illustrated in the schematic of Figure 31 by the dashed arrow which represents eddy-driven oxygen fluxes, pointing towards the coast at depth.

In addition to isopycnal pathways, diapycnal oxygen transport also occurs. This is indicated with the small arrows across isopycnals in the schematic (Fig. 31). The diapycnal oxygen fluxes are not a focus of this thesis. Given that the subduction of the oxygenated water does not reach into the OMZ itself during summer diapycnal transport seem to be crucial for the vertical oxygen fluxes into the OMZ off Peru. Thus the combination of both transport processes can be seen as an effective oxygen pathway consisting of two steps, namely subduction and diapycnal mixing. Therefore it seems possible that enhanced oxygen fluxes due to along-isopycnal subduction also result in enhanced diapycnal oxygen fluxes into the OMZ at greater depth.

It can be summarized that basically two different isopycnal pathways exist. The upper oxycline is ventilated from newly upwelled waters coming from the coast. This ventilation pathway is strongly influenced by submesoscale frontal dynamics, which are predominantly active in the mixed layer and upper thermocline. However, at depth within the OMZ the ventilation along-isopycnals is probably mainly influenced by mesoscale motion. Here, the oxygenated water masses come from further offshore.

8 Conclusion

Multi-platform observations including research vessel, mooring and high-resolution glider-based measurements have been used to investigate the role of meso- and submesoscale processes for the near-coastal circulation and ventilation of the OMZ off Peru. Additionally, the output of a regional model simulation was analyzed to upscale the observational results by studying the pathways of newly upwelled water off Peru.

One important goal of recent research is to understand how the OMZ ventilation off Peru is functioning in present day (*Brandt et al.*, 2015). This knowledge is the basis to understand recent changes in OMZs (*Stramma et al.*, 2008) and to make a prediction of future changes. In this study we focus on the ventilation pathways due to meso- and submesoscale turbulent processes. We find that small-scale processes play an important role for ventilating the OMZ off Peru, providing both horizontal and vertical oxygen transport pathways. Only very recently first physical-biogeochemical models with sufficient resolution to resolve parts of the mesoscale eddy-driven ventilation have been become available (*Dietze and Loeptien*, 2013; *Duteil et al.*, 2014; *Montes et al.*, 2014). However, all of these efforts are based on regional models. The solutions of regional model simulations depend largely on the boundary conditions. These models thus cannot be used to make long-term simulations or climate predictions as long as the boundary conditions are provided by present day climatologies.

Until now, no oxygen budget based on direct oxygen flux measurements has been established for the Peruvian OMZ (*Brandt et al.*, 2015). However, a zeroth order estimate of *Stramma et al.* (2010) and *Brandt et al.* (2015) based on climatological oxygen distributions and an assumed value for the eddy diffusivity suggests that 45 % of total oxygen supply in the eastern tropical South Pacifc OMZ is provided by eddy-driven lateral mixing. However, these studies do not focus on the near-coastal OMZ off Peru where submesoscale eddy-driven and diapycnal fluxes may have a much larger importance for the oxygen supply compared to further offshore.

However, the findings of this thesis can be related to recent studies on the deep OMZ in the eastern tropical North Atlantic, where an oxygen budget based on shipboard, long-term moored and microstructure measurements has been established (*Fischer et al.*, 2013; *Hahn et al.*, 2014; *Brandt et al.*, 2015). The studies show that the oxygen consumption integrated from 350 to 570 m in the deep OMZ of the eastern tropical North Atlantic is balanced by the oxygen supply due to meridional eddy fluxes to about 60% (*Hahn et al.*, 2014) and vertical diapycnal mixing to about 20% (*Fischer et al.*, 2013). The residual supply is mainly attributed to advection by zonal jets (*Brandt*

et al., 2015). The upper boundary of the deep OMZ in the eastern tropical North Atlantic is too deep, compared to the Peruvian OMZ, to be directly influenced by submesoscale dynamics. The density surfaces of the deep OMZ do not outcrop. Thus, no direct local along-isopycnal supply pathways from the surface to the OMZ exist. Consequently our findings on submesoscale dynamics do not impact on the recent oxygen budget estimated for the deep OMZ in the eastern tropical North Atlantic.

Brandt et al. (2015) also investigate the near-coastal shallow OMZ off Mauritania and estimated diapycnal oxygen fluxes of 73 $mmol\ m^{-2}\ d^{-1}$ from the mixed layer into the stratified ocean. However the role of meso- and submesoscale processes for the ventilation has not been investigated so far. Off Mauritania submesoscale processes are observed (*Meunier et al.*, 2012) and subduction of oxygenated water is certainly important as well as the lateral oxygen supply due to mesoscale eddies.

As this study is mainly qualitative and has the aim of increasing process understanding, it should be seen as a first step towards understanding the role of meso- and submesoscale motion for the OMZ ventilation off Peru. So far no, quantitative flux estimates associated with the different processes based on observations have been estimated as have been done for the eastern tropical North Atlantic (*Brandt et al.*, 2015). In the following section a short outlook is given and ideas about possible ways to quantify the oxygen fluxes both in observations and model simulations are proposed.

9 Future work

As shown in this study the combination of high-resolution physical and biogeochemical observations and model simulations is a powerful tool to increase the process understanding on the role of meso- and submesoscale processes in the Peruvian upwelling system. However, from the single event, short term observations presented here, no quantitative meso- and submesoscale eddy-driven oxygen fluxes can be estimated. In this section an outlook of possible strategies to get a more quantitative estimate of the present-day oxygen budget using both observations or models is given. Furthermore a strategy is proposed to use the gained knowledge on the present-day oxygen budget to predict possible future changes in the oxygen minimum zones. The different steps of this strategy are also shown in a schematic in Figure 32.

Building on this thesis, the next step is to understand the role of meso- and submesoscale processes for the near-coastal oxygen ventilation in a more quantitative way. Quantitative estimates of eddy-driven oxygen fluxes both based on observations and models are needed to validate and improve the

model simulations. The strong seasonal cycle in the strength of upwelling and in hydrographic properties off Peru has to be taken into account in the oxygen budget. Therefore high-resolution physical-biogeochemical measurements, which capture all seasons, are suggested. This is necessary because the oxygen distribution for example exhibits a seasonal cycle off Peru (*Czeschel et al.*, 2015) which could imply that oxygen supply pathway due to different processes change their magnitude during the year. If measurements of physical and biogeochemical parameters are available the observed seasonal cycle could be used to further validate the model simulations.

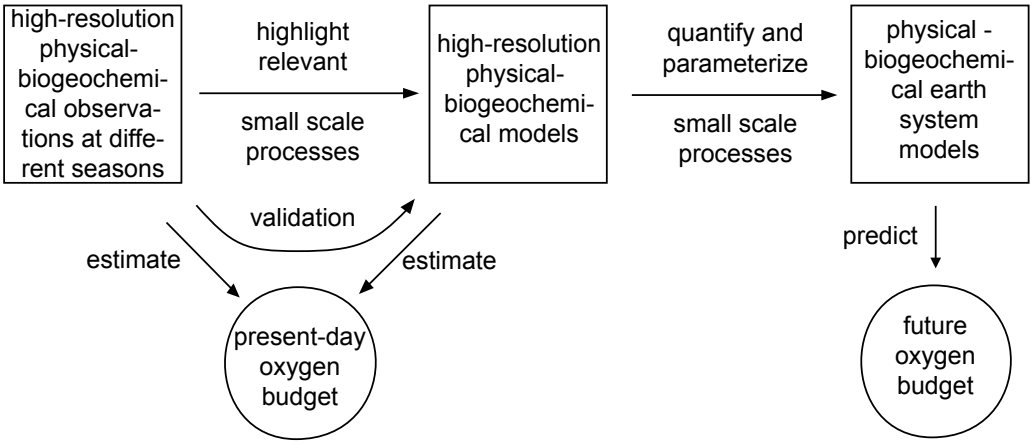

Figure 32: Schematic showing a possible strategy for future research towards the long term goal of predicting changes of the oxygen budget in oxygen minimum zones in the future.

Omand et al. (2015) used glider observations and regional high-resolution biogeochemical model simulations in the North Atlantic to show that up to 50% of the particulate organic carbon export during total spring bloom can be attributed to submesoscale eddy-driven subduction of non-sinking particles from surface water. They used a parametrization of *Fox-Kemper and Ferrari* (2008) to extrapolate to the global scale, using satellite-derived particulate organic carbon concentrations and climatology-based hydrography information. A similar approach using mean density and oxygen gradients from high-resolution observations could be applied to quantify submesoscale eddy-driven oxygen fluxes off Peru. *Brueggemann and Eden* (2015) use linear stability analysis to parameterise eddy-driven fluxes of solutes. The results based on linear stability analyis approach could be compared to the estimates based on the method proposed by *Omand et al.* (2015).

Another more direct observational approach would be to use combined moored velocity and oxygen measurements to estimate the eddy-driven oxy-

gen flux with help of the cross-correlation of both parameters as done by *Hahn et al.* (2014). However, the uncertainty of this approach is relatively large and long time series would be needed. Furthermore this approach does not distinguish between the divergent and rotational eddy fluxes, and the latter do not contribute to the net oxygen supply (*Eden et al.*, 2007; *Hahn et al.*, 2014). Obtaining long-term mooring time series is challenging in the upwelling regime off Peru due to technical issues such as biofouling and the risk of losing equipment due to fishery activities. This approach would exclusively allow the calculation of horizontal eddy fluxes as it is not possible to measure the vertical velocity in the required accuracy of O(mm/s). Even if the direct velocity measurements were accurate enough, the vertical velocity signal would be contaminated by vertical velocities due to internal waves.

Another way to quantify the meso- and submesoscale eddy-driven oxygen fluxes would be to make use of high-resolution biogeochemical model simulations. The model used in sections 4 and 6 is a purely physical model, which does not include oxygen dynamics. However, if a biogeochemical model was coupled to the physical model at the same submesoscale permitting resolution, meso- and submesoscale eddy-driven oxygen fluxes could be quantified. *Nagai et al.* (2015) carried out a high-resolution biogeochemical model study to quantify the offshore and downward fluxes of different biogeochemical tracers in the California upwelling regime. Their study highlights the dominant role of eddies and filaments in driving the overall offshore flux of any matter. A similar regional model study could be carried out off Peru as soon as high-resolution biogeochemical model simulations are available. This should be the case in the next few years due to increased computational power. These simulations might help to parametrize the small-scale fluxes to better implement them in coarse resolution global biogeochemical models. This might help to make more reliable predictions of the future development of oxygen minimum zones.

References

Altabet, M. A., E. Ryabenko, L. Stramma, D. W. R. Wallace, M. Frank, P. Grasse, and G. Lavik (2012), An eddy-stimulated hotspot for fixed nitrogen-loss from the peru oxygen minimum zone, *Biogeosciences*, *9*(12), 4897–4908, doi:10.5194/bg-9-4897-2012.

Badin, G., A. Tandon, and A. Mahadevan (2011), Lateral Mixing in the Pycnocline by Baroclinic Mixed Layer Eddies, *Journal of Physical Oceanography*, *41*, 2080–2101, doi:10.1175/JPO-D-11-05.1.

Barth, J. A., T. J. Cowles, P. M. Kosro, R. K. Shearman, A. Huyer, and R. L. Smith (2002), Injection of carbon from the shelf to offshore beneath the euphotic zone in the california current, *Journal of Geophysical Research: Oceans*, *107*(C6), 10–1–10–8, doi:10.1029/2001JC000956.

Barton, E. D., J. Arístegui, P. Tett, and E. Navarro-Pérez (2004), Variability in the canary islands area of filament-eddy exchanges, *Progress in Oceanography*, *62*(2–4), 71 – 94, doi: http://dx.doi.org/10.1016/j.pocean.2004.07.003, the Canary Islands Coastal Transition Zone - Upwelling, Eddies and Filaments.

Bittig, H. C., B. Fiedler, R. Scholz, G. Krahmann, and A. Körtzinger (2014), Time response of oxygen optodes on profiling platforms and its dependence on flow speed and temperature, *Limnology and Oceanography: Methods*, *12*(8), 617–636, doi:10.4319/lom.2014.12.617.

Boccaletti, G., R. Ferrari, and B. Fox-Kemper (2007), Mixed layer instabilities and restratification, *J. Phys. Oceanogr.*, *37*(9), 2228–2250, doi: 10.1175/JPO3101.1.

Bohlen, L., A. Dale, S. Sommer, T. Mosch, C. Hensen, A. Noffke, F. Scholz, and K. Wallmann (2011), Benthic nitrogen cycling traversing the peruvian oxygen minimum zone, *Geochimica et Cosmochimica Acta*, *75*(20), 6094 – 6111, doi:http://dx.doi.org/10.1016/j.gca.2011.08.010.

Bosse, A., P. Testor, L. Mortier, L. Prieur, V. Taillandier, F. d'Ortenzio, and L. Coppola (2015), Spreading of levantine intermediate waters by submesoscale coherent vortices in the northwestern mediterranean sea as observed with gliders, *Journal of Geophysical Research: Oceans*, pp. n/a–n/a, doi:10.1002/2014JC010263.

Bourbonnais, A., M. A. Altabet, C. N. Charoenpong, J. Larkum, H. Hu, H. W. Bange, and L. Stramma (2015), N-loss isotope effects in the

peru oxygen minimum zone studied using a mesoscale eddy as a natural tracer experiment, *Global Biogeochemical Cycles*, pp. n/a–n/a, doi: 10.1002/2014GB005001.

Bower, A. S., L. Armi, and I. Ambar (1995), Direct evidence of meddy formation off the southwestern coast of portugal, *Deep Sea Research Part I: Oceanographic Research Papers*, *42*(9), 1621 – 1630, doi: http://dx.doi.org/10.1016/0967-0637(95)00045-8.

Bower, A. S., L. Armi, and I. Ambar (1997), Lagrangian observations of meddy formation during a mediterranean undercurrent seeding experiment*, *Journal of Physical Oceanography*, *27*(12), 2545–2575, doi: 10.1175/1520-0485(1997)027¡2545:LOOMFD¿2.0.CO;2.

Brandt, P., H. W. Bange, D. Banyte, M. Dengler, S.-H. Didwischus, T. Fischer, R. J. Greatbatch, J. Hahn, T. Kanzow, J. Karstensen, A. Körtzinger, G. Krahmann, S. Schmidtko, L. Stramma, T. Tanhua, and M. Visbeck (2015), On the role of circulation and mixing in the ventilation of oxygen minimum zones with a focus on the eastern tropical north atlantic, *Biogeosciences*, *12*(2), 489–512, doi:10.5194/bg-12-489-2015.

Brannigan, L. (2015), Intense submesoscale upwelling in anticyclonic eddies, *Geophysical Research Letters (in review)*.

Brink, K., D. Halpern, A. Huyer, and S. R. L. (1983), The physical environment of the peruvian upwelling system, *Progress In Oceanography*, *12*, 285–305.

Brueggemann, N., and C. Eden (2014), Evaluating different parameterizations for mixed layer eddy fluxes induced by baroclinic instability, *J. Phys. Oceanogr.*, *44*(9), 2524–2546, doi:10.1175/JPO-D-13-0235.1.

Brueggemann, N., and C. Eden (2015), Routes to dissipation under different dynamical conditions, *J. Phys. Oceanogr.*, *45*(8), 2149–2168, doi: 10.1175/JPO-D-14-0205.1.

Canfield, D. E., F. J. Stewart, B. Thamdrup, L. De Brabandere, T. Dalsgaard, E. F. Delong, N. P. Revsbech, and O. Ulloa (2010), A cryptic sulfur cycle in oxygen-minimum–zone waters off the chilean coast, *Science*, *330*(6009), 1375–1378, doi:10.1126/science.1196889.

Capet, X., J. C. McWilliams, M. J. Molemaker, and A. F. Shchepetkin (2008a), Mesoscale to submesoscale transition in the california current

system. part ii: Frontal processes, *J. Phys. Oceanogr.*, *38*(1), 44–64, doi:10.1175/2007JPO3672.1.

Capet, X., F. Colas, J. C. Mcwilliams, P. Penven, and P. Marchesiello (2008b), *Eddies in Eastern Boundary Subtropical Upwelling Systems*, pp. 131–147, American Geophysical Union.

Capet, X., J. C. McWilliams, M. J. Molemaker, and A. F. Shchepetkin (2008c), Mesoscale to submesoscale transition in the california current system. part i: Flow structure, eddy flux, and observational tests, *Journal of Physical Oceanography*, *38*(1), 29–43, doi:10.1175/2007JPO3671.1.

Capet, X. J., P. Marchesiello, and J. C. McWilliams (2004), Upwelling response to coastal wind profiles, *Geophysical Research Letters*, *31*(13), n/a–n/a, doi:10.1029/2004GL020123, l13311.

Carr, S. D., X. J. Capet, J. C. McWilliams, J. T. Pennington, and F. Chavez (2008), The influence of diel vertical migration on zooplankton transport and recruitment in an upwelling region: estimates from a coupled behavioral-physical model, *Fisheries Oceanography*, *17*(1), 1–15, doi:10.1111/j.1365-2419.2007.00447.x.

Chaigneau, A., A. Gizolme, and C. Grados (2008), Mesoscale eddies off Peru in altimeter records: Identification algorithms and eddy spatio-temporal patterns, *Progress in Oceanography*, *79*(2-4), 106–119, doi:10.1016/j.pocean.2008.10.013.

Chaigneau, A., M. Le Texier, G. Eldin, C. Grados, and O. Pizarro (2011), Vertical structure of mesoscale eddies in the eastern south pacific ocean: A composite analysis from altimetry and argo profiling floats, *Journal of Geophysical Research: Oceans*, *116*(C11), n/a–n/a, doi:10.1029/2011JC007134.

Chaigneau, A., N. Dominguez, G. Eldin, L. Vasquez, R. Flores, C. Grados, and V. Echevin (2013), Near-coastal circulation in the Northern Humboldt Current System from shipboard ADCP data, *Journal of Geophysical Research: Oceans*, *118*(10), 5251–5266, doi:10.1002/jgrc.20328.

Charney, J. G. (1971), Geostrophic turbulence, *J. Atmos. Sci.*, *28*(6), 1087–1095, doi:10.1175/1520-0469(1971)028¡1087:GT¿2.0.CO;2.

Chavez, F. P., A. Bertrand, R. Guevara-Carrasco, P. Soler, and J. Csirke (2008), The northern Humboldt Current System: Brief history, present

status and a view towards the future, *Progress in Oceanography*, *79*(2-4), 95–105, doi:10.1016/j.pocean.2008.10.012.

Chelton, D. B., R. A. deSzoeke, M. G. Schlax, K. El Naggar, and N. Siwertz (1998), Geographical variability of the first baroclinic rossby radius of deformation, *J. Phys. Oceanogr.*, *28*(3), 433–460, doi:10.1175/1520-0485(1998)028¡0433:GVOTFB¿2.0.CO;2.

Chelton, D. B., M. G. Schlax, R. M. Samelson, and R. A. de Szoeke (2007), Global observations of large oceanic eddies, *Geophysical Research Letters*, *34*(15), n/a–n/a, doi:10.1029/2007GL030812, l15606.

Cline, J., and F. Richards (1972), Oxygen Deficient Conditions and Nitrate Reduction in the Eastern Tropical North Pacific Ocean, *Limnol Ocean. American Society of Limnology and Oceanography*, *17*, 885–900.

Codispoti, L., and J. Christensen (1985), Nitrification, denitrification and nitrous oxide cycling in the eastern tropical South Pacific Ocean., *Mar. Chem.*, *16*, 509–525.

Codispoti, L., and T. Packard (1980), Denitrification rates in the eastern tropical south-pacific., *J Mar Res.*, *38*, 453–477.

Colas, F., J. McWilliams, X. Capet, and J. Kurian (2012), Heat balance and eddies in the peru-chile current system, *Climate Dynamics*, *39*(1-2), 509–529, doi:10.1007/s00382-011-1170-6.

Combes, V., S. Hormazabal, and E. Di Lorenzo (2015), Interannual variability of the subsurface eddy field in the southeast pacific, *Journal of Geophysical Research: Oceans*, pp. n/a–n/a, doi:10.1002/2014JC010265.

Cravo, A., P. Relvas, S. Cardeira, F. Rita, M. Madureira, and R. Sánchez (2010), An upwelling filament off southwest iberia: Effect on the chlorophyll a and nutrient export, *Continental Shelf Research*, *30*(15), 1601 – 1613, doi:http://dx.doi.org/10.1016/j.csr.2010.06.007.

Cromwell, T., and J. L. Reid (1956), A study of oceanic fronts., *Tellus*, *8 (1)*, 94–101.

Czeschel, R., L. Stramma, R. A. Weller, and T. Fischer (2015), Circulation, eddies, oxygen, and nutrient changes in the eastern tropical south pacific ocean, *Ocean Science*, *11*(3), 455–470, doi:10.5194/os-11-455-2015.

D'Asaro, E., C. Lee, L. Rainville, R. Harcourt, and L. Thomas (2011), Enhanced turbulence and energy dissipation at ocean fronts, *Science*, *332*(6027), 318–322, doi:10.1126/science.1201515.

D'Asaro, E. A. (1988), Generation of submesoscale vortices: A new mechanism, *Journal of Geophysical Research: Oceans*, *93*(C6), 6685–6693, doi:10.1029/JC093iC06p06685.

De Brabandere, L., D. E. Canfield, T. Dalsgaard, G. E. Friederich, N. P. Revsbech, O. Ulloa, and B. Thamdrup (2014), Vertical partitioning of nitrogen-loss processes across the oxic-anoxic interface of an oceanic oxygen minimum zone, *Environmental Microbiology*, *16*(10), 3041–3054, doi:10.1111/1462-2920.12255.

Delworth, T. L., A. Rosati, W. Anderson, A. J. Adcroft, V. Balaji, R. Benson, K. Dixon, S. M. Griffies, H.-C. Lee, R. C. Pacanowski, G. A. Vecchi, A. T. Wittenberg, F. Zeng, and R. Zhang (2012), Simulated climate and climate change in the gfdl cm2.5 high-resolution coupled climate model, *J. Climate*, *25*(8), 2755–2781, doi:10.1175/JCLI-D-11-00316.1.

Dietze, H., and U. Loeptien (2013), Revisiting "nutrient trapping" in global coupled biogeochemical ocean circulation models, *Global Biogeochemical Cycles*, *27*(2), 265–284, doi:10.1002/gbc.20029.

Ducet, N., P. Y. Le Traon, and G. Reverdin (2000), Global high-resolution mapping of ocean circulation from topex/poseidon and ers-1 and -2, *Journal of Geophysical Research: Oceans*, *105*(C8), 19,477–19,498, doi:10.1029/2000JC900063.

Duteil, O., F. U. Schwarzkopf, C. W. Böning, and A. Oschlies (2014), Major role of the equatorial current system in setting oxygen levels in the eastern tropical atlantic ocean: A high-resolution model study, *Geophysical Research Letters*, *41*(6), 2033–2040, doi:10.1002/2013GL058888.

Eady, E. T. (1949), Long waves and cyclone waves, *Tellus*, *1*(3), 33–52, doi:10.1111/j.2153-3490.1949.tb01265.x.

Echevin, V., O. Aumont, J. Ledesma, and G. Flores (2008), The seasonal cycle of surface chlorophyll in the peruvian upwelling system: A modelling study, *Progress in Oceanography*, *79*(2–4), 167 – 176, doi:http://dx.doi.org/10.1016/j.pocean.2008.10.026, the Northern Humboldt Current System: Ocean Dynamics, Ecosystem Processes, and Fisheries.

Eden, C., R. J. Greatbatch, and D. Olbers (2007), Interpreting eddy fluxes, *J. Phys. Oceanogr.*, *37*(5), 1282–1296, doi:10.1175/JPO3050.1.

Falkowski, P. G., D. Ziemann, Z. Kolber, and P. K. Bienfang (1991), Role of eddy pumping in enhancing primary production in the ocean, *Nature*, *352*(6330), 55–58.

Ferrari, R. (2011), A frontal challenge for climate models, *Science*, *332*(6027), 316–317, doi:10.1126/science.1203632.

Ferrari, R., and K. L. Polzin (2005), Finescale structure of the t-s relation in the eastern north atlantic, *J. Phys. Oceanogr.*, *35*(8), 1437–1454, doi:10.1175/JPO2763.1.

Ferrari, R., and C. Wunsch (2009), Ocean circulation kinetic energy: Reservoirs, sources, and sinks, *Annual Review of Fluid Mechanics*, *41*(1), 253–282, doi:10.1146/annurev.fluid.40.111406.102139.

Fiedler, P. C., and L. D. Talley (2006), Hydrography of the eastern tropical pacific: A review, *Progress in Oceanography*, *69*(2–4), 143 – 180, doi:http://dx.doi.org/10.1016/j.pocean.2006.03.008, a Review of Eastern Tropical Pacific Oceanography.

Fischer, T., D. Banyte, P. Brandt, M. Dengler, G. Krahmann, T. Tanhua, and M. Visbeck (2013), Diapycnal oxygen supply to the tropical north atlantic oxygen minimum zone, *Biogeosciences*, *10*(7), 5079–5093, doi:10.5194/bg-10-5079-2013.

Flament, P., L. Armi, and L. Washburn (1985), The evolving structure of an upwelling filament, *Journal of Geophysical Research: Oceans*, *90*(C6), 11,765–11,778, doi:10.1029/JC090iC06p11765.

Fonseca, T. R. (1989), An Overview of the Poleward Undercurrent and Upwelling along the Chilean Coast, in *Poleward Flows Along Eastern Ocean Boundaries*, *Coastal and Estuarine Studies*, vol. 34, edited by Neshyba, S.J. and Mooers, Ch.N.K. and Smith, R.L. and Barber, R.T., pp. 203–228, Springer New York.

Fox-Kemper, B., and R. Ferrari (2008), Parameterization of mixed layer eddies. part ii: Prognosis and impact, *J. Phys. Oceanogr.*, *38*(6), 1166–1179, doi:10.1175/2007JPO3788.1.

Fox-Kemper, B., G. Danabasoglu, R. Ferrari, S. Griffies, R. Hallberg, M. Holland, M. Maltrud, S. Peacock, and B. Samuels (2011), Parameterization of mixed layer eddies. iii: Implementation and impact in

global ocean climate simulations, *Ocean Modelling*, *39*(1–2), 61 – 78, doi:http://dx.doi.org/10.1016/j.ocemod.2010.09.002, modelling and Understanding the Ocean Mesoscale and Submesoscale.

Franz, J., G. Krahmann, G. Lavik, P. Grasse, T. Dittmar, and U. Riebesell (2012), Dynamics and stoichiometry of nutrients and phytoplankton in waters influenced by the oxygen minimum zone in the eastern tropical pacific, *Deep Sea Research Part I: Oceanographic Research Papers*, *62*(0), 20 – 31, doi:http://dx.doi.org/10.1016/j.dsr.2011.12.004.

Fuenzalida, R., W. Schneider, J. Garcés-Vargas, L. Bravo, and C. Lange (2009), Vertical and horizontal extension of the oxygen minimum zone in the eastern south pacific ocean, *Deep Sea Research Part II: Topical Studies in Oceanography*, *56*(16), 992–1003, doi: http://dx.doi.org/10.1016/j.dsr2.2008.11.001.

Garau, B., S. Ruiz, W. G. Zhang, A. Pascual, E. Heslop, J. Kerfoot, and J. Tintoré (2011), Thermal lag correction on slocum ctd glider data, *Journal of Atmospheric and Oceanic Technology*, *28*(9), 1065–1071, doi: 10.1175/JTECH-D-10-05030.1.

Garcon, V., A. Oschlies, S. Doney, D. McGillicuddy, and J. Waniek (2001), The role of mesoscale variability on plankton dynamics in the north atlantic, *Deep Sea Research Part II: Topical Studies in Oceanography*, *48*(10), 2199–2226, doi:doi:10.1016/S0967-0645(00)00183-1.

Garrett, C., and W. Munk (1979), Internal waves in the ocean, *Annual Review of Fluid Mechanics*, *11*(1), 339–369, doi: 10.1146/annurev.fl.11.010179.002011.

Gaube, P., D. J. McGillicuddy, D. B. Chelton, M. J. Behrenfeld, and P. G. Strutton (2014), Regional variations in the influence of mesoscale eddies on near-surface chlorophyll, *Journal of Geophysical Research: Oceans*, *119*(12), 8195–8220, doi:10.1002/2014JC010111.

Gill, A. (1982), *Atmosphere-Ocean Dynamics*, International Geophysics, Elsevier Science.

Glover, D. M., S. C. Doney, N. Nelson, and A. Wallis (2008), Mesoscale and Submesoscale Influence on Variability and Anisotropy Observed in Ocean Color Data Near Bermuda, *AGU Fall Meeting Abstracts*, p. A1174.

Grasshoff, K., M. Ehrhardt, and K. Kremling (1983), Methods of seawater analysis 419p, *Eds. Verlag Chemie, Weinheim.*

Gruber, N. (2008), Chapter 1 - the marine nitrogen cycle: Overview and challenges, in *Nitrogen in the Marine Environment (2nd Edition)*, edited by D. G. Capone, D. A. Bronk, M. R. Mulholland, and E. J. Carpenter, 2nd edition ed., pp. 1 – 50, Academic Press, San Diego, doi: http://dx.doi.org/10.1016/B978-0-12-372522-6.00001-3.

Gruber, N., and J. L. Sarmiento (1997), Global patterns of marine nitrogen fixation and denitrification, *Global Biogeochemical Cycles*, *11*(2), 235–266, doi:10.1029/97GB00077.

Gruber, N., Z. Lachkar, H. Frenzel, P. Marchesiello, M. Munnich, J. C. McWilliams, T. Nagai, and G.-K. Plattner (2011), Eddy-induced reduction of biological production in eastern boundary upwelling systems, *Nature Geosci*, *4*(11), 787–792.

Gula, J., M. J. Molemaker, and J. C. McWilliams (2014), Submesoscale cold filaments in the gulf stream, *J. Phys. Oceanogr.*, *44*(10), 2617–2643, doi: 10.1175/JPO-D-14-0029.1.

Gula, J., M. J. Molemaker, and J. C. McWilliams (2015), Topographic vorticity generation, submesoscale instability and vortex street formation in the gulf stream, *Geophysical Research Letters*, *42*(10), 4054–4062, doi: 10.1002/2015GL063731, 2015GL063731.

Gunther, E. R. (1936), A report on oceanographic investigations in the peru coastal current, *Discovery Rep.*, *13*, 107–276.

Gutiérrez, D., E. Enríquez, S. Purca, L. Quipúzcoa, R. Marquina, G. Flores, and M. Graco (2008), Oxygenation episodes on the continental shelf of central peru: Remote forcing and benthic ecosystem response, *Progress in Oceanography*, *79*(2–4), 177–189, doi: http://dx.doi.org/10.1016/j.pocean.2008.10.025.

Hahn, J., P. Brandt, R. J. Greatbatch, G. Krahmann, and A. Körtzinger (2014), Oxygen variance and meridional oxygen supply in the Tropical North East Atlantic oxygen minimum zone, *Climate Dynamics*.

Haine, T. W. N., and J. Marshall (1998), Gravitational, Symmetric, and Baroclinic Instability of the Ocean Mixed Layer, *Journal of Physical Oceanography*, *28*, 634–658, doi:10.1175/1520-0485(1998)028¡0634:GSABIO¿2.0.CO;2.

Hamersley, M. R., G. Lavik, D. Woebken, J. E. Rattray, E. C. Hopmans, and J. S. Sinninghe (2007), Anaerobic ammonium oxidation in the Peruvian

oxygen minimum zone, *Limnology and Oceanography*, *52*(3), 923–933, doi: 10.4319/lo.2007.52.3.0923.

Holland, W. R., and L. B. Lin (1975a), On the generation of mesoscale eddies and their contribution to the oceanicgeneral circulation. i. a preliminary numerical experiment, *J. Phys. Oceanogr.*, *5*(4), 642–657, doi: 10.1175/1520-0485(1975)005¡0642:OTGOME¿2.0.CO;2.

Holland, W. R., and L. B. Lin (1975b), On the generation of mesoscale eddies and their contribution to the oceanicgeneral circulation. ii. a parameter study, *J. Phys. Oceanogr.*, *5*(4), 658–669, doi:10.1175/1520-0485(1975)005¡0658:OTGOME¿2.0.CO;2.

Holte, J., F. Straneo, C. Moffat, R. Weller, and J. T. Farrar (2013), Structure and surface properties of eddies in the southeast Pacific Ocean, *Journal of Geophysical Research: Oceans*, *118*(5), 2295–2309, doi:10.1002/jgrc.20175.

Hormazabal, S., V. Combes, C. E. Morales, M. A. Correa-Ramirez, E. Di Lorenzo, and S. Nuñez (2013), Intrathermocline eddies in the coastal transition zone off central chile (31–41 °s), *Journal of Geophysical Research: Oceans*, *118*(10), 4811–4821, doi:10.1002/jgrc.20337.

Hosegood, P., M. C. Gregg, and M. H. Alford (2006), Sub-mesoscale lateral density structure in the oceanic surface mixed layer, *Geophysical Research Letters*, *33*(22), n/a–n/a, doi:10.1029/2006GL026797, l22604.

Hoskins, B. J. (1974), The role of potential vorticity in symmetric stability and instability, *Quarterly Journal of the Royal Meteorological Society*, *100*(425), 480–482, doi:10.1002/qj.49710042520.

Hoskins, B. J. (1982), The mathematical theory of frontogenesis, *Annual Review of Fluid Mechanics*, *14*(1), 131–151, doi: 10.1146/annurev.fl.14.010182.001023.

Huyer, A., M. Knoll, T. Paluzkiewicz, and R. L. Smith (1991), The peru undercurrent: A study in variability, *Deep Sea Res.*, *39*, 247–279.

Jenkins, W. J. (1988), Nitrate flux into the euphotic zone near bermuda, *Nature*, *331*(6156), 521–523.

Johnson, G. C., and K. E. McTaggart (2010), Equatorial pacific 13 °c water eddies in the eastern subtropical south pacific ocean*, *Journal of Physical Oceanography*, *40*(1), 226–236, doi:10.1175/2009JPO4287.1.

Johnson, G. C., J. M. Toole, and N. G. Larson (2007), Sensor corrections for sea-bird sbe-41cp and sbe-41 ctds*, *Journal of Atmospheric and Oceanic Technology*, *24*(6), 1117–1130, doi:10.1175/JTECH2016.1.

Kadko, D. C., L. Washburn, and B. Jones (1991), Evidence of subduction within cold filaments of the northern california coastal transition zone, *Journal of Geophysical Research: Oceans*, *96*(C8), 14,909–14,926, doi:10.1029/91JC00885.

Kalvelage, T., G. Lavik, P. Lam, S. Contreras, L. Arteaga, C. R. Loscher, A. Oschlies, A. Paulmier, L. Stramma, and M. M. M. Kuypers (2013), Nitrogen cycling driven by organic matter export in the south pacific oxygen minimum zone, *Nature Geosci*, *6*(3), 228–234.

Kalvelage, T., G. Lavik, M. M. Jensen, N. P. Revsbech, C. Löscher, H. Schunck, D. K. Desai, H. Hauss, R. Kiko, M. Holtappels, J. LaRoche, R. A. Schmitz, M. I. Graco, and M. M. M. Kuypers (2015), Aerobic microbial respiration in oceanic oxygen minimum zones, *PLoS ONE*, *10*(7), e0133,526–.

Karstensen, J. (2004), Formation of the South Pacific Shallow Salinity Minimum: A Southern Ocean Pathway to the Tropical Pacific, *Journal of Physical Oceanography*, *34*, doi:10.1175/JPO2634.1.

Karstensen, J., and D. Quadfasel (2002), Formation of southern hemisphere thermocline waters: Water mass conversion and subduction*, *Journal of Physical Oceanography*, *32*(11), 3020–3038, doi:10.1175/1520-0485(2002)032¡3020:FOSHTW¿2.0.CO;2.

Karstensen, J., L. Stramma, and M. Visbeck (2008), Oxygen minimum zones in the eastern tropical Atlantic and Pacific oceans, *Progress in Oceanography*, *77*(4), 331–350, doi:10.1016/j.pocean.2007.05.009.

Karstensen, J., B. Fiedler, F. Schütte, P. Brandt, A. Körtzinger, G. Fischer, R. Zantopp, J. Hahn, M. Visbeck, and D. Wallace (2015), Open ocean dead zones in the tropical north atlantic ocean, *Biogeosciences*, *12*(8), 2597–2605, doi:10.5194/bg-12-2597-2015.

Kessler, W. S. (2006), The circulation of the eastern tropical Pacific: A review, *Progress in Oceanography*, *69*(2-4), 181–217, doi:10.1016/j.pocean.2006.03.009.

Kinsella, E. D., A. E. Hay, and W. W. Denner (1987), Wind and topographic effects on the labrador current at carson canyon, *Journal of Geophysical Research: Oceans*, *92*(C10), 10,853–10,869, doi: 10.1029/JC092iC10p10853.

Klein, P., and G. Lapeyre (2009), The oceanic vertical pump induced by mesoscale and submesoscale turbulence, *Annual Review of Marine Science*, *1*(1), 351–375, doi:10.1146/annurev.marine.010908.163704, pMID: 21141041.

Knauss, J. A. (1957), An observation of an oceanic front., *Tellus*, *9 (2)*, 234–237.

Koehn, E. (2014), Kleinskalige Variabilitaet in einem Gebiet permanenten Auftriebs vor der Kueste Perus, *Christian-Albrechts-Universitaet Kiel (Bachelor Thesis)*, p. 41 pp.

Kolmogorov, A. (1941), The Local Structure of Turbulence in Incompressible Viscous Fluid for Very Large Reynolds' Numbers, *Akademiia Nauk SSSR Doklady*, *30*, 301–305.

Lam, P., G. Lavik, M. M. Jensen, J. van de Vossenberg, M. Schmid, D. Woebken, D. Gutiérrez, R. Amann, M. S. M. Jetten, and M. M. M. Kuypers (2009), Revising the nitrogen cycle in the peruvian oxygen minimum zone, *Proceedings of the National Academy of Sciences*, *106*(12), 4752–4757, doi: 10.1073/pnas.0812444106.

Lapeyre, G., P. Klein, and B. L. Hua (2006), Oceanic restratification forced by surface frontogenesis, *J. Phys. Oceanogr.*, *36*(8), 1577–1590, doi: 10.1175/JPO2923.1.

Lathuilière, C., V. Echevin, M. Lévy, and G. Madec (2010), On the role of the mesoscale circulation on an idealized coastal upwelling ecosystem, *Journal of Geophysical Research: Oceans*, *115*(C9), n/a–n/a, doi: 10.1029/2009JC005827.

Ledwell, J. R., A. J. Watson, and C. S. Law (1998), Mixing of a tracer in the pycnocline, *Journal of Geophysical Research: Oceans*, *103*(C10), 21,499–21,529, doi:10.1029/98JC01738.

Lee, C., L. Thomas, and Y. Yoshikawa (2006), Intermediate water formation at the japan/east sea subpolar front., *Oceanography*, *19*(3), 110–121.

Levy, M. (2008), The modulation of biological production by oceanic mesoscale turbulence, in *Transport and Mixing in Geophysical Flows*, *Lecture Notes in Physics*, vol. 744, edited by J. Weiss and A. Provenzale, pp. 219–261, Springer Berlin Heidelberg.

Levy, M., R. Ferrari, P. J. S. Franks, A. P. Martin, and P. Riviere (2012), Bringing physics to life at the submesoscale, *Geophysical Research Letters*, *39*(14), n/a–n/a, doi:10.1029/2012GL052756, l14602.

Liang, J.-H., J. C. McWilliams, J. Kurian, F. Colas, P. Wang, and Y. Uchiyama (2012), Mesoscale variability in the northeastern tropical pacific: Forcing mechanisms and eddy properties, *Journal of Geophysical Research: Oceans*, *117*(C7), n/a–n/a, doi:10.1029/2012JC008008.

Loescher, C. R., T. Groskopf, F. D. Desai, D. Gill, H. Schunck, P. L. Croot, C. Schlosser, S. C. Neulinger, N. Pinnow, G. Lavik, M. M. M. Kuypers, J. LaRoche, and R. A. Schmitz (2014), Facets of diazotrophy in the oxygen minimum zone waters off peru, *ISME J*, *8*(11), 2180–2192.

Lutjeharms, J. R. E., F. A. Shillington, and C. M. D. Rae (1991), Observations of extreme upwelling filaments in the southeast atlantic ocean, *Science*, *253*(5021), 774–776, doi:10.1126/science.253.5021.774.

Luyten, J. R., J. Pedlosky, and H. Stommel (1983a), Climatic inferences from the ventilated thermocline., *Clim Chang*, *5*(2), 183–191.

Luyten, J. R., J. Pedlosky, and H. Stommel (1983b), The ventilated thermocline, *Journal of Physical Oceanography*, *13*(2), 292–309, doi:10.1175/1520-0485(1983)013¡0292:TVT¿2.0.CO;2.

Mahadevan, A., and D. Archer (2000), Modeling the impact of fronts and mesoscale circulation on the nutrient supply and biogeochemistry of the upper ocean, *Journal of Geophysical Research: Oceans*, *105*(C1), 1209–1225, doi:10.1029/1999JC900216.

Mahadevan, A., and A. Tandon (2006), An analysis of mechanisms for submesoscale vertical motion at ocean fronts, *Ocean Modelling*, *14*(3–4), 241 – 256, doi:http://dx.doi.org/10.1016/j.ocemod.2006.05.006.

Mahadevan, A., A. Tandon, and R. Ferrari (2010), Rapid changes in mixed layer stratification driven by submesoscale instabilities and winds, *Journal of Geophysical Research: Oceans*, *115*(C3), n/a–n/a, doi:10.1029/2008JC005203, c03017.

Marshall, D. P., and C. E. Tansley (2001), An implicit formula for boundary current separation, *Journal of Physical Oceanography*, *31*(6), 1633–1638, doi:10.1175/1520-0485(2001)031¡1633:AIFFBC¿2.0.CO;2.

Martin, A. P., and K. J. Richards (2001), Mechanisms for vertical nutrient transport within a north atlantic mesoscale eddy, *Deep Sea Research Part II: Topical Studies in Oceanography*, *48*(4–5), 757 – 773, doi:http://dx.doi.org/10.1016/S0967-0645(00)00096-5, the Biological Oceanography of the north-east Atlantic-the {PRIME} study.

McDougall, T., and P. Barker (2011), *Getting started with TEOS-10 and the Gibbs Seawater (GSW) Oceanographic Toolbox 28p*, SCOR/IAPSO WG127, ISBN 978-0-646-55621-5 ed.

McDowell, S. E., and H. T. Rossby (1978), Mediterranean water: An intense mesoscale eddy off the bahamas, *Science*, *202*(4372), 1085–1087, doi:10.1126/science.202.4372.1085.

McGillicuddy, D., A. Robinson, D. Siegel, H. Jannasch, R. Johnson, T. Dickey, J. McNeil, A. Michaels, and A. Knap (1998), Influence of mesoscale eddies on new production in the sargasso sea, *Nature*, *394*, 263–265.

McGillicuddy, D. J., L. A. Anderson, S. C. Doney, and M. E. Maltrud (2003), Eddy-driven sources and sinks of nutrients in the upper ocean: Results from a 0.1° resolution model of the north atlantic, *Global Biogeochemical Cycles*, *17*(2), n/a–n/a, doi:10.1029/2002GB001987.

McGillicuddy, D. J., L. A. Anderson, N. R. Bates, T. Bibby, K. O. Buesseler, C. A. Carlson, C. S. Davis, C. Ewart, P. G. Falkowski, S. A. Goldthwait, D. A. Hansell, W. J. Jenkins, R. Johnson, V. K. Kosnyrev, J. R. Ledwell, Q. P. Li, D. A. Siegel, and D. K. Steinberg (2007), Eddy/wind interactions stimulate extraordinary mid-ocean plankton blooms, *Science*, *316*(5827), 1021–1026, doi:10.1126/science.1136256.

McWilliams, J. C. (1985), Submesoscale, coherent vortices in the ocean, *Reviews of Geophysics*, *23*(2), 165–182, doi:10.1029/RG023i002p00165.

McWilliams, J. C., and M. J. Molemaker (2011), Baroclinic frontal arrest: A sequel to unstable frontogenesis, *J. Phys. Oceanogr.*, *41*(3), 601–619, doi:10.1175/2010JPO4493.1.

McWilliams, J. C., F. Colas, and M. J. Molemaker (2009), Cold filamentary intensification and oceanic surface convergence lines, doi: 10.1029/2009GL039402.

McWilliams, J. C., J. Gula, M. J. Molemaker, L. Renault, and A. F. Shchepetkin (2015), Filament frontogenesis by boundary layer turbulence, *J. Phys. Oceanogr.*, pp. –, doi:10.1175/JPO-D-14-0211.1.

Mechoso, C. R., R. Wood, R. Weller, C. S. Bretherton, A. D. Clarke, H. Coe, C. Fairall, J. T. Farrar, G. Feingold, R. Garreaud, C. Grados, J. McWilliams, S. P. de Szoeke, S. E. Yuter, and P. Zuidema (2014), Ocean–cloud–atmosphere–land interactions in the southeastern pacific: The vocals program, *Bulletin of the American Meteorological Society*, *95*(3), 357–375, doi:10.1175/BAMS-D-11-00246.1.

Merckelbach, L., D. Smeed, and G. Griffiths (2010), Vertical water velocities from underwater gliders, *Journal of Atmospheric and Oceanic Technology*, *27*(3), 547–563, doi:10.1175/2009JTECHO710.1.

Messié, M., and F. Chavez (2014), Seasonal regulation of primary production in eastern boundary upwelling systems, *Progress in Oceanography*.

Meunier, T., E. D. Barton, B. Barreiro, and R. Torres (2012), Upwelling filaments off cap blanc: Interaction of the nw african upwelling current and the cape verde frontal zone eddy field?, *Journal of Geophysical Research: Oceans*, *117*(C8), n/a–n/a, doi:10.1029/2012JC007905, c08031.

Molemaker, M. J., J. C. McWilliams, and I. Yavneh (2005), Baroclinic instability and loss of balance, *J. Phys. Oceanogr.*, *35*(9), 1505–1517, doi:10.1175/JPO2770.1.

Molemaker, M. J., J. C. McWilliams, and X. Capet (2010), Balanced and unbalanced routes to dissipation in an equilibrated eady flow, *Journal of Fluid Mechanics*, *654*, 35–63, doi:10.1017/S0022112009993272.

Molemaker, M. J., J. C. McWilliams, and W. K. Dewar (2015), Submesoscale instability and generation of mesoscale anticyclones near a separation of the california undercurrent, *Journal of Physical Oceanography*, doi:10.1175/JPO-D-13-0225.1.

Montes, I., F. Colas, X. Capet, and W. Schneider (2010), On the pathways of the equatorial subsurface currents in the eastern equatorial pacific and their contributions to the peru-chile undercurrent, *Journal of Geophysical Research: Oceans*, *115*(C9), n/a–n/a, doi:10.1029/2009JC005710.

Montes, I., B. Dewitte, E. Gutknecht, A. Paulmier, I. Dadou, A. Oschlies, and V. Garçon (2014), High-resolution modeling of the eastern tropical

pacific oxygen minimum zone: Sensitivity to the tropical oceanic circulation, *Journal of Geophysical Research: Oceans*, *119*(8), 5515–5532, doi: 10.1002/2014JC009858.

Mueller, P., and M. Briscoe (2000), Diapycnal mixig and internal waves., *Oceanography*, *13*(2), 98–103.

Munk, W., L. Armi, K. Fischer, and F. Zachariasen (2000), Spirals on the sea, *Proceedings of the Royal Society of London A: Mathematical, Physical and Engineering Sciences*, *456*(1997), 1217–1280, doi:10.1098/rspa.2000.0560.

Munk, W. H. (1966), Abyssal recipes, *Deep Sea Research*, *13*, 707–730.

Nagai, T., N. Gruber, H. Frenzel, Z. Lachkar, J. C. McWilliams, and G.-K. Plattner (2015), Dominant role of eddies and filaments in the offshore transport of carbon and nutrients in the california current system, *Journal of Geophysical Research: Oceans*, pp. n/a–n/a, doi:10.1002/2015JC010889.

Okubo, A. (1970), Horizontal dispersion of floatable particles in the vicinity of velocity singularities such as convergences, *Deep Sea Research and Oceanographic Abstracts*, *17*(3), 445 – 454, doi: http://dx.doi.org/10.1016/0011-7471(70)90059-8.

Olbers, D., J. Willebrand, and C. Eden (2012), *Ocean Dynamics*, Springer Verlag Berlin, Berlin.

Omand, M. M., E. A. D'Asaro, C. M. Lee, M. J. Perry, N. Briggs, I. Cetini, and A. Mahadevan (2015), Eddy-driven subduction exports particulate organic carbon from the spring bloom, *Science*, *348*(6231), 222–225, doi: 10.1126/science.1260062.

Oschlies, A. (2002), Can eddies make ocean deserts bloom?, *Global Biogeochemical Cycles*, *16*(4), 53–1–53–11, doi:10.1029/2001GB001830, 1106.

Oschlies, A., and V. Garcon (1998), Eddy-induced enhancement of primary production in a model of the north atlantic ocean, *Nature*, *394*, 266–269.

Paulmier, A., and D. Ruiz-Pino (2009), Oxygen minimum zones (omzs) in the modern ocean, *Progress in Oceanography*, *80*(3–4), 113–128, doi: http://dx.doi.org/10.1016/j.pocean.2008.08.001.

Pedlosky, J. (1979), *Geophysical Fluid Dynamics*, 624 pp., Springer-Verlag New York.

Pennington, J. T., K. L. Mahoney, V. S. Kuwahara, D. D. Kolber, R. Calienes, and F. P. Chavez (2006), Primary production in the eastern tropical pacific: A review, *Progress in Oceanography*, *69*(2–4), 285 – 317, doi:http://dx.doi.org/10.1016/j.pocean.2006.03.012, a Review of Eastern Tropical Pacific Oceanography.

Penven, P., V. Echevin, J. Pasapera, F. Colas, and J. Tam (2005), Average circulation, seasonal cycle, and mesoscale dynamics of the peru current system: A modeling approach, *Journal of Geophysical Research: Oceans*, *110*(C10), n/a–n/a, doi:10.1029/2005JC002945.

Pietri, A., P. Testor, V. Echevin, A. Chaigneau, L. Mortier, G. Eldin, and C. Grados (2013), Finescale Vertical Structure of the Upwelling System off Southern Peru as Observed from Glider Data, *Journal of Physical Oceanography*, *43*(3), 631–646, doi:10.1175/JPO-D-12-035.1.

Pietri, A., V. Echevin, P. Testor, A. Chaigneau, L. Mortier, C. Grados, and A. Albert (2014), Impact of a coastal-trapped wave on the near-coastal circulation of the Peru upwelling system from glider data, *Journal of Geophysical Research: Oceans*, *119*(3), 2109–2120, doi:10.1002/2013JC009270.

Pollard, R. T., and L. A. Regier (1992), Vorticity and vertical circulation at an ocean front, *J. Phys. Oceanogr.*, *22*(6), 609–625, doi:10.1175/1520-0485(1992)022¡0609:VAVCAA¿2.0.CO;2.

Prater, M. D. (1992), Observations and hypothesized generation of a meddy in the gulf of cadiz, Ph.D. thesis, Applied Physics Laboratory, University of Washington, University of Washington, 1013 NE 40th St., Seattle, WA 98105-6698.

Ramachandran, S., A. Tandon, and A. Mahadevan (2014), Enhancement in vertical fluxes at a front by mesoscale-submesoscale coupling, *Journal of Geophysical Research: Oceans*, *119*(12), 8495–8511, doi:10.1002/2014JC010211.

Revsbech, N. P., L. H. Larsen, J. Gundersen, T. Dalsgaard, O. Ulloa, and B. Thamdrup (2009), Determination of ultra-low oxygen concentrations in oxygen minimum zones by the stox sensor, *Limnology and Oceanography: Methods*, *7*(5), 371–381, doi:10.4319/lom.2009.7.371.

Risien, C. M., and D. B. Chelton (2008), A global climatology of surface wind and wind stress fields from eight years of quikscat scatterometer data, *J. Phys. Oceanogr.*, *38*(11), 2379–2413, doi:10.1175/2008JPO3881.1.

Rossi, V., C. López, J. Sudre, E. Hernández-García, and V. Garçon (2008), Comparative study of mixing and biological activity of the benguela and canary upwelling systems, *Geophysical Research Letters*, *35*(11), n/a–n/a, doi:10.1029/2008GL033610, l11602.

Rossi, V., C. López, E. Hernández-García, J. Sudre, V. Garçon, and Y. Morel (2009), Surface mixing and biological activity in the four eastern boundary upwelling systems, *Nonlinear Processes in Geophysics*, *16*(4), 557–568, doi: 10.5194/npg-16-557-2009.

Rudnick, D. L., and J. R. Luyten (1996), Intensive surveys of the azores front: 1. tracers and dynamics, *Journal of Geophysical Research: Oceans*, *101*(C1), 923–939, doi:10.1029/95JC02867.

Rudnick, D. L., R. E. Davis, C. C. Eriksen, D. M. Fratantoni, and M. J. Perry (2004), Underwater gliders for ocean research, *Marine Technology Society Journal*, *38*(2), 73–84.

Schmidtko, S., G. C. Johnson, and J. M. Lyman (2013), Mimoc: A global monthly isopycnal upper-ocean climatology with mixed layers, *Journal of Geophysical Research: Oceans*, *118*(4), 1658–1672, doi:10.1002/jgrc.20122.

Schneider, W., R. Fuenzalida, E. Rodríguez-Rubio, J. Garcés-Vargas, and L. Bravo (2003), Characteristics and formation of eastern south pacific intermediate water, *Geophysical Research Letters*, *30*(11), n/a–n/a, doi: 10.1029/2003GL017086.

Shchepetkin, A. F., and J. C. McWilliams (2005), The regional oceanic modeling system (roms): a split-explicit, free-surface, topography-following-coordinate oceanic model, *Ocean Modelling*, *9*(4), 347 – 404, doi: http://dx.doi.org/10.1016/j.ocemod.2004.08.002.

Shchepetkin, A. F., and J. C. McWilliams (2009), Correction and commentary for "ocean forecasting in terrain-following coordinates: Formulation and skill assessment of the regional ocean modeling system" by haidvogel et al., j. comp. phys. 227, pp. 3595-3624, *Journal of Computational Physics*, *228*(24), 8985 – 9000, doi:http://dx.doi.org/10.1016/j.jcp.2009.09.002.

Siedler, G., J. Church, and J. Gould (2001), in *Ocean Circulation and ClimateObserving and Modelling the Global Ocean*, *International Geophysics*, vol. 77, edited by J. C. Gerold Siedler and J. Gould, pp. xviii – iixix, Academic Press, doi:http://dx.doi.org/10.1016/S0074-6142(01)80106-6.

Silva, N., N. Rojas, and A. Fedele (2009), Water masses in the humboldt current system: Properties, distribution, and the nitrate deficit as a chemical water mass tracer for equatorial subsurface water off chile, *Deep Sea Research Part II: Topical Studies in Oceanography*, *56*(16), 1004 – 1020, doi:http://dx.doi.org/10.1016/j.dsr2.2008.12.013, the Oceanography of the Eastern South Pacific II: The Oxygen Minimum Zone.

Smith, K. S., and R. Ferrari (2009), The production and dissipation of compensated thermohaline variance by mesoscale stirring, *Journal of Physical Oceanography*, *39*(10), 2477–2501, doi:10.1175/2009JPO4103.1.

Smyth, W. D., J. N. Moum, and D. R. Caldwell (2001), The efficiency of mixing in turbulent patches: Inferences from direct simulations and microstructure observations, *J. Phys. Oceanogr.*, *31*(8), 1969–1992, doi:10.1175/1520-0485(2001)031¡1969:TEOMIT¿2.0.CO;2.

Stone, P. H. (1966), On non-geostrophic baroclinic stability, *J. Atmos. Sci.*, *23*(4), 390–400, doi:10.1175/1520-0469(1966)023¡0390:ONGBS¿2.0.CO;2.

Stone, P. H. (1970), On non-geostrophic baroclinic stability: Part ii, *J. Atmos. Sci.*, *27*(5), 721–726, doi:10.1175/1520-0469(1970)027¡0721:ONGBSP¿2.0.CO;2.

Stone, P. H. (1972), On non-geostrophic baroclinic stability: Part iii. the momentum and heat transports, *J. Atmos. Sci.*, *29*(3), 419–426, doi:10.1175/1520-0469(1972)029¡0419:ONGBSP¿2.0.CO;2.

Stramma, L., G. C. Johnson, J. Sprintall, and V. Mohrholz (2008), Expanding oxygen-minimum zones in the tropical oceans, *Science*, *320*(5876), 655–658, doi:10.1126/science.1153847.

Stramma, L., G. C. Johnson, E. Firing, and S. Schmidtko (2010), Eastern pacific oxygen minimum zones: Supply paths and multidecadal changes, *Journal of Geophysical Research*, *115*(C9), C09,011.

Stramma, L., A. Oschlies, and S. Schmidtko (2012), Mismatch between observed and modeled trends in dissolved upper-ocean oxygen over the last 50 yr, *Biogeosciences*, *9*(10), 4045–4057, doi:10.5194/bg-9-4045-2012.

Stramma, L., H. W. Bange, R. Czeschel, a. Lorenzo, and M. Frank (2013), On the role of mesoscale eddies for the biological productivity and biogeochemistry in the eastern tropical Pacific Ocean off Peru, *Biogeosciences*, *10*(11), 7293–7306, doi:10.5194/bg-10-7293-2013.

Stramma, L., R. A. Weller, R. Czeschel, and S. Bigorre (2014), Eddies and an extreme water mass anomaly observed in the eastern south pacific at the stratus mooring, *Journal of Geophysical Research: Oceans*, *119*(2), 1068–1083, doi:10.1002/2013JC009470.

Strub, P. T., P. M. Kosro, and A. Huyer (1991), The nature of the cold filaments in the california current system, *Journal of Geophysical Research: Oceans*, *96*(C8), 14,743–14,768, doi:10.1029/91JC01024.

Strub, P. T., J. M. Mesias, V. Montecino-B., J. Rutllant-C., and S. Salinas-M. (1998), Coastal ocean circulation off western South America, in *The Sea, The Global Coastal Ocean vol. 11*, edited by A. Robinson and K. Brink, 11 ed., pp. 273–313, John Wiley and Sons, NY.

Tandon, A., and C. Garrett (1994), Mixed layer restratification due to a horizontal density gradient, *J. Phys. Oceanogr.*, *24*(6), 1419–1424, doi: 10.1175/1520-0485(1994)024¡1419:MLRDTA¿2.0.CO;2.

Taylor, J. R., and R. Ferrari (2009), On the equilibration of a symmetrically unstable front via a secondary shear instability, *Journal of Fluid Mechanics*, *622*, 103–113, doi:10.1017/S0022112008005272.

Testor, P., G. Meyers, C. Pattiaratchi, R. Bachmayer, D. Hayes, S. Pouliquen, L. Petit de la Villeon, T. Carval, A. Ganachaud, L. Gourdeau, L. Mortier, H. Claustre, V. Taillandier, P. Lherminier, T. Terre, M. Visbeck, J. Karstensen, G. Krahmann, A. Alvarez, M. Rixen, P.-M. Poulain, S. Osterhus, J. Tintore, S. Ruiz, B. Garau, D. Smeed, G. Griffiths, L. Merckelbach, T. Sherwin, C. Schmid, J. Barth, O. Schofield, S. Glenn, J. Kohut, M. Perry, C. Eriksen, U. Send, R. Davis, D. Rudnick, J. Sherman, C. Jones, D. Webb, C. Lee, and B. Owens (2010), Gliders as a component of future observing systems, in *Proc. OceanObs09: Sustained Ocean Observations and Information for Society*, vol. 2, ESA, WPP-306., Venice, Italy,.

Thomas, L. N., and C. M. Lee (2005a), Intensification of ocean fronts by down-front winds, *J. Phys. Oceanogr.*, *35*(6), 1086–1102, doi: 10.1175/JPO2737.1.

Thomas, L. N., and C. M. Lee (2005b), Intensification of ocean fronts by down-front winds, *J. Phys. Oceanogr.*, *35*(6), 1086–1102, doi: 10.1175/JPO2737.1.

Thomas, L. N., and J. R. Taylor (2010), Reduction of the usable wind-work on the general circulation by forced symmetric instability, *Geophysical Research Letters*, *37*(18), n/a–n/a, doi:10.1029/2010GL044680, l18606.

Thomas, L. N., A. Tandon, and A. Mahadevan (2008), *Submesoscale Processes and Dynamics*, pp. 17–38, American Geophysical Union, doi: 10.1029/177GM04.

Thomas, L. N., J. R. Taylor, R. Ferrari, and T. M. Joyce (2013), Symmetric instability in the gulf stream, *Deep Sea Research Part II: Topical Studies in Oceanography*, *91*, 96 – 110, doi: http://dx.doi.org/10.1016/j.dsr2.2013.02.025, subtropical Mode Water in the North Atlantic Ocean.

Thomsen, S., C. Eden, and L. Czeschel (2014), Stability analysis of the labrador current, *J. Phys. Oceanogr.*, *44*(2), 445–463, doi:10.1175/JPO-D-13-0121.1.

Treguier, A. M., S. Theetten, E. P. Chassignet, T. Penduff, R. Smith, L. Talley, J. O. Beismann, and C. Böning (2005), The north atlantic subpolar gyre in four high-resolution models, *J. Phys. Oceanogr.*, *35*(5), 757–774, doi:10.1175/JPO2720.1.

Uda, M. (1938), Researches on siome or current rip in the seas and oceans., *Geophysical Magazine*, *II*, 307–372.

Vazquez-Cuervo, J., B. Dewitte, T. M. Chin, E. M. Armstrong, S. Purca, and E. Alburqueque (2013), An analysis of {SST} gradients off the peruvian coast: The impact of going to higher resolution, *Remote Sensing of Environment*, *131*, 76 – 84, doi:http://dx.doi.org/10.1016/j.rse.2012.12.010.

Vignudelli, S., A. Kostianoy, P. Cipollini, and J. Benveniste (2011), *Coastal Altimetry*, 1, Springer-Verlag Berlin Heidelberg.

Vollmer, L., and C. Eden (2013), A global map of meso-scale eddy diffusivities based on linear stability analysis, *Ocean Modelling*, *72*, 198 – 209, doi: http://dx.doi.org/10.1016/j.ocemod.2013.09.006.

von Storch, J.-S., C. Eden, I. Fast, H. Haak, D. Hernández-Deckers, E. Maier-Reimer, J. Marotzke, and D. Stammer (2012), An estimate of the lorenz energy cycle for the world ocean based on the storm/ncep simulation, *J. Phys. Oceanogr.*, *42*(12), 2185–2205, doi:10.1175/JPO-D-12-079.1.

Ward, B. B., A. H. Devol, J. J. Rich, B. X. Chang, S. E. Bulow, H. Naik, A. Pratihary, and A. Jayakumar (2009), Denitrification as the dominant nitrogen loss process in the arabian sea, *Nature*, *461*(7260), 78–81.

Weiss, J. (1991), The dynamics of enstrophy transfer in two- dimensional hydrodynamics., *Physica*, *48*, 273–294.

Winkler, L. W. (1888), Die Bestimmung des im Wasser gelösten Sauerstoffes, *Berichte der deutschen chemischen Gesellschaft*, *21*(2), 2843–2854, doi: 10.1002/cber.188802102122.

Wunsch, C. (1998), The work done by the wind on the oceanic general circulation, *J. Phys. Oceanogr.*, *28*(11), 2332–2340, doi:10.1175/1520-0485(1998)028¡2332:TWDBTW¿2.0.CO;2.

Wunsch, C. (2002), What is the thermohaline circulation?, *Science*, *298*(5596), 1179–1181, doi:10.1126/science.1079329.

Wunsch, C., and R. Ferrari (2004), Vertical mixing, energy, and the general circulation of the oceans, *Annual Review of Fluid Mechanics*, *36*(1), 281–314, doi:10.1146/annurev.fluid.36.050802.122121.

Wyrtki, K. (1962), The oxygen minima in relation to ocean circulation, *Deep Sea Research and Oceanographic Abstracts*, *9*(1–2), 11 – 23, doi: http://dx.doi.org/10.1016/0011-7471(62)90243-7.

Wyrtki, K. (1963), The horizontal and vertical field of motion in the peru current, *Bull. Scripps Inst. Oceanogr*, *8*, 313–344.

Wyrtki, K. (1967), Circulation and water masses in the eastern equatorial pacific ocean, *J. Oceanol. Limnol.*, *1*, 117–147.

Xu, C., X.-D. Shang, and R. X. Huang (2014), Horizontal eddy energy flux in the world oceans diagnosed from altimetry data, *Scientific Reports*, *4*, 5316–.

Zamora, L. M., A. Oschlies, H. W. Bange, K. B. Huebert, J. D. Craig, A. Kock, and C. R. Löscher (2012), Nitrous oxide dynamics in low oxygen regions of the pacific: insights from the memento database, *Biogeosciences*, *9*(12), 5007–5022, doi:10.5194/bg-9-5007-2012.

Zhang, Z., W. Wang, and B. Qiu (2014), Oceanic mass transport by mesoscale eddies, *Science*, *345*(6194), 322–324, doi: 10.1126/science.1252418.

Author Contributions

Sören Thomsen carried out the analysis, produced all the figures and wrote the text of the thesis and both manuscripts presented in sections 5 and 6.

Torsten Kanzow contributed ideas to the design the observational experiment off Peru, the analysis and commented on the thesis and the two manuscripts presented in sections 5 and 6.

Richard J. Greatbatch contributed ideas to the analysis and commented on the thesis and the manuscript presented in section 5.

Gerd Krahmann performed the data calibration of the CTD and glider measurements used in this thesis. He further contributed ideas to the analysis and commented on both manuscripts found in sections 5 and 6.

Marcus Dengler contributed ideas to the analysis and commented on the manuscripts presented in section 5.

Gaute Lavik contributed ideas to the analysis and commented on the manuscripts presented in section 5.

Francois Colas performed the ROMS model experiment used in the thesis and provided the model output. He contributed ideas to the analysis and commented on the manuscript found in section 6.

Vincent Echevin contributed ideas to the analysis and commented on the manuscript found in section 6.

Anja Engel contributed ideas to the analysis and commented on the manuscripts presented in section 6.

Acknowledgements

I want to say special thanks to Torsten Kanzow for the enduring support and trust throughout my entire studies, for providing the interesting topic and giving me a lot of freedom for my research. Furthermore, I am greatful to Richard J. Greatbatch for taking so much of his time, his never-ending support and the inspiring discussions. I want to thank Francois Colas and Vincent Echevin for providing the ROMS model output, all their support and hospitality during my great visit in Paris. I want to thank Gerd Krahmann for providing the calibrated CTD and glider datasets and for supporting me with all questions related to data quality and calibration. I am greatful to Marcus Dengler for the inspiring discussions and support during my entire thesis. I want to thank Anja Engel for her enduring support and all the interesting discussions related to biogeochemistry. I am grateful for the support and input of Gaute Lavik related to the nitrogen cycle off Peru. I also want to thank the whole physical oceanography department for the nice work environment. I want to say great thanks to: Liam Brannigan for helpful suggestions and proofreading the entire thesis; Nils Brüggemann, Katharina Müller, Julius Busecke, Miriam Ferrer-Gonzalez, Tim Fischer and Johannes Hahn for proofreading and commenting on parts of the thesis; Kristin Burmeister for her great support as a HiWi and proofreading parts of the thesis; Christiane Schelten, Nadira Mahmud, Sigrun Komander-Hoepner and Juliane Barth for their effective and priceless support in paperwork.

Affirmation - Eidesstattliche Erklärung

Hiermit erkläre ich an Eides statt, dass ich die vorliegende Arbeit unter Einhaltung der Regeln guter wissenschaftlicher Praxis der Deutschen Forschungsgemeinschaft selbständig erarbeitet und verfasst und keine anderen als die angegebenen Quellen und Hilfsmittel verwendet habe.

Ich versichere, dass diese Arbeit in der vorgelegten oder einer ähnlichen Fassung noch nicht an anderer Stelle zur Erlangung des Doktorgrades eingereicht worden ist.

Kiel, Datum, Unterschrift (Sören Thomsen)